Metals and Ceramics Division

Heavy Vehicle Propulsion Materials Program
Quarterly Progress Report for
April through June 2005

D. R. Johnson
Technical Project Manager

Prepared for
U.S. Department of Energy
Assistant Secretary for Energy Efficiency and Renewable Energy
Office of FreedomCAR and Vehicle Technologies Program
VT 05 01 020

Prepared by the
OAK RIDGE NATIONAL LABORATORY
Oak Ridge, Tennessee 37831-6066
Managed by
UT-Battelle, LLC
for the Department of Energy
Under contract DE-AC05-00OR22725

CONTENTS

Materials for Fuel Systems

High Toughness Materials (ORNL)

Materials for Exhaust Aftertreatment

Materials for Exhaust Aftertreatment (Caterpillar Inc.)

Development of Materials Analysis Tools for Studying NO_x Adsorber Catalysts (ORNL)

Development of NO_x Sensor for Heavy Vehicle Applications (ORNL and Ford Motor Company)

Microstructural Changes in NO_x Trap Materials Under Lean and Rich Conditions at High Temperatures (ORNL)

Catalysis by First Principles (ORNL)

Durability of Particulate Filters (ORNL)

Materials for Air Handling, Hot Section, and Structural Components

Lightweight Valve Train Materials (Caterpillar Inc.)

Thick Thermal Barrier Coatings (TTBCs) for Low Emission, High Efficiency Diesel Engine Components (Caterpillar)

Nanoengineered Materials (North Carolina A&T State University)

NDE of Diesel Engine Components (Argonne National Laboratory)

Durability of Diesel Engine Component Materials (ORNL)

Life Prediction of Diesel Engine Components (ORNL and Caterpillar)

Low-Cost Manufacturing of Precision Diesel Engine Components (ORNL)

Advanced Machining and Sensor Concepts (University of Michigan)

Advanced Cast Austenitic Stainless Steels for High-Temperature Components (ORNL and Caterpillar Inc.)

TiAl Nanolaminate Composites (Lawrence Livermore National Laboratory)

High-Density Infrared Surface Treatment of Materials for Heavy-Duty Vehicles (ORNL)

High Temperature Aluminum Alloys (Cummins)

Mechanical Behavior of Ceramic Materials for Heavy Duty Diesel Engines (ORNL)

Deformation Processes for the Next Generation Ceramics (ORNL)

High Speed Machining of Titanium Project (Third Wave Systems, Inc.)

Synthesis of Nanocrystalline Ceramics (Pennsylvania State University)

Development of Titanium Components for a Heavy-Duty Diesel Engine Turbocharger (Caterpillar Inc.)

Test and Materials Standards

IEA – Rolling Contact Fatigue (ORNL)

IEA Implementing Agreement for a Programme of Research and Development on Advanced Materials for Transportation Applications (ORNL)

Testing Standards (NIST)

Surface Modification of Engineering Materials for Heavy Vehicle Applications (NIST)

Low Cost-High Toughness Ceramics

T. N. Tiegs, F. C. Montgomery, and J. O. Kiggans
Oak Ridge National Laboratory

Objective/Scope

Significant improvement in the reliability of structural ceramics for advanced diesel engine applications could be attained if the critical fracture toughness (K_{Ic}) were increased without strength degradation. Currently, the project is examining toughening of ceramics by incorporation of ductile intermetallic phases.

Technical Highlights

Previous studies have shown that the properties of the aluminide-bonded ceramics are attractive for diesel engine applications and consequently, development of these materials was started. At the present time, TiC-based composites with 40-60 vol. % Ni_3Al are being developed because they have expansion characteristics very close to those for steel. The development effort is being done in collaboration with CoorsTek, Inc.

As reported previously, a large batch (>15 kg total) of TiC-50 vol. % Ni_3Al powder using new NiAl commercial source was fabricated and shipped to CoorsTek. Initial sintering results indicated the densification behavior was similar to the earlier composites, but slightly less: 6.05 g/cm^3 versus 6.11 g/cm^3. However, flexural strength measurements revealed a rather low strength in comparison to the previous material from a different NiAl manufacturer. The comparison was 945±150 MPa for the earlier materials and 600±37 MPa for the newest batch. SEM examination of a fracture surface showed numerous agglomerates ≤100 μm in size. EDAX indicated they were NiAl particles. Evidently the new batch of NiAl powder contained larger particles (even though the powder was listed as <44 μm).

A modified milling procedure was instituted with the NiAl and particle size analysis indicated all particles were <10 μm. Sintering of test parts with the modified powder was improved and densities of ~6.11 g/cm^3 were obtained. This density is equal or better than the previous high strength materials. A test batch (~3 kg) of powder with the modified milling procedure has been sent to CoorsTek for injection molding. Parts and test MOR bars have been manufactured and sent back to ORNL. Sintering behavior of these injection molded materials will be reported in the next progress report.

Status of Milestones

On schedule.

Communications/Visits/Travel

Numerous communications with CoorsTek on cermet processing were done.

Problems Encountered

The sintering furnace used for processing studies was out of service part of the time because of a faulty pressure control valve.

Publications

None.

Advanced Diesel Aftertreatment

Corey Shannon, Herbert DaCosta, Julie Faas, Matt Stefanick, Svetlana Zemskova, Christie Ragle, Ron Silver, Paul Park, and Craig Habeger
Caterpillar Inc.

Objective/Scope

The objective of the effort is to develop and evaluate materials that will be utilized in aftertreatment systems for diesel engine applications. These materials include catalysts for CO and hydrocarbon oxidation, NO_x reduction, and filtration media to improve particulate abatement capabilities in the exhaust system. The project is a part of Caterpillar strategy to meet EPA requirements for regulated diesel emissions in 2007 and beyond.

This year's focus is to assess durability of various catalyst technologies in terms of phosphorous, sulfur, and thermal degradation, and to identify diesel particulate trapping materials that have high durability and filtration efficiency to comply with future emission regulations for heavy-duty diesel engines.

Technical Highlights

Catalyst Durability.

NO_x Adsorber durability: A series of model Lean NO_x Traps (LNT) were made by coating 400 cpsi cordierite monolith cores with γ-Al_2O_3 washcoat. The cores were then dipped in Ce acetate solution, dried then calcined at 550ºC for 5 hours to give a loading of 20 wt. % CeO_2. The process was repeated with a Ba acetate solution to give a loading of 11 wt% BaO, and then with Pt/Rh nitrate solution, resulting in a loading of 5 wt. % Pt and 0.6 wt. % Rh. The finished catalysts were reduced in 5% H_2 at 350ºC for 2 hours. The finished catalysts were tested for NO_x conversion using a laboratory reactor and 1-inch-diameter x 3-inch catalyst cores at a space velocity of 55 K/h. Each sample was degreened at 275ºC for 20 minutes in a reducing gas (2.5% H_2, 2.5% CO, 5% CO_2, 5% H_2O, bal. N_2), then switched to an oxidizing mix (12% O_2, 5% CO_2, 5% H_2O, bal. N_2). 200 ppm NO_x (10% NO_2) was added to load the samples. After saturating the samples at 275ºC, the LNTs were ramped to 425ºC in the oxidizing mix without the NO_x, regenerated in the reducing gas and reloaded with NO_x. After determining the initial activity of the model LNT, the sample was exposed to 3.6 g/L of phosphorus using a diesel fuel burner with phosphorus-doped fuel at 250ºC. The aged sample was then re-analyzed for NO_x conversion in the lab reactor. The aging process was repeated to increase the exposure of some of the catalysts to 10 g/L of phosphorus.

The oxidation, storage, and reduction function of the NO_x adsorbers was tested after loading with 3.6 and 10 g/L phosphorus, with and without a blank monolith in front. Results indicate that phosphorus degrades LNTs. The NO oxidation function was not affected by the exposure of 3.6 g/L phosphorus; however, NO to NO_2 conversion dropped from 45% to about 35% after exposure to 10 g/L phosphorus.

In contrast to the relatively stable oxidation function, a significant impact was observed on the catalyst storage capacity even on exposure to 3.6 g/L of phosphorus. Figure 1 shows that at 20% NO slip, the moles of NO_x stored per mole of available Ba in the LNT dropped by 65%.

Furthermore, at a constant storage capacity of 0.05 moles NO_x /mole Ba, the NO_x slip increased from 6% on a fresh LNT to 30% after 3.6 g/L P, and to 90% after exposure to 10 g/L P.

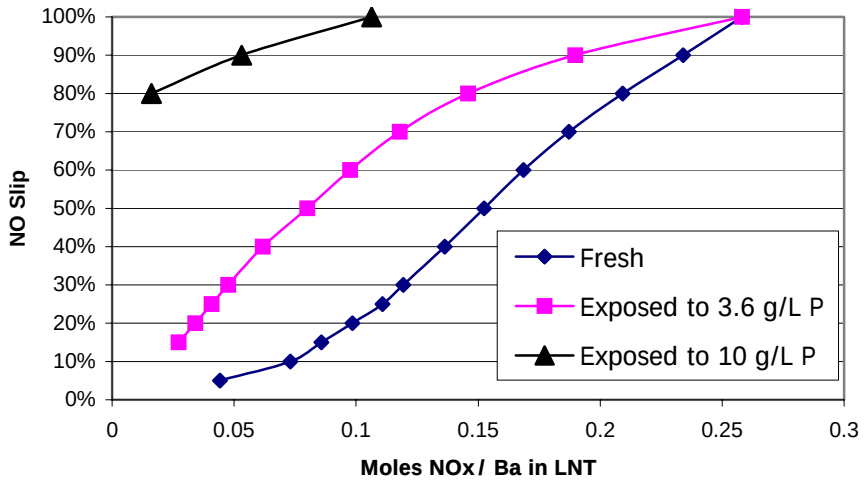

Figure 1: The effect of phosphorus exposure on LNT NO_x storage for three different exposures.

The reduction of NO to N_2 under the rich condition was negatively affected by the loss of LNT storage capacity. Figure 2 shows the NO_x storage capacity at 80% slip of a series of fresh LNTs plotted against the amount of NO_x reduced to N_2. A straight line was fit to the data with a correlation coefficient of 0.968. Exposing the catalysts to 3.6 g/L phosphorus reduced the storage capacity and thus decreased the NO_x reduction. However, testing the LNTs in the opposite direction from which they were exposed to phosphorus revealed a significant boost in N_2 formation from NO_x. When the LNT cores are exposed to phosphorus, the phosphorus tends to deposit in a non-uniform profile with the greatest amount of phosphorus in the front of the core and less phosphorus in the rear. Any NO_x introduced to the front of this aged sample cannot be adsorbed until it gets far enough into the core that phosphorus isn't blocking the adsorption sites. Upon switching to rich gas, the front section of the aged LNT has no NO_x to release and thus no reduction occurs. If NO_x containing gas is introduced at the rear of the core, NO_x begins storing immediately inside the new entrance of the sample. In this case, when the system is swept by rich gas, the upstream section of the LNT has stored NO_x to release and the Rh in the downstream high phosphorus part of the catalyst can reduce the NO_x to N_2. Thus the Rh in the LNT appears to remain active for NO reduction even if no NO_x is stored due to the phosphorus blocking adsorption sites.

Results from this first phase of testing show that phosphorus poisoning may become a significant source of deactivation as durability requirements become increasingly stringent. For LNTs, the NO_x storage capacity function is affected first and most strongly.

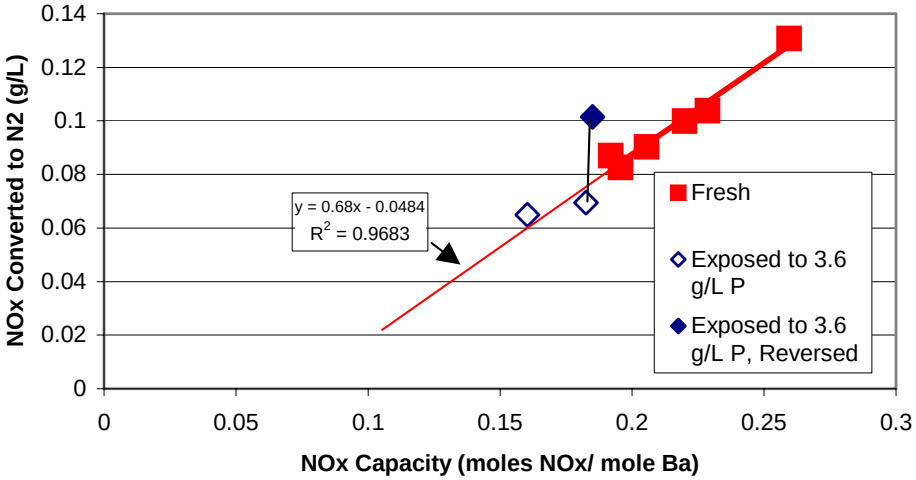

Figure 2: The effect of phosphorus exposure on LNT reduction of NO in a rich gas stream.

Diesel Particulate Filter (DPF)

Two different ceramic-based un-catalyzed DPF materials obtained from suppliers have been tested and the results for filtration efficiency and backpressure were compared. The experimental results indicate a significant difference in backpressure between the two different DPF materials.

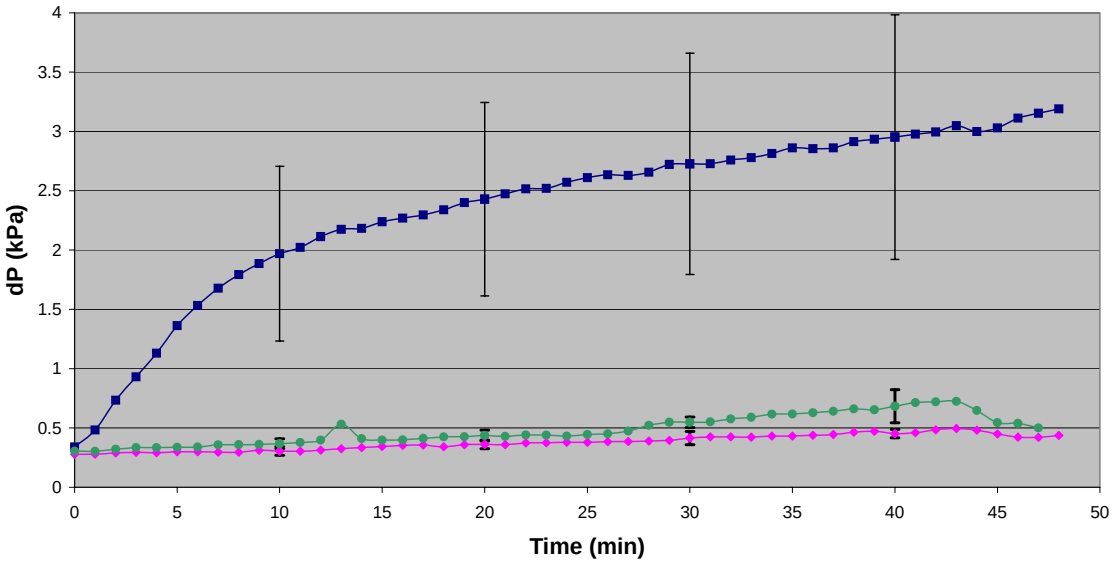

Figure 3: A plot of back pressure vs. time for two different filtration materials.

The Figure 3 shows the backpressure during the soot-loading process of two DPF materials. Pink diamonds represent the uncatalyzed material #1, and green circles represent the catalyzed material #1. Blue squares represent the uncatalyzed material #2. Three independent measurements of each DPF sample were averaged to show the experimental repeatability. Error

bars are shown for all data sets at every ten minutes. In terms of back pressure, the material #1 performed significantly better than the material #2. In addition, material #1 (uncatalyzed as well as catalyzed samples) showed excellent repeatability with much less variance than material #2.

Despite the significant difference in backpressure, both types of uncatalyzed filter materials showed high filtration efficiency (97-99%) throughout the duration of the experiment. The filtration efficiency of the catalyzed samples (Material #1) remained high (97-98%) without significant change in backpressure.

Future Plans

1. Urea-SCR samples will be loaded with various levels of phosphorus to determine durability relative to fresh performance. Results will be compared with the previous data on LNTs.
2. The regeneration efficiency of the DPF samples will be tested.

Travel

1. Ron Silver and Paul Park traveled to Philadelphia, PA to attend the 19th Annual Meeting of the North American Catalysis Society.
2. Herbert DaCosta made a trip (Detroit, Mi) to attend the SAE World Congress.

Presentations/Publications

Ronald G. Silver, Matthew Stefanick, Julie M. Faas, and Svetlana Zemskova, "Impact of Phosphorus Exposure on Lean NO_x Trap Performance," presented at the 19th Annual Meeting of the North American Catalysis Society, Philadelphia (2005)

Paul Park and Carrie Boyer, "Effect of SO_2 on the Activity over Ag/γ-Al_2O_3 Catalysts for NO_x Reduction in Lean Conditions," presented at the 19th Annual Meeting of the North American Catalysis Society, Philadelphia (2005).

Status of FY 2005 Milestones

1. The durability study of various catalyst technologies (oxidation catalyst, NO_x adsorber and urea-SCR) for phosphorus and S degradation has progressed as scheduled.
2. The measurement of filtration efficiency and backpressure of uncatalyzed and catalyzed DPF 1-in. x 3-in. core samples obtained from suppliers were completed.

Development of Materials Analysis Tools for Studying NO_x Adsorber Catalysts

Thomas Watkins, Larry Allard, Doug Blom, Michael Lance, Harry Meyer, Larry Walker and Chaitanya Narula
Oak Ridge National Laboratory

Roger England, Bill Epling, Howard Fang and Tom Yonushonis
Cummins Inc.

Objective

The objective of this effort is to produce a quantitative understanding of the processing and in-service effects on NO_x adsorber catalyst technology leading to an exhaust aftertreatment system with improved catalyst performance capable of meeting the 2007 emission requirements.

Samples and Approach

A Cummins catalyst supplier provided new catalyst materials, which are being examined with diagnostic tools developed under the CRADA. Investigations of these candidate-production materials are being implemented on both the bench and engine research scale. These investigations include the examination of unused, reactor and engine-aged catalyst samples. Investigative tools included transmission electron microscopy (TEM), X-ray diffraction (XRD), X-ray photoelectron spectroscopy (XPS), Raman Spectroscopy and infrared spectroscopy (IR).

Technical Highlight

A model catalyst system was examined with both scanning transmission electron microscopy (STEM) and X-ray diffraction (XRD). The model system contains gamma-alumina and Pt on a cordierite substrate. The size of the Pt particles or crystallites was sought as a function of length along the catalyst brick. Figure 1 shows the Pt particle sizes to be the same at both ends of the sample. The bright spots in the STEM images are the Pt particles. Multivariate Statistical Analysis, an analysis procedure for spectral image datasets, was applied to extract the particle size distribution from 10 images of each section. While the distributions appear to be different, the average and median sizes effectively the same. The same sample was examined with XRD to determine the particle size as a function of length along the sample. Eight 10 mm areas are being examined while the remaining 70 mm is masked off with (100) Si wafer parts. The XRD results also showed negligible particle/crystallite size growth/change along the length of the sample, but did not agree with respect to size (see Figure 2). This is probably due to the superposition of the platinum and alumina peaks. This will be investigated further.

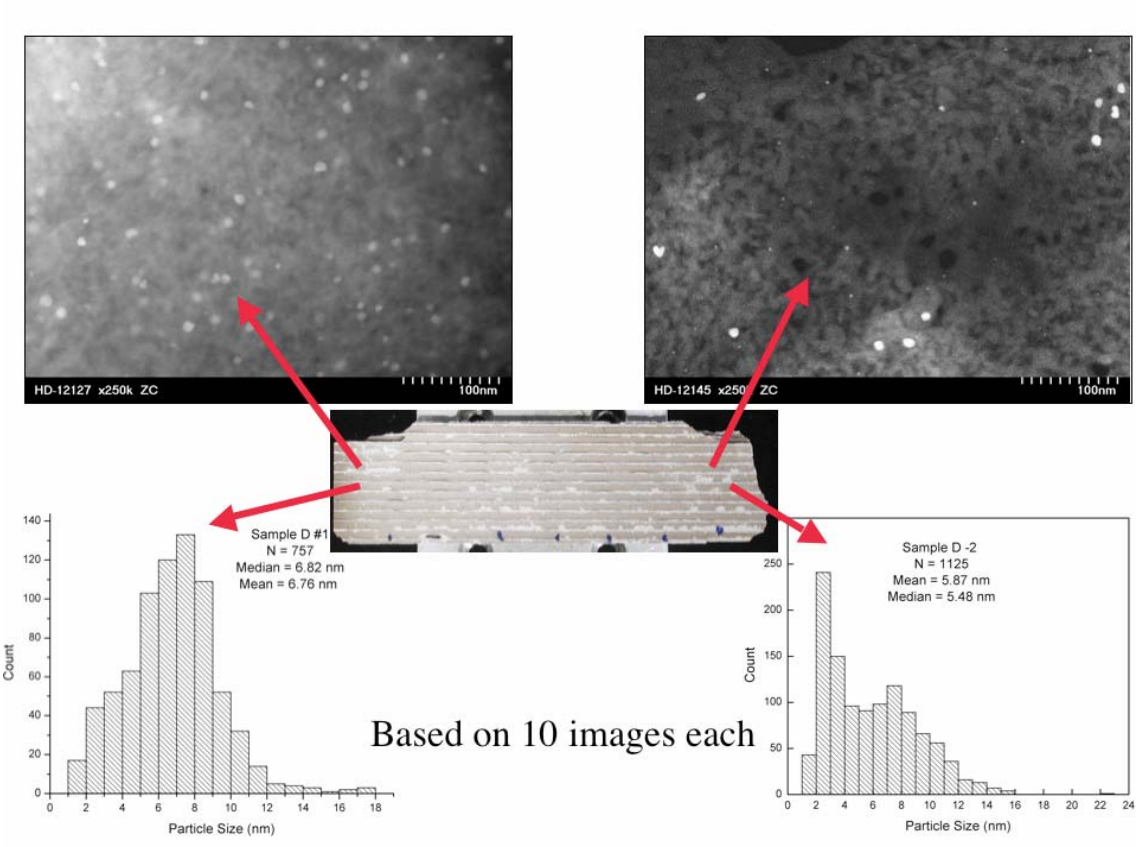

Figure 1: STEM results from location indicated on the sample.

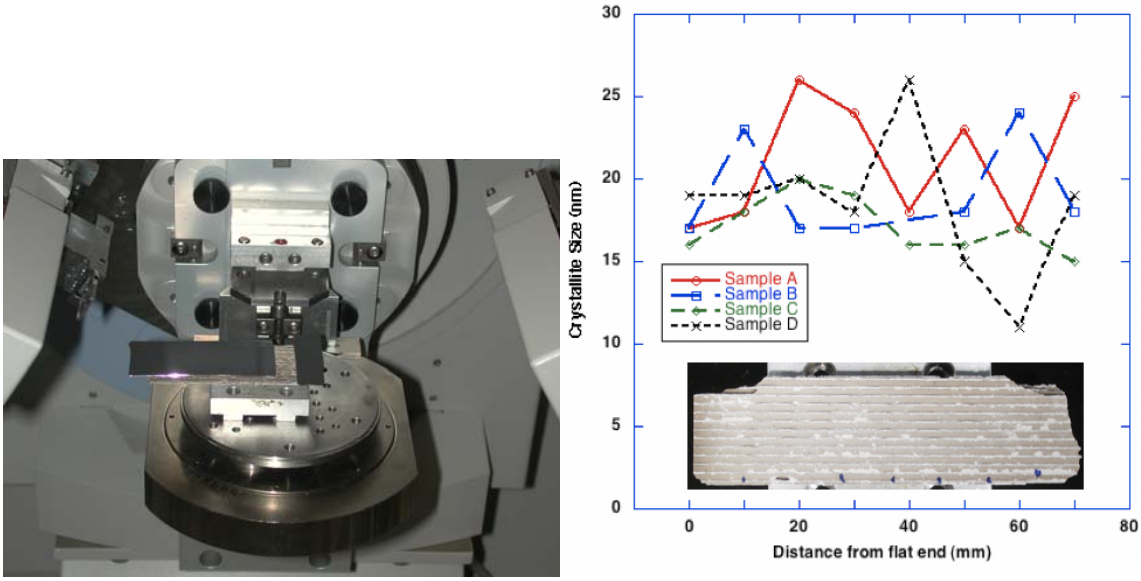

Figure 2: The XRD experimental set up and crystallite size as a function of length along the sample.

Development of NO_x Sensors for Heavy Vehicle Applications

Timothy R. Armstrong, David L. West, Fred C. Montgomery
Oak Ridge National Laboratory

CRADA No. ORNL 01-0627
with Ford Motor Company

Objective

The proposed project seeks to develop technologies and materials that will facilitate the development of NO_x and ammonia sensors. The development of low-cost, simple NO_x will facilitate the development of ultra-low NO_x emission engines, directly supporting the OHVT goals.

Technical Highlights

Most work was driven by need to identify alternative electrode/substrate combination, pursuant to observation that $La_{1-x}Sr_xCrO_3/Zr_{2-x}Y_xO_{2-\delta}$ sensing elements showed evidence of decomposition after long-term operation in the presence of NO_2 and H_2O. Two main alternatives were explored:

1. $La_{0.85}Sr_{0.15}CrO_3$ (LSC) electrodes on $Ce_{0.8}Gd_{0.2}O_{2-\delta}$ (GdC) substrates.
    a. Sensing elements using this materials combination could yield "total NO_x" sensing at 600°C as shown in Figure 1. Fig. 1 also shows that the $[O_2]$ sensitivity is a decreasing function of $[NO_x]$, similar to the behavior of elements with LSC electrodes and $Zr_{2-x}Y_xO_{2-\delta}$ (YSZ) substrates.
    b. The DC resistance of this materials combination tended to increase with time (Fig. 2). The changes in DC resistance due to the presence of NO, however, stayed relatively constant.
    c. No decomposition was observed after exposure to H_2O (g), NO_x, and electrical stimulus for ~100 hr. at 600°C. See Fig. 3.

2. $LaCr_{0.85}Mg_{0.15}O_3$ (LMC) electrodes on $Zr_{1.84}Y_{0.16}O_{2-\delta}$ (YSZ) substrates.
    a. This materials combination could not yield "total NO_x" sensing performance. Although the responses to NO and NO_2 were of the same algebraic sign, the response to NO_2 was greater in magnitude (Fig. 4).
    b. The DC resistance of these sensing elements decreased slowly at 600°C under the condition of constant applied current (0.25 μA) as seen in Fig. 5a. Changes induced by NO (20–190 ppm) were constant over a period of 3 days (Fig. 5b)
    c. No decomposition was observed after exposure to H_2O (g), NO_x, and electrical stimulus for ~100 hr. at 600°C. See Fig. 6.

Future Plans

- Continue investigation of alternate substrates and electrode materials. In particular, plan to examine Cr-deficient $LaCrO_3$. (Cr deficiency should enhance electronic conductivity, as Cr deficiency leads to formation of Cr^{4+}.)
- Work with CRADA partners to develop methods of quantifying and characterizing sensing element "drift" (as exemplified in Fig. 2). "Drift" is becoming increasingly important to industry member of CRADA team (Ford).
- Investigate acquisition of equipment that would allow of the application of low-frequency (1-100 Hz) AC stimulus.

Status of FY 2005 Milestones

(1) Optimize the electrode design (geometry) to maximize output signal. **(03/05)**
Completed 03/05 with interdigitated electrodes

(2) Optimize the electrode morphology for the current class of lanthanum chromite electrocatalysts to maximize output signal. **(05/05)**
On hold pending milestone 3.

(3) Evaluate sensor sensitivity to steam and develop protocol to minimize. **(09/05)**
Ford recently indicated during a phone call that milestone 3 is to be the focus of this year's activity. They further indicated that humidity has been the major cause of failure in most NO_x sensors developed to date and they wish us to develop an understanding of humidities effects on our materials immediately. ***On track***

Communications/Visits/Travel

Biweekly teleconference were initiated this quarter between DOE, Ford, LLNL, and ORNL.

Problems Encountered

None to date.

Publications

None

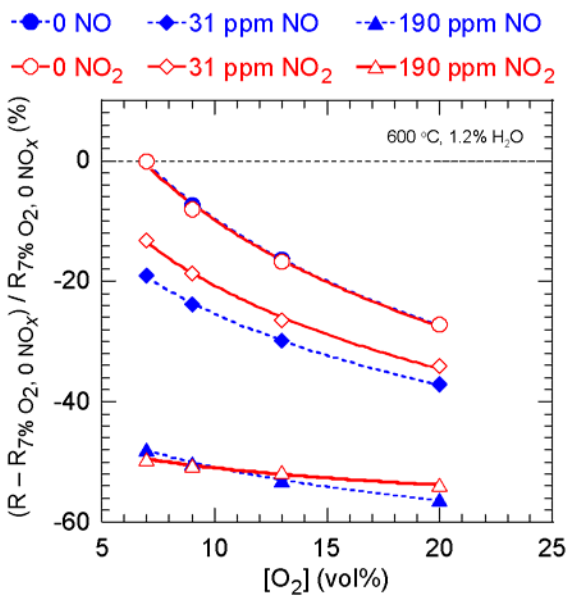

Figure 1. Sensing performance of prototype LSC/GdC element. 15 mV was applied as a DC electrical stimulus.

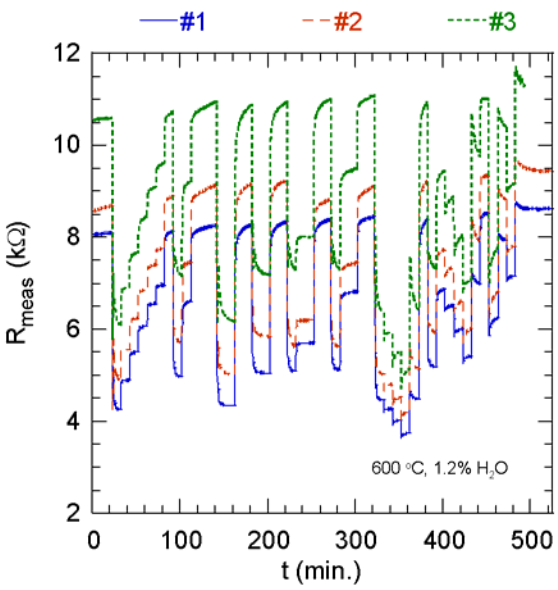

Figure 2: Response of a prototype LSC/GdC element (15 mV electrical stimulus) to varying [NO] and [O_2]. The [NO] and [O_2] variations (0–190 ppm_V and 7–20 vol. %) were identical for each of the three runs.

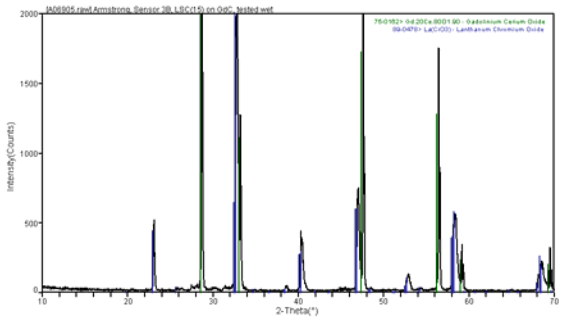

Figure 3: X-ray diffraction (Cu K_{α}) pattern from a tested LSC/GdC sensing element. All peaks in the pattern can be assigned to LSC or GdC, indicating that no decomposition has occurred during use.

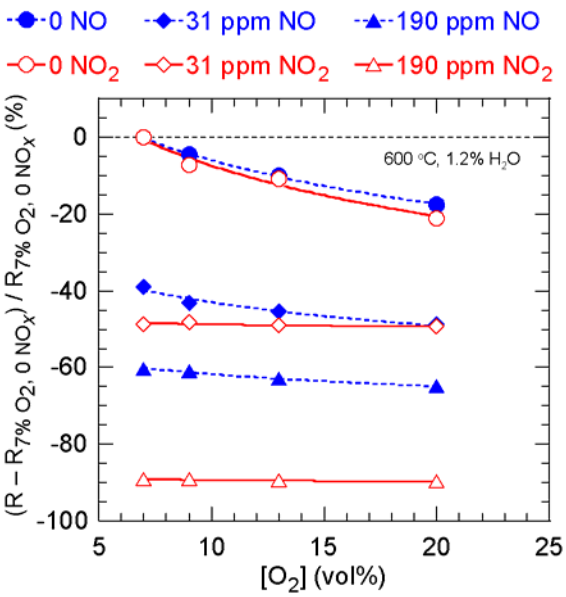

Figure 4: Sensing performance of prototype LMC/YSZ element. 0.25 μA was applied as a DC electrical stimulus. Note the stronger NO_2 response, particularly for 190 ppm.

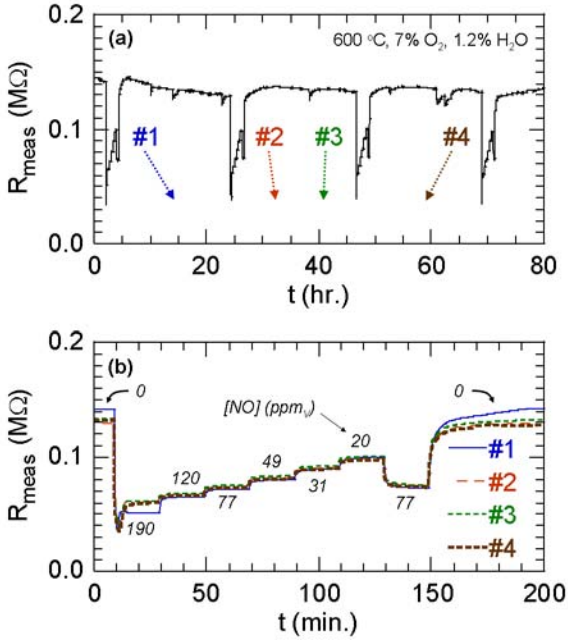

Figure 5: Measured response of a LMC/YSZ sensing element with constant applied current (0.25 μA). No NO was present except at the times indicated by the numbers in the upper figure (a). The lower figure (b) shows the changes induced by NO concentrations between 20 and 190 ppm_V.

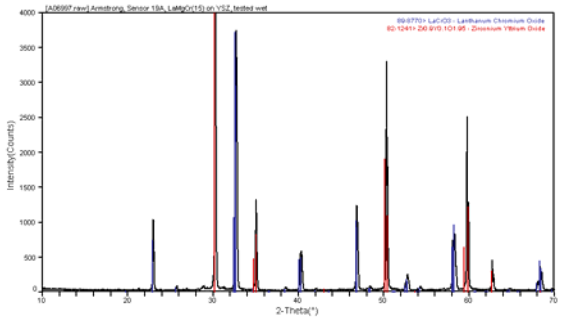

Figure 6. X-ray diffraction (Cu K_α) pattern from a tested LMC/YSZ sensing element. All peaks in the pattern can be assigned to LMC or YSZ, indicating that no decomposition has occurred during use.

Microstructural Changes in NO_x Trap Materials under Lean and Rich Conditions at High Temperatures

C.K. Narula, M. Moses, and L.F. Allard
Oak Ridge National Laboratory

Objective/Scope

The introduction of diesel-engine-based heavy-duty trucks and passenger vehicles depends on the successful development of a strategy to treat nitrogen oxides (NO_x) emissions. A catalyst or a combination of catalysts that can convert NO_x into inert gases under oxidizing conditions over a complete range of exhaust temperatures does not presently exist. Among NO_x treatment strategies, lean NO_x traps (LNT) are the most likely candidates for early deployment because they are consumer transparent (no action needed on the part of consumers) and can be system-integrated into current vehicle control strategies [1].

NO_x traps collect engine out NO_x during lean operation and treat it during short rich operation cycles [2]. The NO_x traps can be considered to be derived from commercial three-way catalysts (TWC) installed to treat stoichiometric emissions from engines operating at air-fuel ratios of ~14. As such, the basic components of NO_x traps are identical to three-way catalysts. The advance version of three-way catalyst is a two-layer system on a honeycomb substrate with the inner layer based on platinum-alumina and the outer layer on rhodium-ceria-zirconia. The NO_x traps derived from advanced three-way catalysts are identical to these with the exception of high baria content (the upper limit being close to 20%) in the alumina layer.

Fresh NO_x traps work very well but cannot sustain their high efficiency over the life-time of vehicles. The gradual and persistent deterioration in the performance of commercial TWC is quite well known [3]. The performance deterioration in NO_x traps is believed to be caused by aging due to high-temperature operation and sulfation-desulfation cycles necessitated by the sulfur oxides in the emissions from the oxidation of sulfur in fuel. The formation of barium aluminate is also considered to be a cause of performance deterioration since barium aluminate forms on thermal aging and is an inefficient NO_x adsorber. Until last year, the aging related microstructural changes in precious metals component were not available in open literature. In our previous reports, we summarized our studies of fresh and aged supplier samples that clearly show changes that occur on aging under various operating conditions. The prominent changes are sintering and migration of precious metals and migration of barium leading to reduced precious metal-adsorber surface area available for NO_x adsorption in lean cycles.

In order to design a thermally durable NO_x trap, there is a need to understand the changes in the microstructure of materials that occur during various modes of operation (lean, rich, and lean-rich cycles). This information can form the basis for selection and design of new NO_x trap materials that can resist the deterioration under normal operation. The first goal of the project is to determine if one or all of the microstructural changes take place during lean, rich, or lean-rich cycles.

The tasks to achieve this goal are as follows:

- Complete microstructural characterization of fresh and thermally aged NO_x trap materials to determine the species formed as a result of aging.
- Complete microstructural characterization of fresh NO_x trap materials after exposure to lean conditions to determine the species formed during lean cycles.
- Complete microstructural characterization of fresh NO_x trap materials after exposure to rich conditions to determine the species formed during rich cycles.

The second goal of the project is to investigate and design new materials that can withstand NO_x trap operating conditions without undergoing detrimental structural changes. The results from the first goal will provide insights into changes that occur in NO_x trap materials at a microstructural level upon extended exposure to NO_x trap operating conditions enabling selection and design of materials for the second goal.

Technical Highlights

Over the last two years, we determined the microstructural changes that occurred in a supplier lean NO_x trap system (based on Pt/BaO-Al_2O_3 and CeO_2-ZrO_2 materials) upon aging on (1) a pulsator at Ford (2) dyano at Ford, and (3) on vehicles in gasoline DISI engines in Europe.

- After pulsator aging, lean and rich aged samples showed that the sintering of platinum particles occurs during aging and barium migrates into ceria-zirconia layer. Both of these factors reduce platinum-barium oxide surface area where NO_x adsorption and reduction takes place during lean and rich cycles respectively. The stoichiometric aging also leads to the migration of barium into ceria-zirconia layer but the sintering of platinum is less severe.
- The dyano aged samples showed extensive sintering of platinum and its migration in ceria-zirconia layer. The sintering of rhodium was also observed. The migration of barium into ceria-zirconia and the sintering of precious metal component could explain the deterioration of performance
- The analysis of on vehicle evaluated samples after 32K kilometers and 80K kilometers showed that the bulk of precious metal sintering occurred in the early stages of on vehicle aging.

These results primarily show precious metal sintering and barium migration to be cause of performance deterioration in NO_x trap materials in gasoline engine exhaust conditions. While the laboratory aging protocols for diesel engines are in development, we have compiled a data showing early stage changes in model NO_x trap materials under diesel conditions. We assumed that lower temperature of simulated diesel exhaust would slow down the aging compared with gasoline engine exhaust. Thus, we completed a series of thermal aging, diesel lean aging, and diesel rich aging of model NO_x trap and model NO_x trap modified with manganese oxide as well as Pt/Al_2O_3 for comparison purposes. The results have been previously reported and are summarized in Table I with updates.

In the last report, we reported the completion of the updated ex-situ reactor which included a bench top tube furnace and dual solenoids. The updated reactor allowed us to evaluate catalyst under lean-rich cycles and the addition of the tube furnace extended the temperature range to 1000°C and provided continuous and reproducible temperatures.

We initiated our work using a 60-second lean and 5-second rich cycles at 500°C/4 h to mimic normal operating conditions. The model LNT catalyst, 2%Pt-98%[10%CeO_2-ZrO_2-

90%(2%La_2O_3-98% BaO•6Al_2O_3)], and the modified catalyst, 2%Pt, 5%MnO_2-93%[10%CeO_2-ZrO_2-90%(2%La_2O_3-98% BaO•6Al_2O_3)], were tested under this cycle using simulated diesel exhaust without SO_2. We observed Pt particle sintering under these conditions and some particles as large as 3.5 nm could be seen. A summary of these results is included in Table 1. The lack of significant sintering was consistent with the fact that LNTs are durable under normal operating conditions when no sulfur is present and no desulfation step is required. The impact of 240 s/60 s lean-rich cycle at normal operating (500°C) temperatures was not significant and the results are consistent with those observed in the 60 s/5 s cycling experiments as summarized below:

- 2% Pt/γ-Al_2O_3 aged under lean/rich cycling (240s/60s) at 500°C/4 h results in Pt particles with the same median range (1.0 – 1.5 nm) as the freshly prepared catalyst although some large particles ~3 nm can be seen.
- 2%Pt-98%[10%CeO_2-ZrO_2-90%(2%La_2O_3-98%BaO•6Al_2O_3)] aged under lean/rich cycling (240s/60s) at 500 °C results in Pt particles with the same median range (1.0 – 1.5 nm) as the freshly prepared catalyst but it shows some 3.5 nm particles. This result is also consistent with the results obtained in the 60 s/5 s cycling study.

We also carried out accelerated aging protocol using 60s/5 s lean-rich cycles at 700°C/16h and simulated diesel exhaust conditions without SO_2 and monitored the microstructural changes in the catalyst, 2%Pt-98%[10%CeO_2-ZrO_2-90%(2%La_2O_3-98% BaO•6Al_2O_3)], after every 4 h. After the first 4-h interval, sintering of the Pt particles was observed with the appearance of particles in 2-4.5 nm range accompanied by movement of particles as compared with fresh samples that show particles in 0.5-2.0 nm range. Further sintering in 4-h increments showed gradual increase in 2-5 nm particles [Table 2]. The impact of longer 240 s/60 s lean-rich cycle accelerated aging (700°C) temperatures was not significant and the results are consistent with those observed in the 60s/5s cycling experiments [Table 1 & 2]. Figure 1A-1E show TEMs and particle size distributions of 2%Pt-98%[10%CeO_2-ZrO_2-90%(2%La_2O_3-98% BaO•6Al_2O_3)] samples aged under lean/rich cycling (240 s/60 s) at the accelerated aging conditions for 4,8,12, and 16 h.

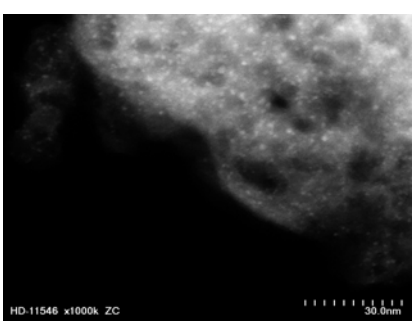

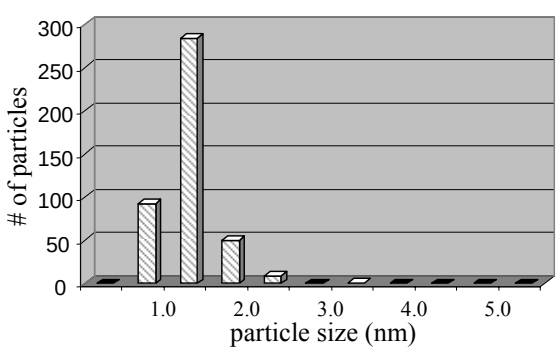

Figure 1A: Fresh Sample shows Pt particles in 0.5-2.5 nm range with distribution centered at 1 nm.

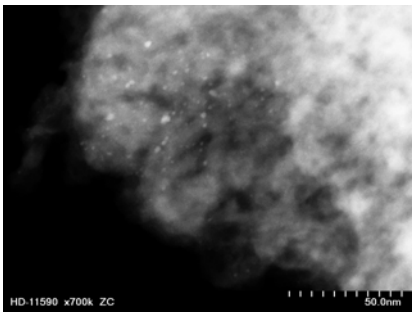

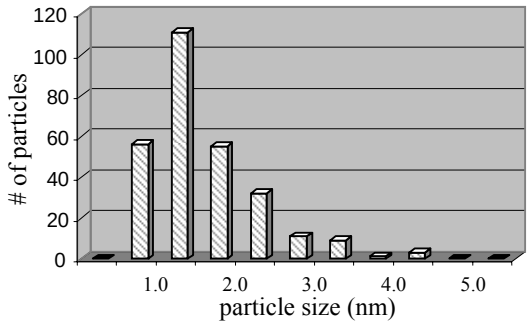

Figure 1B: After the first 4-h period, Pt particle size increases and is in 0.5-4.5nm range. On average, there was increase of 0.4 nm, but the median particle range didn't change. However, the locations and presence of the particles changed dramatically.

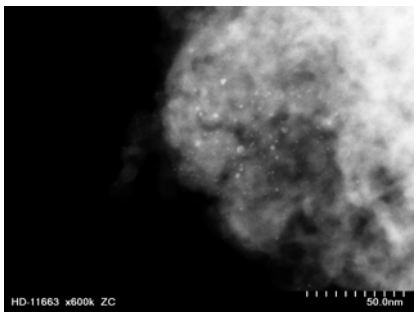

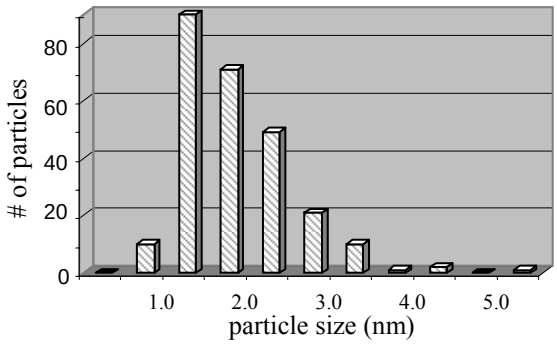

Figure 1C: After the second 4-h period, Pt particle size remained in 0.5-4.5 nm range. On average, there was increase of 0.3 nm due to increase in larger particles. The locations and presence of the Pt particles did not alter from that observed after the 1st 4 h of the lean/rich thermal aging protocol.

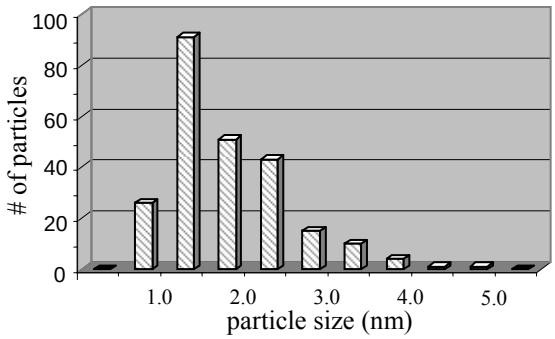

Figure 1D: After the third 4-h period, Pt particle size increased slightly to in 0.5-5.0 nm range. But there was no significant increase in average particle size or median. The locations and presence of the Pt particles did not alter from that observed after the 2nd 4 h of the lean/rich thermal aging protocol.

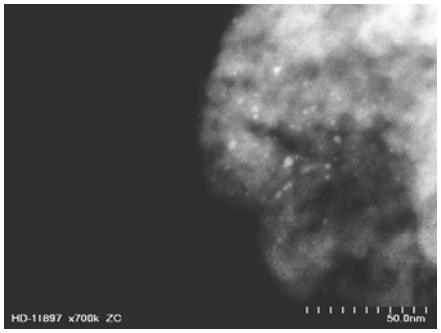

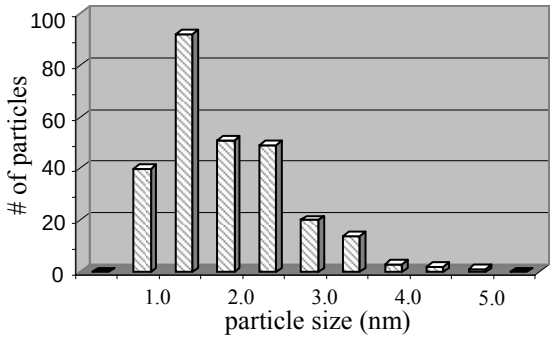

Figure 1E: After the fourth 4-h period, there was essentially no change from third 4h period. .

These results indicate that sintering occurs at the early stages of aging and subsequently, the particle size distribution shifts towards the larger particles.

We are initiating the study of microstructural changes in simulated exhaust containing sulfur oxide. Correlation of these results and those from catalyst evaluation studies will allow us to forecast durability based on microstructural changes.

Other activities

The assembly of a bench-top flow reactor is in process.

Communications/Visitors/Travel

CKN presented a paper at the Eighth DOE Crosscut Workshop on Lean Emissions Reduction Simulation based in part on this work. CKN will present a paper at the DEER conference based in part on this work.

Publications

1. Narula, C.K.; Shelton, W.A.; Allard, L.F.; Xu, Y.; M. Moses, M.; Schneider, W.; Gates, B.; Combining Theory and Experiments in Studies of Structural Changes in LNT Materials, Eighth DOE Crosscut Workshop on Lean Emissions Reduction Simulation, University of Michigan - Dearborn, Dearborn, Michigan 48128, May 17-19, (2005).
2. Narula, C.K.; Allard, L.F.; Moses, M.; Xu, Y.; Shelton, W.; Schneider, W.F.; Graham, G.; Hoard, J.; Lean NO_x Traps – Microstructural Studies of Real World and Model Catalysts, DEER 2005, Palmer Hilton, Chicago, Aug. 21-25, 2005.

References

1. Miyoshi, N.; Matsumoto, S.; Katoh, K.; Tanaka, T.; Harada, J.; Takahashi, N.; Yokota, K.; Sigiura M., and Kasahra, K.; “Development of New Concept Three-Way Catalyst for Automotive Lena-Burn Engines”, SAE paper 95-0809.

2. Takahashi, N.; Shinjoh, H.; Iijima, T.; Suzuki, T.; Yamazaki, K.; Yokota, K.; Suzuki, H.; Miyoshi, N.; Matsumoto, S.; Tanizawa, T.; Tateishi, S.; and Kasahara, K.; "The New Concept 3-Way Catalyst for Automotive Lean-Burn Engine: NO_x Storage and Reduction Catalyst", Catalysis Today, 1996, **27**, 63-69.
3. Gandhi, H.S., Graham, G.W., and McCabe, R.W., "Automotive Exhaust Catalysis", J. Cat., 2003, **216**, 433-442.

Table 1. Summary of Pt particle size change under various treatments to the model catalysts

CATALYST	**Fresh Sample[1]**	**Thermal Aging In Air (XRD of powder)**	**Lean Diesel Aging 500°C/4 h**	**Rich Diesel Aging 500°C/4 h**	**Lean/ Rich Cycle Diesel Aging 500°C/4 h[1]**	
					60 s/5 s	**240 s/60 s**
2% Pt / γ-Al_2O_3	0.8–2.0 nm (1.4 nm)	600ºC, 3.4 nm 700ºC, 17.1 nm 800ºC, 26.1 nm 900ºC, 39.5 nm	1.0– 2.0nm[1] (1.5 nm)	2.0 - 4.0 nm	N/A	0.6 – 3.0 nm (1.5 nm)
2%Pt-98%[10%CeO_2-ZrO_2-90%(2%La_2O_3-98% BaO•6Al_2O_3)]	0.6–2.9 nm (1.4 nm)	600ºC, 2.6 nm 700ºC, 21.3 nm 800ºC, 37.2 nm 900ºC, 48.4 nm	1.0 -2.0 nm	1.5 - 3.5 nm	0.5 – 4.3 nm (1.7 nm)	0.8 – 3.5 nm (1.7 nm)
2%Pt, 5%MnO_2-93%[10%CeO_2-ZrO_2-90%(2%La_2O_3-98% BaO•6Al_2O_3)]	0.7–2.6 nm (1.6 nm)	700ºC, 20.7 nm 800ºC, 27.0 nm 900ºC, 34.0 nm	2 – 3 nm	1 – 2 nm	0.7 – 3.2 nm (1.7 nm)	-------

1. Sample size ranges are reported and averages are reported in brackets.

Table 2. Summary of Pt particle size change under lean/rich cycle treatments at 700 °C to the model catalysts.

CATALYST	**Aging Time**	**Lean / Rich Diesel Exhaust without SO_2**	
		60 s/5 s[1]	**240 s/60 s[1]**
2%Pt-98%[10%CeO_2-ZrO_2-90%(2%La_2O_3-98% BaO•6Al_2O_3)]	**F**	0.6 – 2.9 nm (1.4 nm)	0.9 – 2.5 nm (1.5 nm)
	4 h	0.5 – 5.0 nm (2.1 nm)	0.6 – 4.4 nm (1.8 nm)
	8 h	0.6 – 5.4 nm (2.1 nm)	0.8 – 5.3 nm (2.1 nm)
	12 h	0.6 – 5.9 nm (2.0 nm)	0.7 – 4.7 nm (2.0 nm)
	16 h	N/A	0.7 – 4.7 nm (2.0 nm)

1. The distribution is centered on these values. Averages are reported in brackets

Catalysis by First Principles - Can Theoretical Modeling and Experiments Play a Complimentary Role in Catalysis?

C. Narula, W. Shelton, Y. Xu, M. Moses, L. Allard
Oak Ridge National Laboratory

V. Bhirundi, Prof. B. Gates
University of California, Davis

Prof. W. Schneider
University of Notre Dame

Objective/Scope

This research focuses on an integrated approach between computational modeling and experimental development, design and testing of new catalyst materials, that we believe will rapidly identify the key physiochemical parameters necessary for improving the catalytic efficiency of these materials.

The typical solid catalyst consists of nano-particles on porous supports. The development of new catalytic materials is still dominated by trial and error methods, even though the experimental and theoretical bases for their characterization have improved dramatically in recent years. Although it has been successful, the empirical development of catalytic materials is time consuming and expensive and brings no guarantees of success. Part of the difficulty is that most catalytic materials are highly non-uniform and complex, and most characterization methods provide only average structural data. Now, with improved capabilities for synthesis of nearly uniform catalysts, which offer the prospects of high selectivities as well as susceptibility to incisive characterization combined with state-of-the science characterization methods, including those that allow imaging of individual catalytic sites, we have compelling opportunity to markedly accelerate the advancement of the science and technology of catalysis.

Computational approaches, on the other hand, have been limited to examining processes and phenomena using models that had been much simplified in comparison to real materials. This limitation was mainly a consequence of limitations in computer hardware and in the development of sophisticated algorithms that are computationally efficient. In particular, experimental catalysis has not benefited from the recent advances in high performance computing that enables more realistic simulations (empirical and first-principles) of large ensemble atoms including the local environment of a catalyst site in heterogeneous catalysis. These types of simulations, when combined with incisive microscopic and spectroscopic characterization of catalysts, can lead to a much deeper understanding of the reaction chemistry that is difficult to decipher from experimental work alone.

Thus, a protocol to systematically find the optimum catalyst can be developed that combines the power of theory and experiment for atomistic design of catalytically active sites and can translate the fundamental insights gained directly to a complete catalyst system that can be technically deployed.

Although it is beyond doubt computationally challenging, the study of surface, nanometer-sized, metallic clusters may be accomplished by merging state-of-the-art, density-functional-based, electronic-structure techniques and molecular-dynamic techniques. These techniques provide accurate energetics, force, and electronic information. Theoretical work must be based electronic-structure methods, as opposed to more empirical-based techniques, so as to provide realistic energetics and direct electronic information.

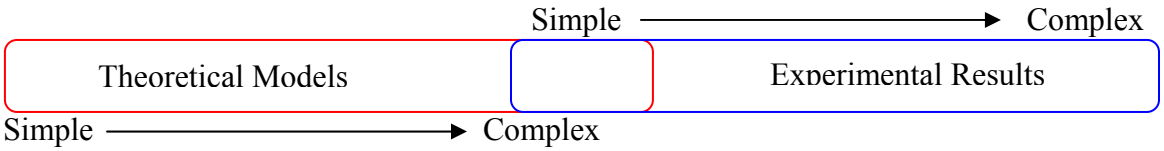

A computationally complex system, in principle, will be a model of a simple catalyst that can be synthesized and evaluated in the laboratory. It is important to point out that such a system for experimentalist will be an idealized simple model catalyst system that will probably model a "real-world" catalyst.

Thus it is conceivable that "computationally complex but experimentally simple" system can be examined by both theoretical models and experimental work to forecast improvements to obtain optimum catalyst systems.

Our Goals are as follows:

- Our initial theoretical goal will be to carry out the calculation and simulation of realistic Pt nanoparticle systems (i.e., those equivalent to experiment), in particular by addressing the issues of complex cluster geometries on local bonding effects that determine reactivity. As such, we expect in combination with experiment to identify relevant clusters, and to determine the electronic properties of these clusters.
- Our initial experimental goal will be to prepare metal carbonyl clusters, decarbonylated metal clusters, sub-nanometer metal particles, and metallic particles (~5 nm) on alumina (commercial high surface area, sol-gel processed, and mesoporous molecular sieve). We will then evaluate these systems for CO conversion efficiencies to determine the species that participates in CO oxidation catalysis.

Technical Highlights

Alumina Support Materials:
We synthesized sol-gel alumina by the reported procedure from the hydrolysis of Al(sec-$C_4H_9O)_3$, nitric acid peptization, and gelation. The material gives an amorphous X-ray diffraction between 5° and 70° 2θ. The alumina sol surface area calculated from a multipoint BET measurement without degassing is 170.82 m^2/g. Degassing equipment is now available and new BET measurements are scheduled. SEM images show some macro-pores on the surface at 4.5kx magnification but no ordered structure can be seen (Figure 1).

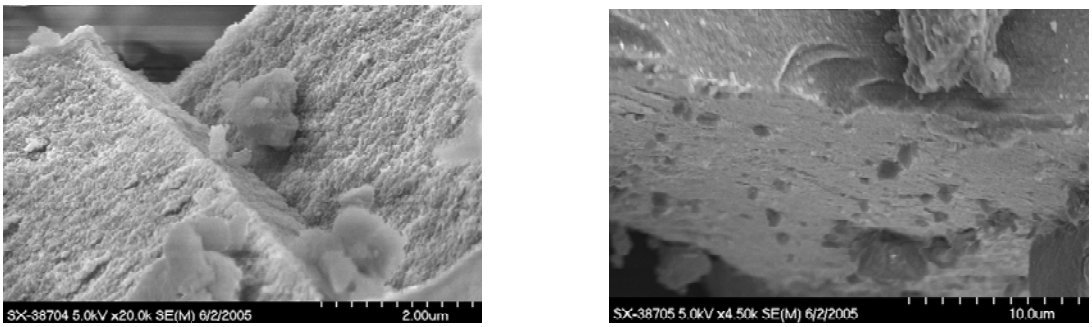

Figure 1. SEM images of sol-gel alumina at magnifications of 20.0 and 4.5 kx.

We synthesized alumina molecular sieves by a structure-templated method using cetyltrimethylammonium bromide, reported by Deng et al. [1]. X-ray diffraction of the alumina molecular sieves and SEM images (Figure 2) match reported characterization. Preliminary surface area analysis by multipoint BET analysis gave 208 m^2/g when the reaction was stirred at 128 rpm. Halving the stirring rate to 64 rpm increased the surface area to 234 m^2/g. These measurements were obtained without sample degassing. These values are about half of the reported BET surface area [~470 m^2/g]. With the degassing equipment now available the 64 rpm sample will be repeated. If the measurements still show low surface area result compared to the literature value of, further synthesis modifications will be undertaken.

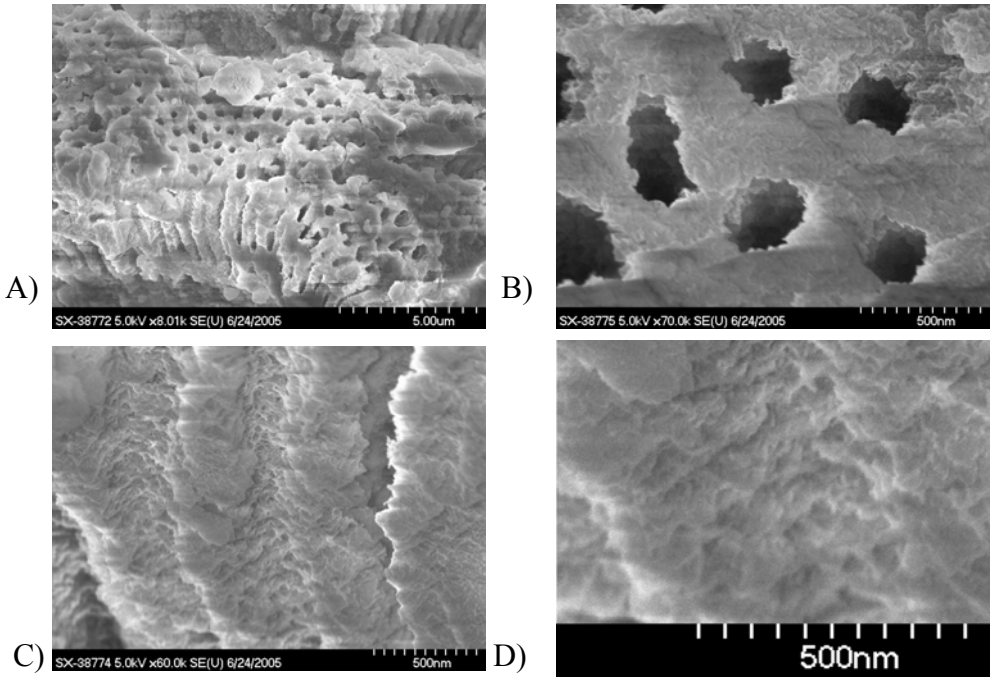

Figure 2. SEM images of the Al_2O_3 molecular sieves prepared by stirring at 64 rpm. (A) shows the surface openings of the macropores (channel openings) and the channels that extend through the material. (B) is a close-up of the channel opening at an angle. (C) is close-up of macropore channels and some of the micropores within the channels can be discerned. (D) shows an enlargement of the micropores within the channels from (C).

Since the alumina molecular sieve structure collapses at elevated temperatures, we are adding stabilizers to freshly prepared materials. We have followed structural changes by powder XRD (Figure 3) and found that incorporation of 2 wt. % La to alumina molecular sieves and calcining at 500°C/ 5.5 h in flowing air leads to an amorphous materials that does not show any crystallized phases even after additional calcining under following air at 700°C/5.5h and 900°C/5.5 h. Low intensity broad peaks, indicative of aluminum oxide, gain a small fraction of intensity as the sample is treated under harsher temperatures.

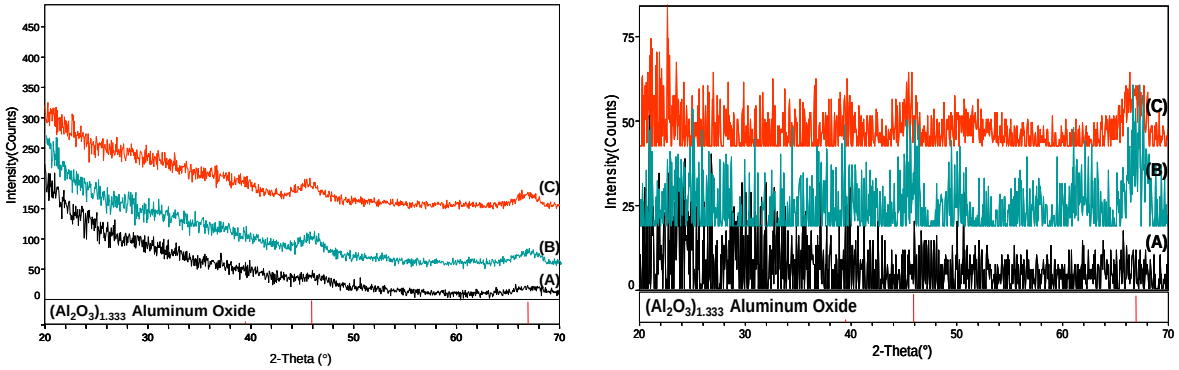

Figure 3. X-ray diffraction patterns of Al_2O_3 molecular sieves synthesized at 64 rpm, doped with 2 wt. % La and calcined under flowing air at (A) 500°C/ 5.5 h, followed by annealing under flowing air at (B) 700°C/ 5.5 h, and finished with a final annealing under flowing air at (C) 900°C/ 5.5 h. The diffraction patterns on the left are without background subtraction and those on the right are with background subtraction. Diffraction lines of aluminum oxide are of JCPDF # 75-0921.

SEM images will be obtained to determine if hierarchical nanopore structure is maintained.

Platinum-Alumina System:

While synthesis and characterization sol-gel and molecular sieve alumina is in progress, we have synthesized and characterized Pt/Al_2O_3 materials using commercially alumina. We have initiated our efforts on the synthesis of these materials and have isolated nanocluster Pt/commercial γ–alumina. The clusters have been synthesized by impregnation of γ–alumina with $H_2PtCl_6 \bullet 6H_2O$ followed by calcinations in air. Particle size images of the 2% $Pt/\gamma\text{-}Al_2O_3$ prepared by the impregnation method are shown in Figure 4. Low magnification STEM imaging shows approximately ~1 nm particles with a narrow distribution centered in 1-1.5 nm range (Figure 4 B). High magnification images obtained using the ACEM in the HAADF-STEM mode indicate the atomic make up of these 1-1.5 nm particles and confirm the presence of smaller platinum clusters, see Figure 4C-D.

Thermal treatment of this material furnishes metallic Pt/ commercial γ–alumina. We plan to make Pt/clusters on alumina. A variety of Pt clusters ($[Pt_{15}(CO)_{30}]^{2-}$, $[Pt_6(CO)_{12}]^{2-}$, $[Pt_9(CO)_{18}]^{2-}$) on MgO are known but not on aluminas [2]. We plan to prepare these clusters on a variety of aluminas (commercial γ–alumina, sol-gel alumina [2], and molecular sieve alumina [1]). We will also prepare decarbonylated clusters, nanoclusters (~10 nm) and metallic particles (100 nm) on the alumina.

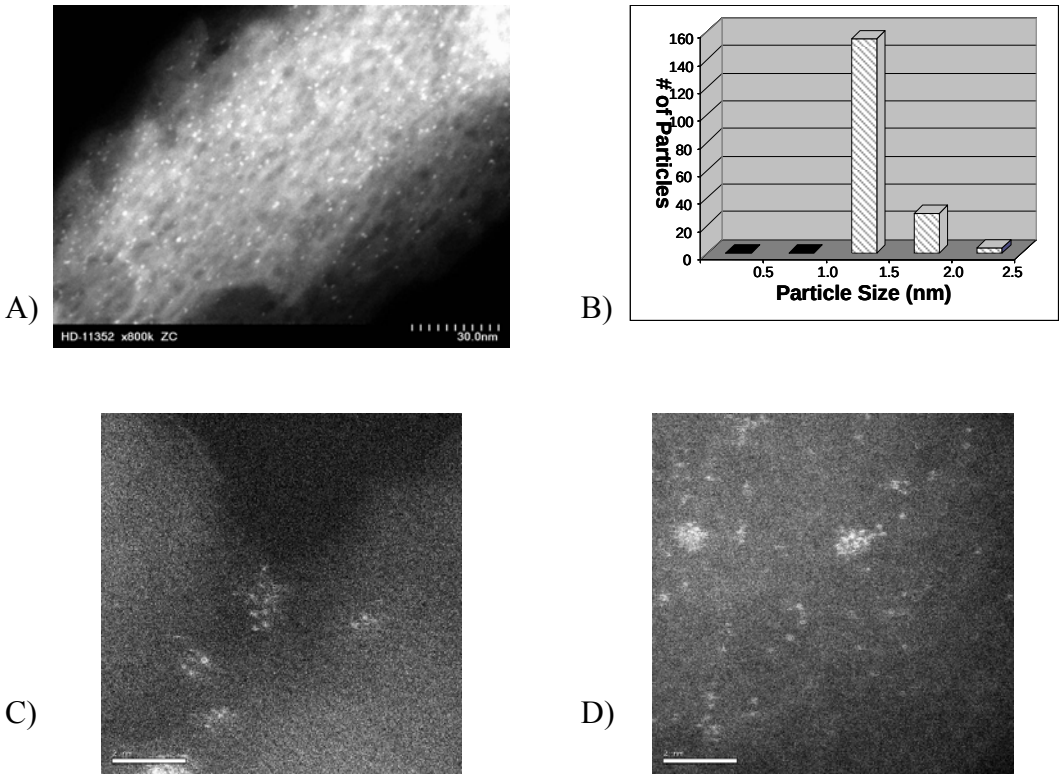

Figure 4. (A) STEM images of the 2% Pt/ γ-Al_2O_3 sample and (B) a graph of the particles size distribution. (C and D) ACEM HAADF-STEM images of 2% Pt/ γ-Al_2O_3.

The theoretical efforts, which are based on the Density Functional Theory (DFT), have so far been focused on the oxidation behavior of Pt nanoclusters. Recently we concluded the investigation of the properties of isolated pure Pt (Pt_x) and Pt oxide (Pt_xO_x and Pt_xO_{2x}) clusters (x = 1, 2, 3, 4, 5, and 10) using the DFT code VASP. Here the stoichiometries of Pt:O=1:1 and 1:2 represent, respectively, partially and fully oxidized Pt systems. The main results are summarized in Figure 5.

Structurally, the Pt_xO_x clusters ($x > 2$) prefer to form closed loops, in which the Pt atoms form the backbones in the shape of triangle, quadrangle, pentagon, etc. with each O atom occupying a Pt-Pt bridge position. The Pt_xO_{2x} series, on the other hand, form variously bent linear chain structures, in which each middle Pt atom is coordinated to four O atoms and each terminal Pt atom coordinated to three. At a certain length the chain structure becomes flexible enough to form a closed loop so that all the Pt atoms are fully coordinated. Thus both Pt_xO_x and Pt_xO_{2x} clusters prefer what may be loosely described as one-dimensional structures, as opposed to the three-dimensional matrices of the bulk oxides. They are also structurally different from the corresponding Pt_x clusters.

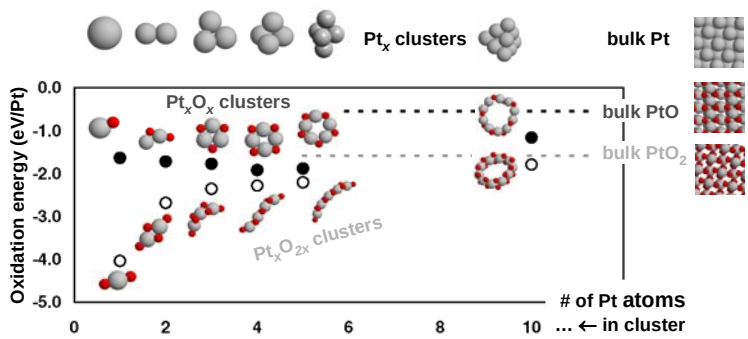

Figure 5: Oxidation energies of the Pt_xO_x (filled circles) and Pt_xO_{2x} (open circles) clusters. Black and grey dashed lines indicate bulk PtO (-0.54 eV) and β-PtO2 (-1.58 eV) formation energies, respectively. The stick-and-ball representations of the pure Pt and Pt oxide clusters are included. Red spheres represent O atoms, and grey spheres represent Pt atoms.

Another salient feature is that the oxidation of the Pt_x clusters, either partial or complete, is more exothermic (more negative oxidation energy per Pt atom) than the oxidation of bulk Pt to the bulk oxides. The oxidation energies of the Pt oxide clusters display strongly non-linear dependence on cluster size and generally become more exothermic as the cluster size decreases. This suggests that Pt clusters are more readily oxidized than bulk Pt, and that the smaller the cluster, the more readily it is oxidized. Furthermore, complete oxidation of Pt_x clusters to Pt_xO_{2x} is always favored energetically over partial oxidation (to Pt_xO_x), regardless of the cluster size.

We performed Bader charge analysis on the Pt oxide clusters and found that they differ from the bulk oxides in one more way: The Pt-O bonds in the Pt oxide clusters have considerable covalent character compared to the bulk oxides, which are predominantly ionic. Therefore we conclude that the Pt oxide clusters are distinctly different from the Pt bulk oxides structurally, energetically, and chemically. Because the structural and energetic transformations accompanying $Pt_x \rightarrow Pt_xO_x$ and $Pt_xO_x \rightarrow Pt_xO_{2x}$ depend strongly on and vary non-linearly with x, the Pt and Pt oxide nanoclusters are anticipated to exhibit widely differing activities for O_2 dissociation and catalytic oxidation.

$H_3Re_3(CO)_{12}/\gamma$-Al_2O_3 System:

We initiated this work by successfully synthesizing $H_3Re_3(CO)_{12}$ by using literature methods and confirmed its formation by IR spectroscopy [4]. In the previous report, we described the decarbonylation and characterization of decarbonylated clusters by EXAFS & XANES spectroscopy. The EXAFS parameters indicated complete decarbonylation of the rhenium. The data indicate the formation of trinuclear Re rafts, Re_3. The decarbonylated samples, modeled as trirhenium rafts, are shown by the XANES data to incorporate electron-deficient (cationic) rhenium. On the basis of a comparison of the observed XANES signature with various XANES of various reference materials, we tentatively identify the oxidation state of Re to be +4.

The $H_3Re_3(CO)_{12}/\gamma$-Al_2O_3 sample was imaged on the aberration corrected electron microscopy (ACEM) in the HAADF-STEM mode. The intact supported tri-rhenium rafts indicated by IR spectra, EXAFS, and XANES were confirmed by atomic resolution STEM images (Figure 5 and inset). In addition to tri-rhenium rafts, atomic rhenium, dimers and larger polyatomic clusters were also atomically resolved. STEM images indicate that the while slightly larger clusters were present the sample was predominately cluster comprised of 1-3 Re atoms.

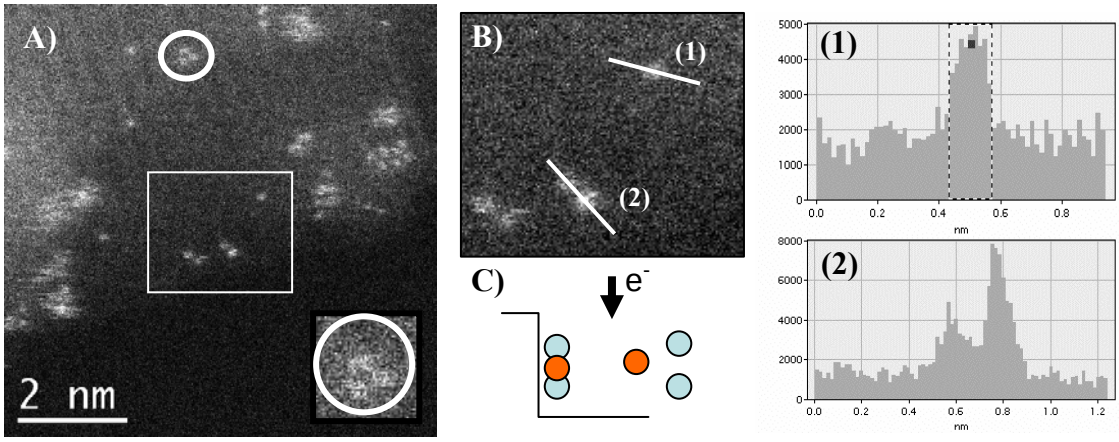

Figure 6. ACEM HAADF-STEM images of 1 wt. % Re/γ-Al_2O_3. (A) Image of $H_3Re_3(CO)_{12}/\gamma$-Al_2O_3 at 20Mx. The inset at the bottom right is an enlargement of the tri-rhenium raft located in the circle. (B) An enlargement of the boxed in area of (A). Traces 1 and 2 correspond to the particle intensity. Graphs indicate one atom in trace of particle (1) and three atoms in trace of particle (2). (C) Front and side views of Re_3 cluster, tethered to a ledge parallel to the beam direction. Above trace (2) is consistent with this cluster orientation.

STEM images of $H_3Re_3(CO)_{12}/\gamma$-Al_2O_3 treated in H_2 at 400°C to decarbonylate the clusters were also obtained using the ACEM. Images at 10-15 Mx indicated uniform clusters with diameters of ca. 0.4 – 0.8 nm. The instability of the alumina on the sample grid which caused sample drift and charging hindered efforts to captures images of atomic resolution. Rhenium has a 1.37 Å radius, which suggests that the clusters are composed of 1-3 Re atoms.

Preparation of approximately 10 Å Re clusters on commercial γ-Al_2O_3 has been completed and microstructural characterization will be reported in the next report.

Next Steps:
We plan to carry out following tasks:

- We will synthesize Pt and Re carbonyl clusters on sol-gel and molecular sieve alumina and decarbonylate these sample. This will create a matrix of samples with varying Pt particles size and oxidation on alumina substrate with increasing surface area and pore structure. Following tables summarize the already prepared and characterized samples (i.e. commercial, sol-gel, and molecular sieve support materials, the catalysts prepared are shown by √√).

  We will in initiate the evaluation of these catalysts for CO oxidation. The results will be compared with the results from theoretical calculation. If consistent, we will proceed with the evaluation of the catalysts for NO_x and hydrocarbon oxidation.

	Commercial γ-Al_2O_3	Sol-Gel γ-Al_2O_3	Molecular Sieve γ-Al_2O_3
$[Pt_6(CO)_{12}]^{2-}$	√	√	√
Decarbonylated Pt	√	√	√
Pt_n	√√	√	√
Pt_x	√√	√	√
$H_3Re_3(CO)_{12}$	√√	√	√
Decarbonylated Re	√√	√	√
Re_n	√√	√	√
Re_x	√√	√	√

- As our next step, we have begun to study how the properties of a Pt cluster vary as a function of the extent of oxidation. That is, as a Pt cluster is coordinated to an increasing number of O atoms, how its structure and energy change. This will fill in the gap of our knowledge between reduced (Pt_x), partially oxidized (Pt_xO_x), and completely oxidized (Pt_xO_{2x}) Pt clusters and is important because fractionally oxidized Pt phases are also known to appear under reaction conditions.

  We have also begun investigating the adsorption of several atomic and molecular species relevant to CO oxidation, including O, O_2, CO, and CO_2, on the Pt and Pt oxide nanoclusters. In addition, we plan on studying the kinetics of O_2 dissociation and CO oxidation. Preliminary results indicate that adsorption properties on Pt nanoclusters also display non-linear dependence on cluster size. The adsorption energies of the atomic O and O_2 molecule decrease (i.e., becoming more exothermic) as the size of the Pt cluster increases. The trend undergoes a reversal before approaching bulk surface level, whose location is unknown due to insufficient data. For CO, its adsorption energy appears to increases smoothly with cluster size.

  At the same time, we will begin modeling the Re_3 cluster. The first step will be to study the organometallic precursor and its various decarbonylated forms in gas phase, in order to understand the structure of the Re_3 raft as observed on alumina support. We will also begin working on choosing an appropriate model for the alumina support.

  The input theoretical model for Pt, Re clusters and alumina is based on the observed structures seen in experimentally synthesized materials.

Other Activities

The synthesis laboratory has been equipped to enable preparation materials under inert atmosphere to enable preparation of cluster materials as well as materials by sol-gel type processes. A reactor that allows catalyst evaluation from atmospheric pressure to 1400 psi is being set-up at ORNL (expected completion date mid-August) that will allow evaluation of catalysts.

Communication/Visitors/Travel

Bruce Gates and W. Schneider presented papers at the North American Catalysis Society meeting in Philadelphia. C.K. Narula presented this work at Eighth DOE Crosscut Workshop on Lean Emissions Reduction Simulation. L.F. Allard and C.K. Narula are scheduled to present papers based on this project at the Microscopy Society of America annual meeting and the DEER work-shop.

Publications

1. Bhirud, V.A., Narula, C., Gates, B.C., γ-Al2O3 Supported Trirhenium Rafts: Spectroscopic and Microscopic Characterization, 19th North American Catalysis Society Meeting, Philadelphia, USA, May 22-27, (2005)
2. Xu, Y.; Shelton, W.A.; Schneider, W.F.; Effect of Particle Size on the Oxidizability of Platinum Clusters; submitted to *J. Am. Chem. Soc*. (submitted)
3. Xu, Y.; Shelton, W.A.; Schneider, W.F.; Nanoscale Effects in the Reactivity of Pt Clusters towards CO oxidation, 19th North American Catalysis Society Meeting, Philadelphia, USA, May 22-27, (2005)
4. Xu, Y.; Shelton, W.A.; Schneider, W.F.; Theoretical studies based on post-Hartree-Fock and DFT methods, in *Synthesis and applications of oxide nanoparticles and nanostructures*, Ed. Rodriguez, J.A.; John Wiley & Sons; in preparation.
5. Bhirud, V.A.; Moses, M.J.; Blom, D.A.; Allard, Jr. L. F.; Aoki, T.; Mishina, S.; Narula, C.K.; Gates, B.C.; Alumina-supported Tri-rhenium Clusters Visible by Aberration-Corrected Dark-field STEM, Microscopy and Microanalysis 2005, Honolulu, USA July 31-August 4, (2005).
6. Narula, C.K.; Shelton, W.A.; Allard, L.F.; Xu, Y.; M. Moses, M.; Schneider, W.; Gates, B.; Combining Theory and Experiments in Studies of Structural Changes in LNT Materials, Eighth DOE Crosscut Workshop on Lean Emissions Reduction Simulation, University of Michigan - Dearborn, Dearborn, Michigan 48128, May 17-19, (2005).

References

1. Deng, W.; Toepke, M.W., Shanks, B.H., *Adv. Func. Mater.*, 2003, 13, 61.
2. Gates, B.C., *Chem. Rev.*, 1995, 95, 511
3. Narula, C.K.; Nakouzi, S.R., Wu, R., Goralski, C.T., Allard, L.F., *AIChE Journal,* 2001, 47, 744.
4. Andrews, M. A., Kirtley, S. W., Kaesz, H. D., *Inorg. Synth.* **1977**, 17, 16.
5. Fung, A. S., Tooley, P. A., Kelley, M. J., Koningsberger, D. C., Gates, B. C. *J. Phys. Chem.* **1991**, 95, 225.

Durability and Reliability of Ceramic Substrates for Diesel Particulate Filters

Edgar Lara-Curzio, Amit Shyam, H-T. Lin and Randy Parten
Oak Ridge National Laboratory

Objectives/Scope

To develop/implement test methods to characterize the physical and mechanical properties of ceramic diesel particulate filters (DPFs), and to implement a probabilistic-based analysis to quantify their durability and reliability.

Highlights

Water was found to lower the threshold for, and to enhance the rate of, slow crack growth in porous cordierite DPF.

Technical Progress

During the reporting period work was initiated to evaluate the static and dynamic fatigue behavior of porous cordierite test specimens according to ASTM standard test methods C1465-00 and C1576-05, which are based on flexural testing of rectangular beams. The results obtained from these tests, in particular the slow crack growth (SCG) parameters, will be compared with those obtained by double torsion testing. Work also continued to determine the effect of testing environment, and water in particular, on the SCG behavior of porous cordierite. To assess the effect of water on SCG, double-torsion tests were carried-out in water, air and mineral oil. As indicated by the results shown in Figure 1, it was found that when tested in water, in contrast to ambient air, both the threshold for SCG and the SCG exponent decreased, with the latter decreasing by as much as 30%. These results are consistent with by Kaneko et al. (2002), who reported that the strength of porous cordierite decreases significantly when tested in water as compared to air. Examination of crack trajectories after fracture testing, using scanning electron microscopy, revealed that cracks propagated along inter pore regions, but it was not possible to determine if this process was facilitated by intergranular phases, as reported by Suzuki and Baba (2003). Future work will be focused on further understanding the role of microstructure on mechanical behavior of cordierite DPFs.

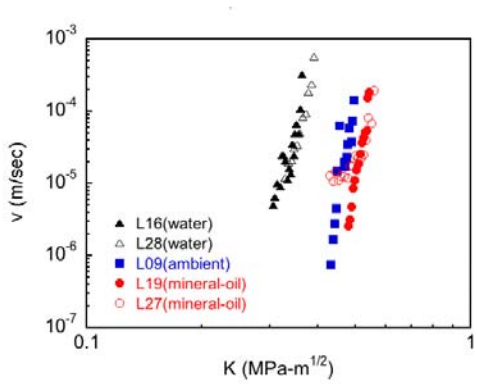

Figure 1. Effect of testing environment on the crack growth behavior of porous cordierite.

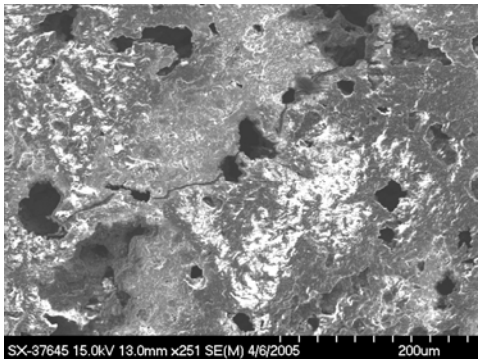

Figure 2. SEM micrograph illustrating the role of microstructure on a crack trajectory in porous cordierite.

Milestones

To organize a round-robin testing program to determine the precision in the determination of flexural strength of cordierite cellular ceramics used as DPFs. June 2005. (Completed)

Meetings

Monthly teleconferences with Cummins and Corning personnel were held during the reporting period.

References

K. Kaneko, N. Honbe, M. Matsumoto, Y. Yasutomi, T. Saitoh and T. Takigawa, "Triple-layered thick glassy grain boundaries in porous cordierite ceramics," *Acta Materialia* **50** (2002) pp. 567-604

A. Suziku and H. Baba, "Assessment of Damage Tolerance and Reliability for Ceramics," *Materials Science Research International*, **vol. 9**, No. 2 (2003) pp. 160-166

Lightweight Valve Train Materials

Jeremy S. Trethewey, John A. Grassi, Chad S. Logan
Caterpillar Inc.

Introduction

Valve train components in heavy-duty engines operate under high stresses and temperatures, and in severely corrosive environments. In contrast, the valve train components in the light-duty engine market require cost-effective reliable materials that are wear resistant and lightweight in order to achieve high power density. For both engine classes, better valve train materials need to be identified to meet market demand for high reliability and improved performance while providing the consumer lower operating costs.

Advanced ceramics and emerging intermetallic materials are highly corrosion and oxidation resistant, and possess high strength and hardness at elevated temperatures. These properties are expected to allow higher engine operating temperatures, lower wear, and enhanced reliability. In addition, the lighter weight of these materials (about 1/3 of production alloys) will lead to lower reciprocating valve train mass that could improve fuel efficiency. This research and development program is an in-depth investigation of the potential for use of these materials in heavy-duty engine environments.

The overall valve train effort will provide the materials, design, manufacturing, and economic information necessary to bring these new materials and technologies to commercial realization. With this information, component designs will be optimized using computer-based lifetime prediction models, verified in rig bench tests and validated in short-and long-term engine tests.

Program Overview

Information presented in this report is based on previous proprietary research conducted under Cooperative Agreement DE-FC05-97OR22579.

Ceramic Materials

Silicon nitride materials have been targeted for valve train materials in automotive and diesel industries since the early 1980's. Some silicon nitride material grades have reached a mature level of materials processing, capable of implementation into production. Commercial realizations have been reported in both automotive and diesel valve trains, with large-scale production underway. The silicon nitride valve train components in production are used in high rolling contact stress applications and have exhibited superior wear resistance, and longevity.

Intermetallic Materials

Titanium aluminide-based intermetallics retain their strength to elevated temperature and are highly corrosion-resistant. They are lightweight, and posses high fracture toughness. These alloys are actively being investigated for several aerospace and automotive applications.

Fourteenth Quarter Summary

Engine Testing of TiAl, Silicon Nitride and Production Valves

As outlined in previous quarterly reports (see Oct-Dec 2004), arrangements have been made to perform 1000-hour endurance engine tests in parallel on three valve materials: γ-TiAl, Si_3N_4 and austenitic steel production valves. Various destructive and non-destructive characterization tests will be performed on the valves at scheduled intervals of accumulated engine running time. These engine tests are scheduled to begin 3Q05.

Fine control of the surface finish is necessary for intermetallic (TiAl) and ceramic (Si_3N_4) valves due to their susceptibility to surface defects; e.g., pits, machining scratches, surface cracks. The valve surface finish was optimized via unique processing at Erwin Junker Maschinenfabrik (Nordrach, Germany), a company specializing in finish machining. Twelve TiAl valves and forty six Si_3N_4 valves were finish machined to the specifications of exhaust and intake valves for C15 diesel and G3406 natural gas engines (see Figure 1). Some of these valves had been finish machined once previously (Nov 2003); however, they were re-machined to correct tolerances. The valve profile and surface roughness were measured to ensure compliance with geometric and surface roughness specifications. The required R_A was achieved on all regions except for the seat contact surface. This is not considered as critical as other regions because the seat contact surface experiences compressive wear loads, rather than tensile loads.

Several adaptations must be considered to allow Oak Ridge National Laboratory's G3406 engine to accept the new "ceramic valve" design geometry. Some changes that must be addressed are:

- Seat inserts – The seat insert/valve contact angle changed from ~20º to ~45º to mitigate fillet radius stresses. Custom seat inserts were designed and fabricated to accommodate this design change.
- Stem length – The "ceramic design" valves are ~2 mm shorter than the production valves. A minor height adjustment to the bridge will be made to accommodate this length change.
- Keeper – To reduce the stress concentrations imparted at the keeper grooves, the number of grooves was reduced from two (production valves) to one ("ceramic design" valves). The groove diameter was also increased. Thus, the keeper design must be modified to accommodate these changes.
- Hot running lash – The thermal properties of the TiAl and Si_3N_4 are significantly different than the production austenitic steel valve material. This will affect the hot running lash. Therefore, care must be taken to measure and verify the specified hot running lash for all three types of valves during initial operation.
- Valve guide – The valve/guide constraint was considered but determined not to be a significant factor. The ceramic and intermetallic valves are the same diameter as the production valve and the coefficient of thermal expansion of the production valve is higher than that of either experimental material. This eliminates the concern of valve/guide interference at high temperature.

Development of a Life Prediction Tool for Advanced Materials

The effort to model a ceramic/intermetallic valve in a G3406 engine continues. An extension of the sub-contract with Jadaan Engineering & Consulting has been secured with an updated

Statement of Work. A kick-off meeting for this second round of investigation was held and current efforts are focused on acquiring the data necessary for model enhancements. An updated model that incorporates TiAl, non-axisymmetric loads and PDS (Probabilistic Design System) is expected to be complete by 4Q05.

TiAl Machining study

Machining processes account for a significant portion of the cost of valve components. This is especially true for high temperature materials such as intermetallics and ceramics since these materials are sensitive to surface features. Thus, it is necessary to identify the most economical method of machining that achieves the required specifications; e.g., geometric tolerances and surface roughness.

A series of experiments is planned to investigate the capability of three machining techniques (turning, grinding, and laser-assisted machining) on TiAl test specimens. The surface finish achieved by each technique will be quantified based on microscopy and profilometry measurements. These test specimens will then be subjected to axial stepped fatigue tests at room temperature and operating temperature to evaluate the effect of machining damage and temperature on the fatigue performance of TiAl. These tests are to be performed at Oak Ridge National Lab. Results are expected by 4Q05.

Friction study

Friction is a fundamental phenomenon in the valve train system. It behaves in both a detrimental manner (e.g., wear of valve seat contact) and beneficial manner (e.g. traction that allows retention of the rotocoil). There is currently no comprehensive database that captures the friction behavior of valve materials to peripheral components. To address this, a matrix of experiments has been developed that will explore the interaction of various valve materials (TiAl, Si_3N_4 and austenitic steel) with the materials that they contact (seat insert, valve guide, keeper and bridge). These tests will be performed on an in-house Cameron-Plint test apparatus in an environment that grossly simulates the engine operating conditions. Results from these tests will aid modeling efforts and highlight the consequences of changing valve materials from the well-known production steel to an advanced material.

ANL effort

JG Sun at Argonne National Lab is leading the effort to investigate applicable NDE techniques for valve characterization. In past reports it was shown that the laser scatter technique effectively identifies surface and sub-surface defects on Si_3N_4 specimens. Recently, an un-machined TiAl casting blank was delivered to ANL for preliminary analysis. It was determined that the laser scatter technique could detect surface defects, but not sub-surface defects because the material is not translucent.

Subsequently, vibrothermography was identified as a potential NDE technique that could detect near-surface fatigue cracks within valves and other structural engine components. Arrangements have been made to send several specimens to ANL for preliminary evaluation.

Presentations & Relevant Travel

Presentation to ORNL, DOE staff	4-27-05	Annual program review
Travel: Junker (Nordrach, FRG)	5-9-05 to 5-13-05	Witness finish machining of valves
Presentation to HTML staff	5-19-05	Update on TiAl activities
Travel: Univ. of Wis., Platteville #2	5-24-05	Kick-off meeting for modeling SOW
Presentation to ANL staff	6-6-05	Update on TiAl activities

Plans for Future Work

The primary focus of the next quarter will be preparations and execution of the ORNL G3406 engine testing of Si_3N_4 and TiAl valves. This will involve valve characterization, rig-test validation and G3406 engine modifications. Additional effort will be placed on continued development and application of the valve lifetime model. The machining and friction study will also be continued in the next quarter. Materials will be procured and preliminary results will be acquired.

Figure 1: Ti-6Al-4V shaft welded to TiAl head: a) before, and b) after finish machining.

Thick Thermal Barrier Coatings (TTBCs) for Low Emission, High Efficiency Diesel Engine Components

M. Brad Beardsley
Caterpillar Inc.

Objective/Scope

New diesel engine combustion technologies such as HCCI (Homogenous Charged Compression Ignition) have the potential to reduce emissions while maintaining engine efficiency. However, increased heat rejection with this type of combustion will require insulating materials to maintain efficiency. Two new materials, amorphous steels and quasicrystals, have shown promise as thermal barrier coatings. The low melting point of these materials (~1100-1200°C) allows them to be processed using high velocity oxygen fueled coating processes that produce coating with higher adherence and strength than plasma spraying. The higher density produced by this coating process eliminates the need for sealing of the coating structure. Thermal conductivities for the amorphous steels and quasicrystal materials have been measured to be in the range of 1.5 to 5 W/m-K. The amorphous steels have also been shown to have higher toughness than zirconia based ceramics traditionally used for thermal barriers. Material properties of the coatings will be measured for use in FEA analysis of coated components and initial prototype pistons and heads will be produced for engine testing.

Technical Highlights

Quasicrystalline and Amorphous Steel Coatings – Robotic programs to HVOF spray the flame deck of cylinder heads and the bowl of pistons are being developed. Initial spray results for the head geometry are promising in that the thickness control and roughness of the as-sprayed coating appear to be sufficient to use without post machining operations. This will greatly enhance the cost effectiveness of the coating system. Initial coating thickness will be 3.5 mm to determine the maximum impact after which the coating thickness will be optimized for cost and thermal resistance required.

Future Plans

A piston and head will be sprayed for engine testing in the next quarter. Actual engine testing will be done in 1st Qt. FY2006.

Travel

Visited Solar Turbines to discuss new bond coating materials available for TBC applications and determine their application to quasicrystal and amorphous steel coatings. Determined that the new bond coating materials were better suited to PVD type coatings.

Status of FY 2005 Milestones

Determine coating bending strength of quasicrystalline TBC. (Complete by February 28, 2005)
Delayed, will be completed by August 2005.

Produce quasicrystalline TBC piston for engine testing. (Complete by April 30, 2005)
Delayed, to be completed by July 2005.

Publications

None this period.

Processing and Characterization of Structural and Functional Materials for Heavy Vehicle Applications

J. Sankar, Z. Xu, and S. Yarmolenko
North Carolina A & T State University

Objective/Scope

Study liquid-phase sintering of yttria-stabilized zirconia.

Task

Produce the green forms of yttria-stabilized zirconia (YSZ) powders mixed with bismuth oxide powder using slurry casting method. Sinter the cast green forms and study the effect of liquid-phase sintering on the microstructures.

Technical Highlights

Reducing the manufacturing cost is urgently desired to lower the overall cost of solid oxide fuel cells (SOFCs). Many costly factors in the manufacturing processes have been identified. High energy expense in the sintering of the fuel cell components, especially the YSZ electrolyte, is on of the major causes for the cost. Usually the sintering of the YSZ powders needs a temperature higher than 1500°C for many hours to obtain a fully densified electrolyte. Reduction of the sintering temperature will save the energy for sintering and also save the investment on expensive high-temperature furnaces.

In this project, 4.5 wt. % bismuth oxide powders were added into YSZ powders. To accomplish the slurry casting, polymeric binder, dispersant, plasticizer and ethanol as the solvent were added into the powder mixture. The amount of the components and the procedures to prepare the slurry for casting are the same as published in the previous report[1]. To investigate the effect of the liquid-phase sintering on the densification of the YSZ particles with different sizes, the green forms with -325 mesh YSZ power were cast and dried firstly. A suspension of the mixed YSZ powders of 66.7 wt. % of -325 mesh, 23,1 wt. % of 56nm and 13.2 wt. % of 20nm in ethanol solution stabilized with poly(dimethyldiallylammonium chloride) (PDDA) was prepared. A thin layer was sprayed onto the dried green form substrate of the cast. The coated specimens were sintered in furnace at the maximum temperature of 1000°C. Figure 1 shows the programmed sintering cycle for the liquid phase sintering. The temperature was first raised to 100°C to eliminating the stresses due to drying of the specimen. Then it was heated up to 600°C at the ramp rate of 2°C/min, was dwelled for 2 h to remove the polymer components. The temperature was again raised to 1000°C or 1100°C at the same rate and sintering was fulfilled in 4 h. The microstructure of the sintered specimens were examined with scanning electron microscopy.

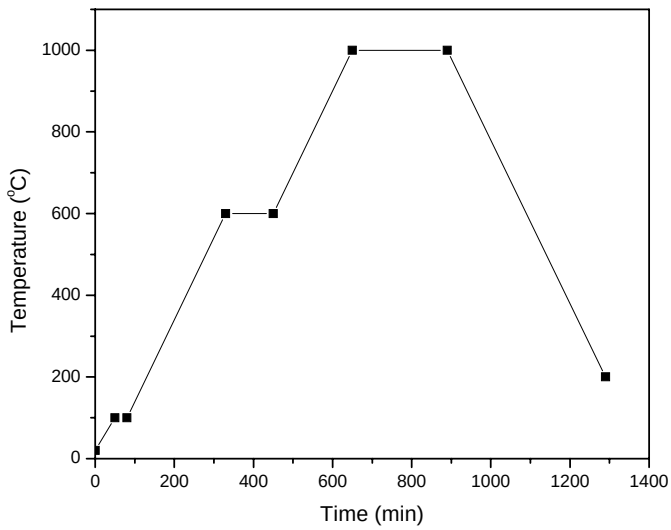

Figure1. Sintering cycle for liquid phase sintering of YSZ specimens.

Results and Discussion

Usually the purpose of liquid-phase sintering is to enhance densification rates, achieve accelerated grain growth. Liquid-phase sintering is particularly useful for the ceramics that are difficult to densify by solid-state sintering. YSZ has a melting point of about 2700°C. To obtain a fully densified YSZ electrolyte, a sintering temperature as high as 1600°C was used for solid-state sintering. If the sintering temperature can be reduced a few hundred degrees by using liquid-phase sintering, the benefit will be substantial saving in the cost to prepare the YSZ electrolytes for SOFCs. Bismuth oxide (bismite, Bi_2O_3) has a low melting point of 817°C. In addition, this oxide itself is a good oxide ion conductor, with a higher conductivity than YSZ. Therefore, it is worthwhile to study the effectiveness of liquid-phase sintering of YSZ with the presence of bismuth oxide.

Effect of the sintering temperature

A comparison of the effect of the sintering temperatures on the densification was made. Figure 2 shows the micrographs of the specimens sintering at 1000°C and 1100°C, respectively. From images in Figure 2(a) and (b) that were magnified to 20,000 times, it can be concluded that both specimens that sintered at 1000 and 1100°C are fully sintered. From the images in Figure 2(c) and (d) which were taken at a lower magnification from the same specimens mentioned above, it is shown that there are still many pores over the samples. This set of images demonstrates that the densification at 1000°C and 1100°C did not make significant difference. Therefore, a temperature of 1000°C was chosen for all the sintering thereafter. On the other hand, this experiment revealed a potential to produce porous YSZ frame structure at lowered temperatures using liquid-phase sintering.

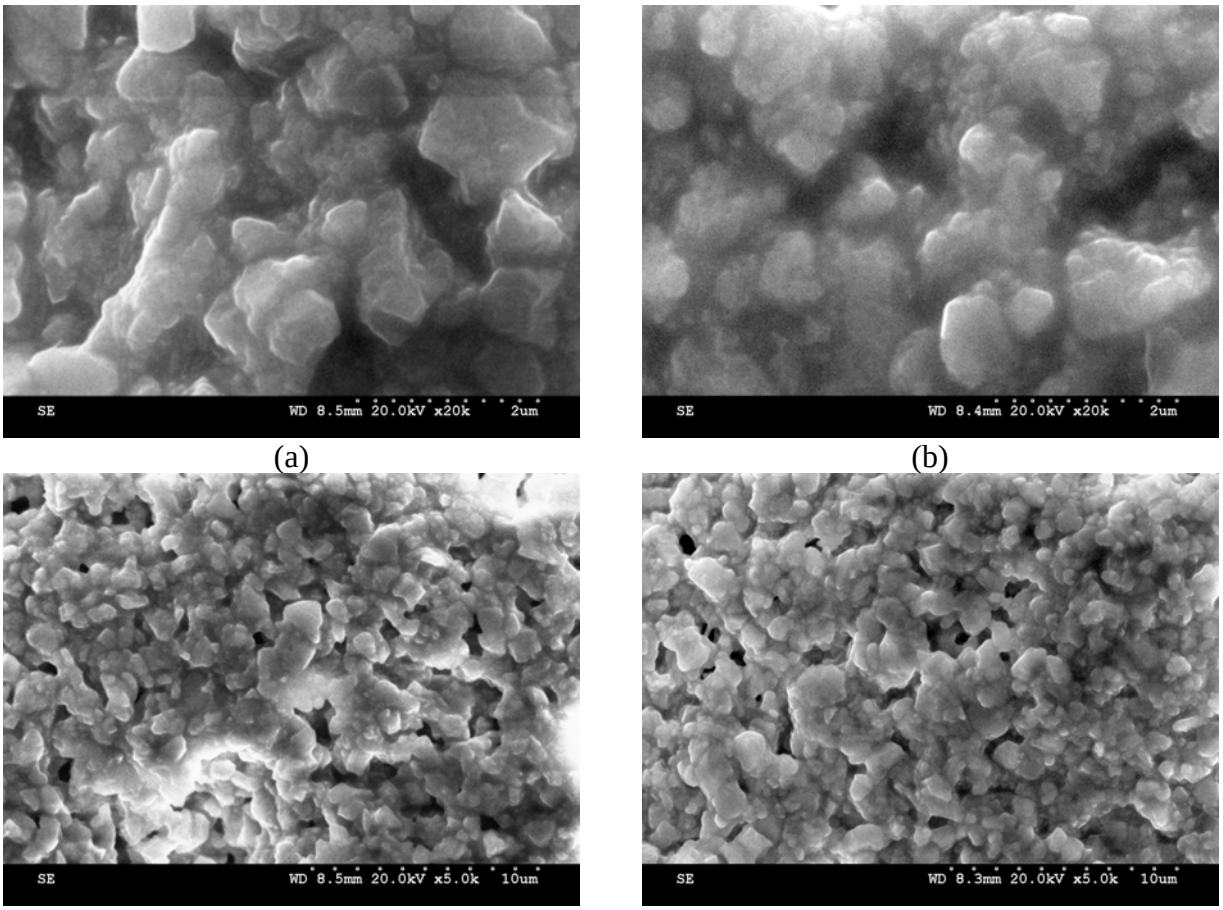

(a) (b) (c) (d)

Figure 2 Micrographs of liquid-phase sintered YSZ with addition of 4.5 wt.% of bismuth oxide sintered at different temperatures, (a) and (c) 1000°C; (b) and (d) 1100°C for 4 h.

Effect of the YSZ particle size

As is stated above, sintering experiments were conducted for the samples with substrate and coating layered structure. The substrate comprises YSZ particles of a larger size, while the coating consists of YSZ particles of mixed sizes. The purpose of doing in this way is to explore the possibility of producing a dense YSZ layer on a porous YSZ substrate using one liquid-phase sintering process. The knowledge of solid-state sintering advises that small particles have higher densification rates than the large particles during sintering because of two main reasons. First, large particles have lower packing density than the small particles. The material comprised with large particles needs more diffusion energy and time to reach densification than one with small particles. Secondly, small particles, especially nano particles have high chemical potentials than large particles. As a result, the material with small particles possesses higher diffusion rates than one with large particles. This will further enlarge the difference of the densification during sintering between materials with different particles sizes. These factors will also take effect in liquid-phase sintering.

Figure 3 shows the SEM images taken from the top and bottom surfaces of a coated specimen after liquid-phase sintering at 1000°C for 4 h. This observation proved that it is effective to

produce dense coating on porous substrate by using different particle sizes in the two different parts of the structure during liquid-phase sintering. This method can be employed in production of SOFC sandwich structures, which will reduce the manufacturing cost substantially by simplifying the fabrication process and saving sintering energy.

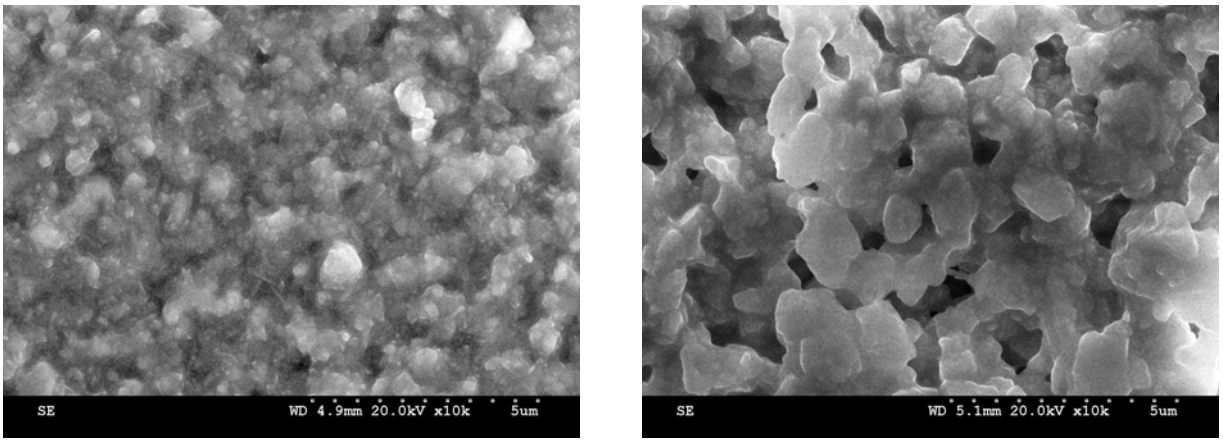

(a) (b)

Figure 3. Micrographs of the (a) coating and (b) substrate sintered at 1000 °C for 4 h in liquid phase in one process.

Conclusions

Experiments demonstrated that liquid-phase sintering is an energy-efficient process and Bi_2O_3 is an effective low melting point material to perform liquid-phase sintering of YSZ. Either dense or porous YSZ can be obtained by this sintering technique. Moreover, the effectiveness of obtaining a dense YSZ coating on porous YSZ substrate in one single sintering process is very valuable for the fabrication of SOFC structures. Future work will be on the effect of the addition of Bi_2O_3 on the ion conductivity of YSZ.

References

1. J. Sankar, Z. Xu, and S. Yarmolenko, in Heavy Vehicle Propulsion Materials Program Quarterly Progress Report for January through April 2004, ed. D.R. Johnson, prepared for US Department of Energy.

Communications/Visitors/Travel

None

Problems Encountered

None

NDE Development for Ceramic Valves for Diesel Engines

J. G. Sun and J. M. Zhang
Argonne National Laboratory

J. S. Trethewey and J. A. Grassi
Caterpillar, Inc.

Objective/Scope

Emission reduction in diesel engines designated to burn fuels from several sources has lead to the need to assess ceramic valves to reduce corrosion and emission. The objective of this work is to evaluate several nondestructive evaluation (NDE) methods to detect defect/damage in structural ceramic valves for diesel engines. One primary NDE method to be addressed is elastic optical scattering. The end target is to demonstrate that NDE data can be correlated to material damage as well as used to predict material microstructural and mechanical properties. There are three tasks to be carried out: (1) Characterize subsurface defects and machining damage in flexure-bar specimens of NT551 and SN235 silicon nitrides to be used as valve materials. Laser-scattering studies will be conducted at various wavelengths using a He-Ne laser and a tunable-wavelength solid-state laser to optimize detection sensitivity. NDE studies will be coupled with examination of surface/subsurface microstructure and fracture surface to determine defect/damage depth and fracture origin. NDE data will also be correlated with mechanical properties. (2) Assess and evaluate subsurface damage in ceramic valves to be run in bench test and in a single-cylinder-engine test. All valves will be examined at ANL prior to test, during periodic scheduled shut downs, and at the end of the planned test runs.

Technical Highlights

During this period (April-June 2005) we continued to analyze and characterize the eight ground/fractured SN235P rods. In addition, two cylindrical tensile specimens, one stainless steel and the other intermetallic TiAl (Titanium Aluminide) material, were preliminarily studied using the laser scatter method.

1. Laser Scatter Characterization of Cylindrical SN235P Ground/Fractured Rods

(1) Statistical analysis on scatter images obtained at optical wavelength of 633 nm
Laser scatter and fractography data for eight ground SN235P rods were presented in the last quarterly report. It was shown that laser scatter can identify fracture origins in all fractured rods. In this period, statistical parameters of the laser scatter data were processed and studied to examine their correlation with fracture strength. These statistical parameters include range, mean, standard deviation, skewness, skewness/standard deviation, and coefficient of variance Cv (standard deviation/mean).

Figure 1 shows fracture strength as functions of statistical parameters for the eight rods. The standard deviation and skewness in Fig. 1 generally correlate well with the fracture strength. Both show a similar trend, i.e., strength decreases with the increase of standard deviation or skewness. These results are physically reasonable. Because standard deviation is a measure of scatter intensity difference from the background, a high standard deviation indicates the presence of severe subsurface damages/defects which generate higher scattered light intensity above the

background while a low standard deviation represents weak damages with lower scattered intensities over the background. It is noted that the nondimensional parameters skewness/standard-deviation and Cv in Figs. 1c-d also show the same trend. These nondimensional parameters can be good candidates for predicting the fracture strength.

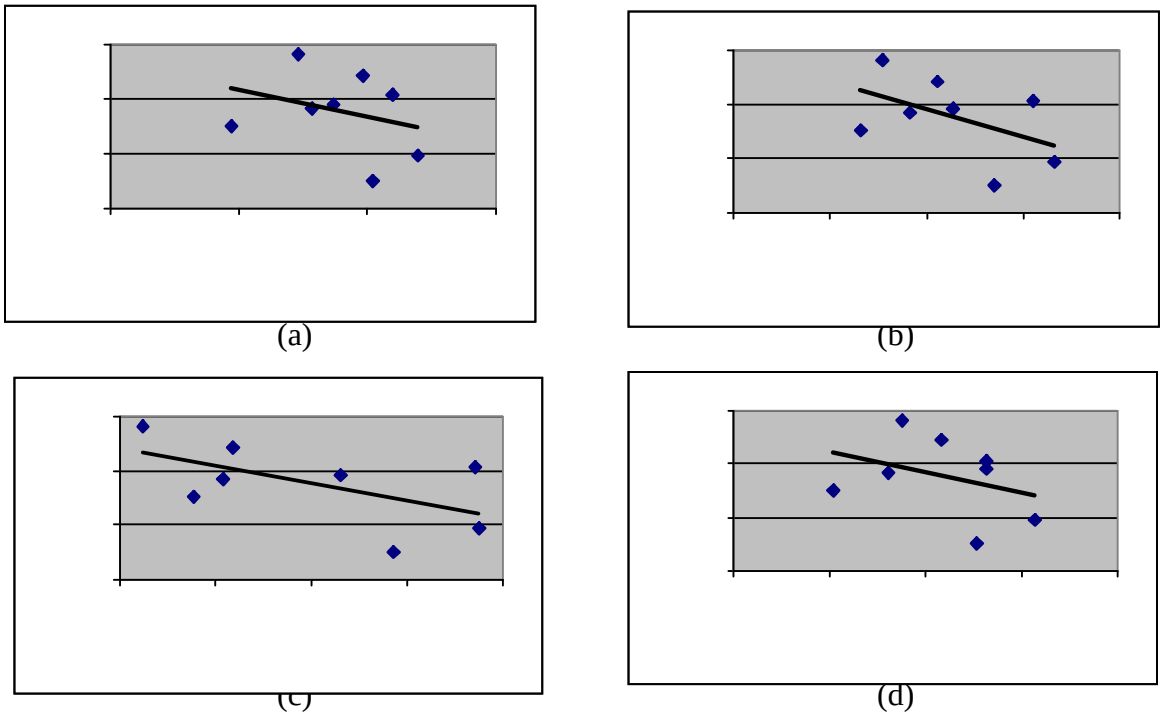

Fig. 1. Correlation of fracture strength with statistical parameters processed from laser-scatter images around fracture regions.

(2) Comparison of laser scatter images obtained at wavelengths 633 nm and 850 nm

From our previous study on silicon-nitride ceramics, it was concluded that laser light with a longer wavelength can penetrate deeper below the surface and, therefore, may reveal information from the deeper subsurface damage/defects. A longer wavelength of 850 nm was used to scan the eight ground/fractured rods and the scatter results have been compared with those obtained at shorter wavelength of 633 nm. Figure 2 shows a typical comparison (for Rod #6). Some interesting phenomena can be observed from these images. First, the surface coloration (likely contamination) contrast can be seen clearly in the scatter image of 633 nm, while this contrast is less prominent in the image of 850 nm. This is because that longer wavelength (850 nm) penetrates deeper under the surface. At longer wavelengths, the recorded signal contains more scattered light from the deep region than from the surface region. And at shorter wavelengths, the scattered signal from the surface features contribute more to the total scatter signal. Therefore, surface coloration can be seen more clearly in shorter wavelengths than in longer wavelengths. Second, comparing the cropped images in Figs. 2b and 2d for the same region that were acquired at wavelengths 633 nm and 850 nm, respectively, it is seen that there are more bright spots (subsurface scatter sites) in the image of 633 nm. This is also attributed to the deeper optical penetration at longer wavelengths. As a result, subsurface defects (likely porosities) that are very near to the surface will be captured clearly at shorter wavelength but not at longer wavelength, or at least not as prominent in the scatter image of longer wavelength.

Although additional information is revealed from scatter data acquired at longer wavelengths, laser light at these wavelengths is invisible (infrared) that pose a significant challenge for laser beam positioning and focusing. Therefore, longer wavelength will not be further used for study of cylindrical specimens.

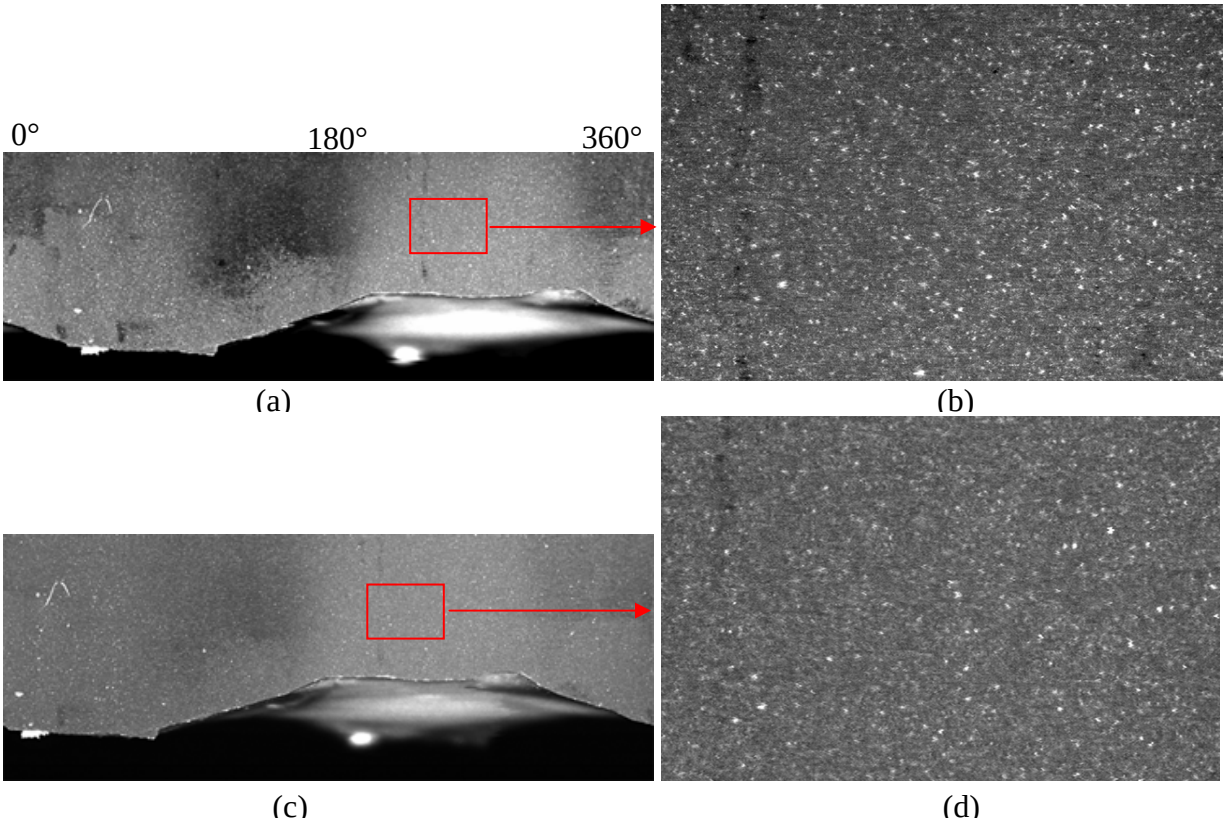

Fig. 2. Scatter images of Rod #6: at wavelength 633 nm for (a) entire circumference near fracture and (b) cropped image; at wavelength 850 nm for (c) entire circumference and (d) cropped image.

2. NDE Study of Tensile Specimens of Stainless Steel and Intermetallic TiAl Materials

As a result of program shift at Caterpillar Inc. from structural ceramics (Si_3N_4) to intermetallics (TiAl) for valve-train component application (Trethewey et al., quarterly report for the period of Jan.-Mar. 2005), NDE methods capable of detecting machining and operation damage in the surface layer of TiAl material need to be established. Laser scatter NDE method was identified to be suitable for this application. However, because there is no optical penetration for intermetallic or metallic materials, laser scatter with cross-polarization detection is used to enhance surface features such as very rough topography or surface breaking cracks. A preliminary assessment of this application was conducted for two tensile specimens shown in Fig. 3, a partially fractured stainless steel rod and a TiAl half-rod; we received these specimens from Caterpillar in late June. For the stainless steel rod, laser scatter image and photomicrograph of the middle region (marked as 1 in Fig. 3) are shown in Fig. 4. The crack can be seen clearly in scatter image and photomicrograph, and the longitudinal machining marks can also be observed in this region. Similar results were obtained for the TiAl specimen. These results will be further analyzed and presented in the next report.

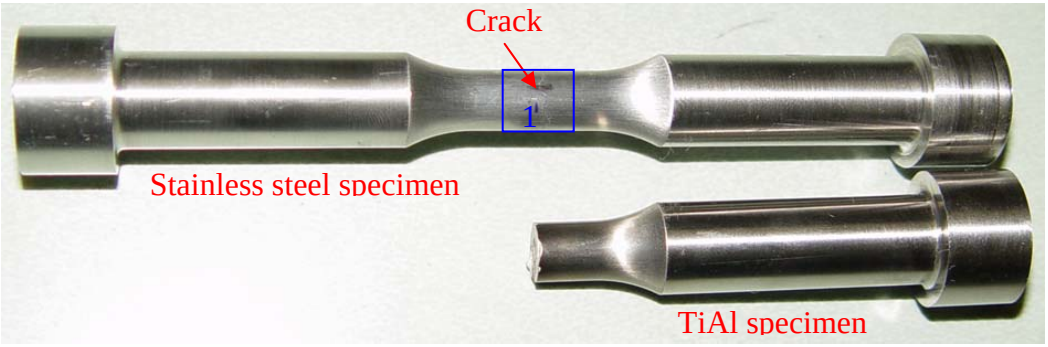

Fig. 3. Photograph of stainless steel rod and TiAl half-rod.

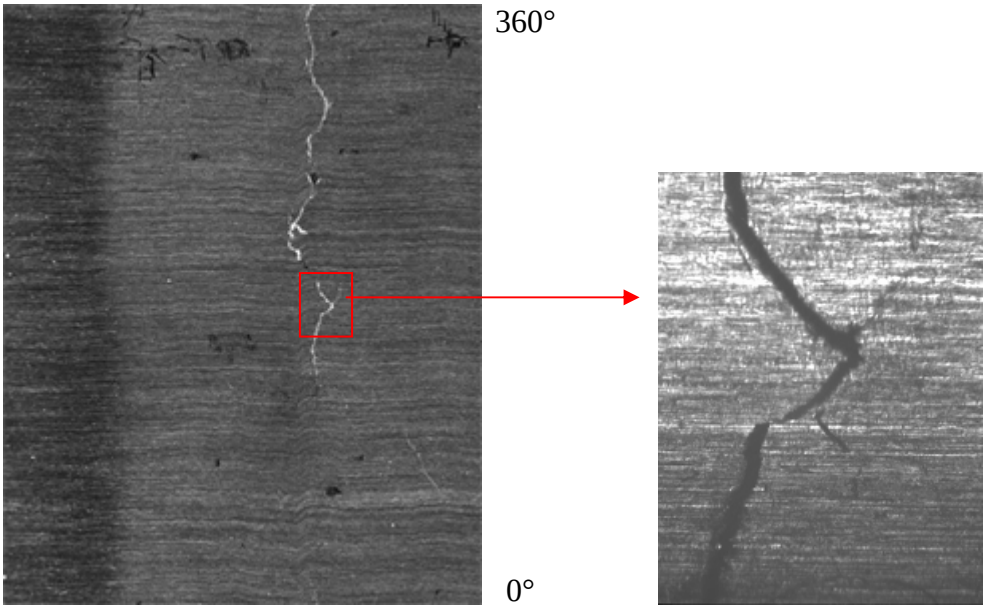

(a) (b)

Fig. 4. Stainless steel rod: (a) scatter image of region 1 marked in Fig. 3; (b) 50X photomicrograph of crack region.

Status of Milestones

Current ANL milestones are on schedule.

Communications/Visits/Travel

J. G. Sun visited Caterpillar Inc. on June 6, 2005 to discuss project issues.

Jeremy Trethewey and Chad Logan of Caterpillar Inc. plan to visit ANL on July 7 to discuss project schedule for valve engine test and NDE analyses.

J. G. Sun plans to present a paper entitled "Characterization of Subsurface Defects in Ceramic Rods by Laser Scattering and Fractography Methods" at the 32nd Annual Review of Progress in Quantitative Nondestructive Evaluation, Bowdoin College, Brunswick, Maine, July 31-August 5, 2005.

Problems Encountered
None this period.

Publications
None this period.

Durability of Diesel Engine Component Materials

Peter Blau and Jun Qu
Oak Ridge National Laboratory

John Truhan
University of Tennessee

Objective/Scope

The objective of this effort is to enable the development and use of more durable, low-friction moving parts in diesel engines for heavy vehicle propulsion systems. The scope of candidate materials and coatings broadly includes metallic alloys, intermetallic compounds, ceramics, or composite materials depending on which is best-suited for each application. Parts of current interest include scuffing-critical components, such as fuel injector plungers and exhaust gas recirculation (EGR) waste gate bushings. Bench-scale simulations of the rubbing conditions in diesel engine environments are developed and used to study the accumulation of surface damage, and to correlate it with the properties and compositions of the surface species. The effects of mechanical, thermal, and chemical factors on scuffing and reciprocating sliding wear are being determined. Results are used to develop graphical methods for scuffing performance mapping and to select materials for durability-critical engine components. In FY 2005 an analytical model for selecting materials for scuffing-critical applications is being developed and validated. Also in FY 2005, a new task was initiated to determine how to engineer the surfaces of titanium alloys to make them more suitable for friction- and wear-sensitive engine components. Approaches include thermal oxidation to create thin lubricating layers.

Technical Highlights

Surface Engineering of Titanium Alloys using Thermal Oxidation. Recent experiments have shown promising results for using thermal oxidation treatments to significantly reduce the friction coefficient and wear rate of titanium alloy Ti-6Al-4V under diesel oil-lubricated conditions. The new ASTM G 181 standard piston ring/liner friction test and a companion standard for wear being developed by ORNL, also under DOE/OFCVT sponsorship, were used to perform reciprocating sliding friction tests in diesel engine oil. Comparisons with cast iron liner materials were made using production grade, Cr-plated diesel engine piston rings (Caterpillar C-15 engine).

Treatment of the Ti alloy surfaces involves elevated temperature exposure to air or an oxygen-rich environment. This simple heat treatment produces a titania surface layer and a TiN-containing diffusion layer underlying it. Figure 1 shows that the steady-state friction coefficients for diesel engine production-grade piston rings against the thermally-oxidized titanium in 15W40 oil are essentially the same as those for gray cast iron. In contrast, non-treated titanium alloys exhibited more than triple the friction coefficient.

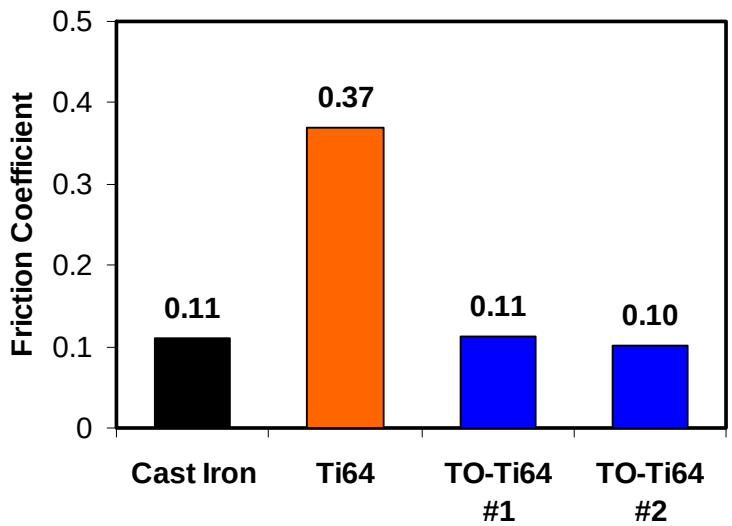

Figure 1. Steady-state friction coefficient for production diesel engine rings sliding against cast iron, non-treated titanium alloy, and thermally-oxidized (TO) titanium alloy.

The Knoop microindentation hardness of the surface of the TO-treated Ti-6Al-4V was 7 times higher than that for non-treated alloy. As shown in Table 1 and illustrated by the wear scar images in Figures 2 (a-c), the normalized wear rates for the TO surface were an astounding 60,000 times lower than those for non-treated Ti-6Al-4V, and a factor of about 32 lower than that for the cast iron. The test on the non-treated Ti alloy (Figure 2(b)) had to be terminated after only 11 minutes of running because the ring had worn too far into the flat specimen.

Table 1.
Wear Rates for Piston Rings against Cast Iron, Titanium Alloy, and Thermally-Oxidized (TO) Titanium Alloy in 15W40 Diesel Oil

	Cast Iron	Ti-6Al-4V	TO Ti-6Al-4V
Test load (N)	240	130	240
Test duration (hours)	6	0.2	6
Wear rate (mm^3/N-m)	1.9×10^{-7}	3×10^{-4}	5.9×10^{-9}

These promising results suggest that Ti-based engine components that involve sliding contact could be protected by a TO treatment. The reason for this behavior may involve both surface hardening effects and changes in the chemical reactivity. Surface chemistry studies performed in conjunction with this work have shown that the treated surfaces form beneficial anti-wear films in the presence of traditional oil additives. A program highlight concerning these encouraging, new results has been prepared and sent to DOE/OFCVT.

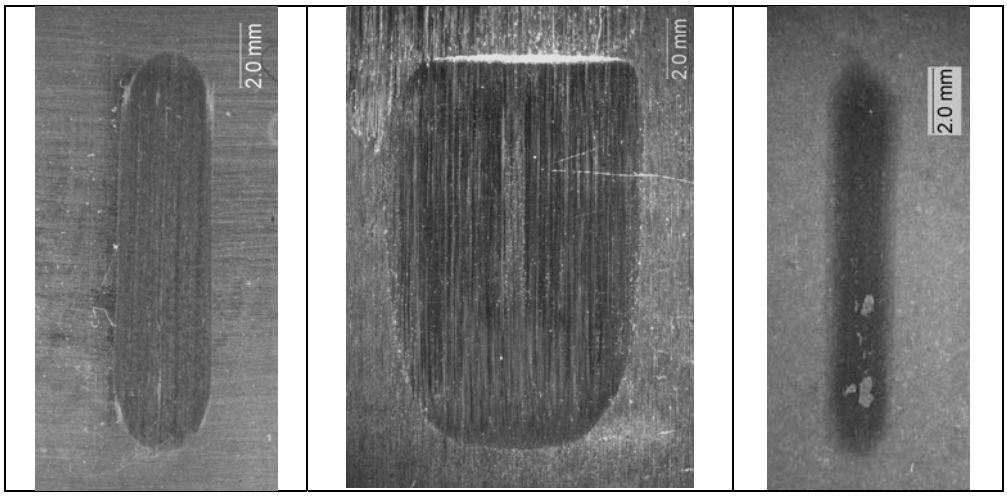

(a) (b) (c)

Figure 2. Wear scars after diesel oil-lubricated piston ring wear tests on (a) cast iron, (b) Ti-6Al-4V, (c) thermally-oxidized Ti-6Al-4V.

Future Plans

1) Continue the development of the scuffing model, described in previous reports, to involve the mechanics of failure of boundary lubricating films.

2) Continue to investigate the mechanisms by which thermal oxidation improves the durability of titanium materials for diesel engine components and determine the longevity of TO films in longer experiments.

Travel

None this period.

Status of Milestones

1) Prepare transition diagrams for current and promising, new fuel system materials that exemplify the relationship between real contact pressure, surface finish, and the onset of scuffing in diesel fuel environments. (March 31, 2004 - completed)

2) Develop a conceptual model for selecting materials and their optimal surface finishes for scuffing applications in diesel engines. (September 30, 2004 - completed**)**

3) Report on the results of research to improve the friction and wear characteristics of titanium alloys by applying surface engineering methods like thermal oxidation and controlled surface patterning. (June 30, 2005 – completed. Highlight submitted to DOE, journal article in preparation.)

4) Develop mechanistic model for scuffing processes in boundary-lubricated fuel injector plunger materials. (September 30, 2005)

Publications and Presentations

J. Qu, J. J. Truhan, P. J. Blau (2005) "Scuffing Transition Diagrams for Heavy Duty Diesel Fuel Injector Materials in Ultra Low-Sulfur Fuel-Lubricated Environment," accepted for the journal *Wear*.

Life Prediction of Diesel Engine Components

H. T. Lin, T. P. Kirkland, A. A. Wereszczak, M. K. Ferber
Oak Ridge National Laboratory

Jeremy Trethewey
Caterpillar, Inc.

Objective/Scope

The valid prediction of mechanical reliability and service life is a prerequisite for the successful implementation of structural ceramics and advanced intermetallic alloys as internal combustion engine components. There are three primary goals of this research project which contribute toward that implementation: the generation of mechanical engineering data from ambient to high temperatures of candidate structural ceramics and intermetallic alloys; the microstructural characterization of failure phenomena in these ceramics and alloys and components fabricated from them; and the application and verification of probabilistic life prediction methods using diesel engine components as test cases. For all three stages, results are provided to both the material suppliers and component end-users.

The systematic study of candidate structural ceramics (primarily silicon nitride) for internal combustion engine components is undertaken as a function of temperature (< 1200°C), environment, time, and machining conditions. Properties such as strength and fatigue will be characterized via flexure and rotary bend testing.

The second goal of the program is to characterize the evolution and role of damage mechanisms, and changes in microstructure linked to the ceramic's mechanical performance, at representative engine component service conditions. These will be examined using several analytical techniques including optical and scanning electron microscopy. Specifically, several microstructural aspects of failure will be characterized:

(1) strength-limiting flaw-type identification;
(2) edge, surface, and volume effects on strength and fatigue size-scaling
(3) changes in failure mechanism as a function of temperature;
(4) the nature of slow crack growth; and
(5) what role residual stresses may have in these processes.

Lastly, numerical probabilistic models (i.e., life prediction codes) will be used in conjunction with the generated strength and fatigue data to predict the failure probability and reliability of complex-shaped components subjected to mechanical loading, such as a silicon nitride diesel engine valve. The predicted results will then be compared to actual component performance measured experimentally or from field service data. As a consequence of these efforts, the data generated in this program will not only provide a critically needed base for component utilization in internal combustion engines, but will also facilitate the maturation of candidate ceramic materials and a design algorithm for ceramic components subjected to mechanical loading in general.

Technical Highlights

Studies on the mechanical properties of NT551 silicon nitride valve stems after 500-h bench rig test have been completed during this reporting period. The objective of this study was to see whether the 500-h bench rig test would introduce any surface damage to the valve stem surfaces, and thus degrade the mechanical strength. The half-cylindrical valve stems were tested using 30/60 mm spans fixture with 2 mm/min crosshead speed at room temperature. Figure 1 shows the uncensored Weibull strength distribution of these half-cylindrical valve stems. The mechanical results show a characteristic strength of 1135 MPa, and Weibull modulus of 12.7, comparable and/or better than those as-machined cylindrical samples reported previously. It's anticipated that the strength-limiting flaw would be the transverse surface machining grooves, as indicated in previous report. However, detailed fractography and SEM analysis will be carried out and results will be summarized in the next report.

Previous studies on silicon nitride components showed that the samples machined from first-stage turbine blades and nozzles exhibited 15-20% lower strength than those machined from production billets due to the differences in microstructure and chemical compositions. Thus, it is critical to carry out similar characterization effort for TiAl components, and provide mechanical database for probabilistic component design verification and life prediction efforts of end users. A half of TiAl turbo wheel was acquired from Caterpillar, as shown in Fig. 2. Machining of biaxial discs from the airfoil region for mechanical strength evaluation will be initiated during the next reporting period.

Status of Milestones

Milestone: "Complete testing and analysis of prototype silicon nitride valves after bench rig testing." On schedule.

Communications / Visitors / Travel

Communication with Jeremy Trethewey at Caterpillar on the on the update of the mechanical data of half-cylindrical valve stems after 500 h bench rig test.

Monthly meeting with Jeremy Trethewey Caterpillar and Tim Theiss at NTRC on the updated status of engine testing of Si_3N_4 and TiAl exhaust valves.

Visit Jeremy Trethewey and Nan Yang at Caterpillar to discuss research plans on TiAl alloy as well as update of Si_3N_4 engine testing, May 19, 2005.

Communications with Jeremy Trethewey and Nan Yang at Caterpillar on the mechanical property characterization of TiAl components.

Problems Encountered

None.

Publications

None

References

1. H. T. Lin and M. K. Ferber, "Characterization of Mechanical reliability of Silicon Nitride Microturbine Rotors," *Key Engineering Materials* Vol. 287 (2005), pp. 393-403.

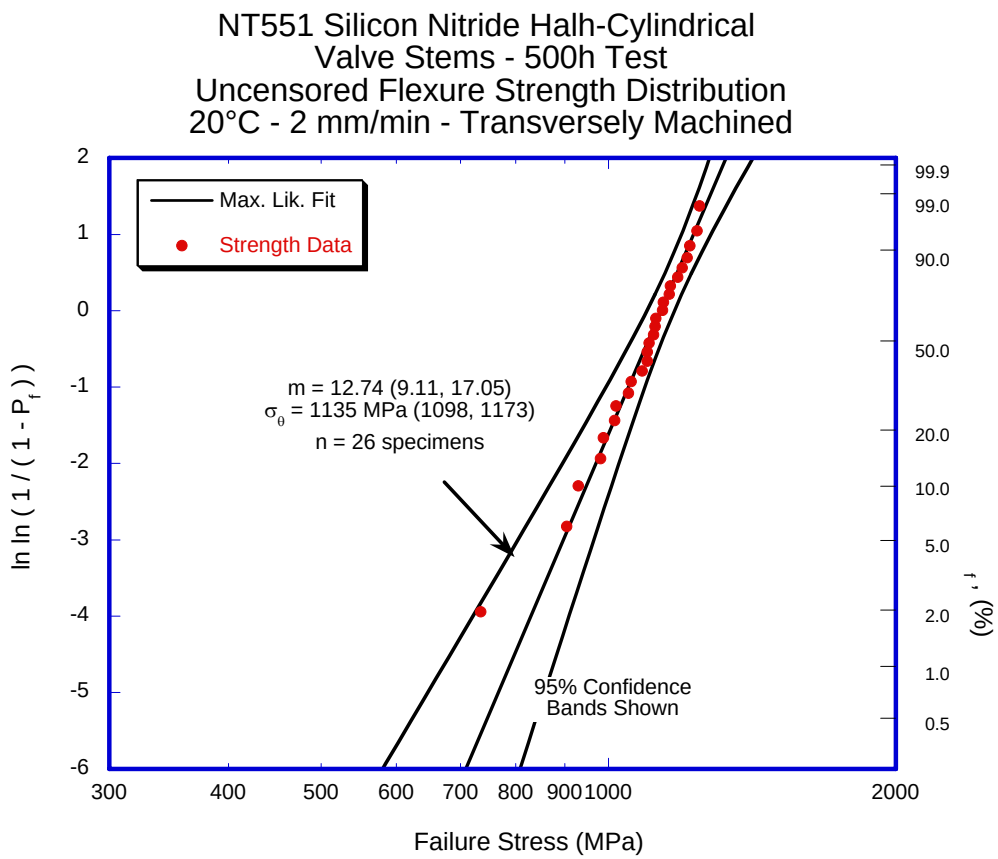

Figure 1. Strength distribution of 500-h-tested Norton NT551 silicon nitride half-cylindrical valve stems transversely machined and tested at 20°C.

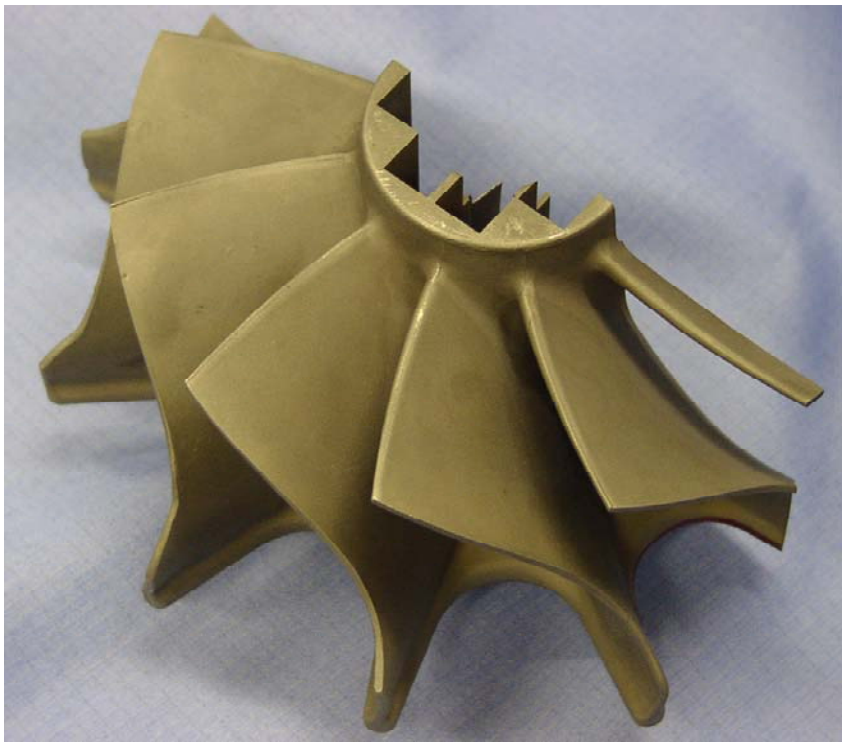

Figure 2. Photo of half of the machined TiAl turbo wheel acquired from Caterpillar for component characterization effort.

Low-Cost Manufacturing of Precision Diesel Engine Components

P. J. Blau and Jun Qu
Oak Ridge National Laboratory

Objective/Scope

The objectives of this effort are (1) to identify and investigate cost-effective processes to machine precision components of advanced materials for diesel engines and (2) to develop and use methods to characterize the effects of machining on the surface quality and performance of advanced engine materials.

Technical Highlights

New cutting tool materials for high-speed titanium machining. Titanium alloys require special machining procedures to ensure high stock removal rates, ensure excellent surface quality, and suppress chip ignition. New cutting tool materials are being investigated for possible use in machining of Ti alloys in conjunction with ORNL's participation in the Third Wave Systems high-speed titanium machining consortium (see previous quarterly reports). One potential tool material is a TiC-Ni_3Al matrix composite (cermet) which was developed at ORNL. A TiC (95 vol. %)-Ni_3Al composite was been prepared with the help of T. Tiegs, and tooling inserts were machined by wire EDM followed by abrasive hand-finishing of the cutting edges.

Preliminary cutting experiments on titanium at University of Michigan (Rui Li and Albert J. Shih), indicated higher cutting forces for the TiC-Ni_3Al tool compared to the WC-Co tool. That was probably due to its blunter cutting edge. However, unlike the abrasive or adhesive wear that limits tool life on other tool materials, chipping problems limited the TiC-Ni_3Al tool life. Assuming that the short life was caused by porosity (up to 15 μm in pore size), a cermet with a higher concentration (9 vol. %) of Ni_3Al was prepared. The larger binder content was intended to eliminate or reduce porosity and increase the fracture toughness as well. The Vickers microindentation hardness (200g-f) of the cermets is compared to that of a commercial WC-Co tooling material in Table 1. Figure 1 shows that the microstructure of the second TiC cermet was nearly pore-free.

Table 1. Microindentation Hardness of Cermets

Material	HV (GPa)
TiC-Ni_3Al(5%)	20.6
TiC-Ni_3Al(9%)	17.3
WC-Co(6%)	18.5

The experimental TiC-Ni_3Al tool inserts were tested by turning grade-2, commercially pure titanium at 0.41, 0.82, and 3.25 m/s cutting speeds, 0.254 mm/rev feed, and a 1.0 mm depth of cut. In all cases, the axial, radial, and tangential cutting forces for the TiC cermet tools were higher than those for the WC-Co insert.

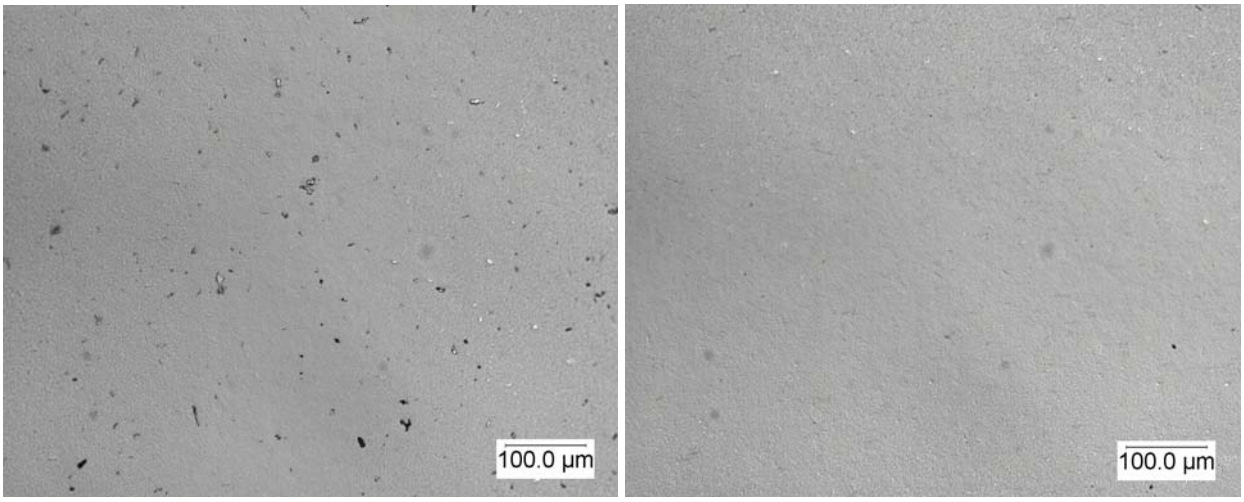

(a) TiC (95 vol. %)-Ni_3Al (b) TiC (91 vol. %) -Ni_3Al

Figure 1. Microstructures of TiC-Ni_3Al cermets.

In these experiments, 'tool failure' was defined as a sudden, dramatic increase in cutting forces. Based on that criterion, Table 2 lists the tool life of the TiC-Ni_3Al tools compared with a WC-Co tool at the highest surface speeds. Unlike the progressive tool wear observed on the WC-Co, edge chipping was the dominant failure mode for the TiC-Ni_3Al tools, especially at the higher cutting speeds. Significantly different tool lives (9.2 and 33.7 seconds at 3.25 m/s) were obtained using two different tips on the same TiC-Ni_3Al(9%) insert, suggesting non-uniformity of the microstructure, non-consistent sharpening characteristics of the cutting edges, or both.

Table 2. Tool Life in Machining of CP Ti

Tool insert	s = 0.82 m/s	s = 3.25 m/s
TiC-Ni_3Al (5%)	18.4	15.3
TiC-Ni_3Al (9%)	>294.4	9.2 (tip #1) 33.7 (tip #2)
WC-Co	*Not tested*	69

The difficulties of sharpening the edges of poly-phase ceramic composite materials may be a problem for TiC-based cermets. Therefore, during the next quarter, several additional tests will be run to verify the current results, but if the results are not encouraging, work with the two cermets as cutting tools will be discontinued.

Future Plans

(1) Conduct instrumented grinding tests on cermet materials to investigate the effects of hard particle content on grindability and surface quality.

(2) Continue to participate in the development and validation of high-speed machining models for titanium and other materials within the Third Wave Machining Consortium.

(3) Continue to investigate nickel aluminide/titanium carbide cermets as cutting tools to determine if they are viable.

(4) Develop plans for a new initiative in non-traditional machining of advanced materials.

Travel

J. Qu attended the Third Wave Systems (TWS) 2005 Software Users Conference on May 4, 2005, and the short course on machining modeling on May 5, 2005. Both events were held in Dearborn, Michigan. In addition, Qu visited Dr. Albert Shih at the University of Michigan, Ann Arbor.

FY 2005 Milestone

1) Complete an investigation on the effects of grinding and related abrasive removal processes on surface quality in advanced cermets. **(06/05)**

Presentations and Publications

None.

Cost-Effective Machining of Titanium Alloys

Albert Shih
University of Michigan

Objective/Scope

The objective of this research is to investigate new technologies for cost-effective machining of Ti alloys. Experiments and modeling of the turning and drilling of titanium alloys and new tool materials are investigated.

Technical Highlights

In the past quarter, experiments of the drilling of titanium alloys were conducted to study the feasibility of high speed drilling of Ti-6Al-4V. On high speed drilling of Ti-6Al-4V, the effect of cutting fluid on the drill life was studied using a lathe. The turning test of new tool material was also continued. The TiC (91%)-Ni_3Al (9%) metal matrix ceramic (MMC) with smaller porosity compared with TiC (95%)-Ni_3Al (5%), prepared by Oak Ridge National Lab, was tested as new tool material for turning CP Ti. The drilling temperature experiment was setup and inverse heat transfer analysis was developed to analyze the high drill temperature when drilling CP Ti. Four thermocouples were embedded in the drill flank face and wired via the drill coolant holes for temperature measurement. A thermal finite element model of the spiral point drill and the inverse heat transfer method were proposed with experimentally measured drill temperature as the input to study the detailed drill temperature distribution in drilling of CP Ti.

1. High Speed Drilling of Ti-6Al-4V

Due to the inherent material properties, the machinability of Ti alloys is poor in terms of tool life [1-4]. In order to increase the productivity, high speed is required in machining practice. High cutting speed results in the high cutting temperature and rapid tool wear. It is the goal of this research to investigate limits in Ti drilling and study the effect of cutting fluid on the drill life under the high speed drilling condition.

1.1. Experimental setup and experiment design

The experiment was conducted in a Fadal computer numerical control vertical machining center. The tool was uncoated WC-Co (Kennametal grade K715 with 9.5% Co) spiral point drill with 4.0 mm diameter, marked as WC-Co Spiral, which was selected on the base of results of the last quarter. The workpiece was a 6.35 mm thick Ti-6Al-4V plate. A Kistler 9273A piezoelectric dynamometer was used to measure the thrust force and torque in the drilling process.

The experiments were conducted at two spindle speeds, 13,500 and 14,700 rpm, which correspond to 168 and 183 m/min peripheral cutting speed, respectively, and constant 0.051 mm/rev feed. These speeds are way beyond the recommended cutting speed commonly used in practice. Both dry cutting and cutting with cutting fluid CIMTECH 310 (7% concentration), a synthetic metalworking fluid recommended for Ti machining, were tested. Thrust force, torque, and drill life were compared under these conditions.

1.2. Results and discussions

Ti drilling at high speed has known to be difficult. Using HSS Twist drill, the drill melted at the second hole with the spindle speed only 1470 rpm under dry condition and 2200 rpm with the application of cutting fluid, as reported in the last quarter. Using the WC-Co spiral point drill, the drill can survive at very high spindle speed. Table 1 lists the number of holes drilled at high speed drilling conditions.

Table. 1. Summary of drill life with high spindle speed.

	Number of holes drilled	
Spindle speed (rpm)	Without cutting fluid	With cutting fluid
14,700	6 and 10 (two tests)	14
13,500	6	58

As reported in the last quarter, without using cutting fluid, drill broke after drilling 6 to 10 holes on Ti-6Al-4V at 14,700 rpm spindle speed or 183 m/min drill peripheral cutting speed. With the application of cutting fluid, the tool broke at 14th hole. The cutting fluid did not increase the drill life significantly. The possible reason is that the cutting fluid can not enter the cutting region due to the centrifugal force under such high drill rotational speed. The Sabre machining center at ORNL is capable of coolant through the spindle and holes inside the drill. This can deliver coolant to the critical area and will be tested.

Fig. 1 shows the thrust force and torque when drilling with cutting fluid. The torque curves show abrupt towering part at the end of drilling process. Because Ti chips are continuous, chip ejection becomes very difficult at high spindle speed and feed rate. The packed chips in the drill flute increase the torque and finally result in the breakage of the drill body at the last hole. Before the failure in the 14th hole, the increase in torque became apparent but the force does not change significantly until the drill broke. It indicated that the peripheral of the cutting edge started to wear out near the end of drilling.

Because the tool life normally exponentially decreases with the increasing cutting speed and the drill life is short even with cutting fluid at 14,700 rpm spindle speed, lower spindle speed 13,500 rpm was tested. At 13,500 rpm spindle speed, the peripheral cutting speed is 168 m/min and the feed rate is 11.4 mm/s. At such speed, the penetration of the 6.35 mm thick Ti plate only takes 0.56 s, only 0.06 s slower than 14700 rpm spindle speed. Without cutting fluid, the drill life was also short, just 6 holes. Fig. 2 shows the thrust force and torque under this condition. The thrust force and torque increased sharply when the drill broke.

Although the drill life did not increase at lower spindle speed under dry drilling condition, the drill life was found to increase significantly up to 58 holes when the cutting fluid is applied. Fig. 3 shows the thrust force and torque. Gradual increase of the thrust force was found with the hole numbers, indicating the gradual wear of the drill chisel and cutting edges. Compared with results of 14700 rpm, no abrupt towering part can be found at the torque curves. This is the result of cutting fluid which contributes to the decreased cutting temperature and friction between the chip and tool flute, and drill body and hole wall.

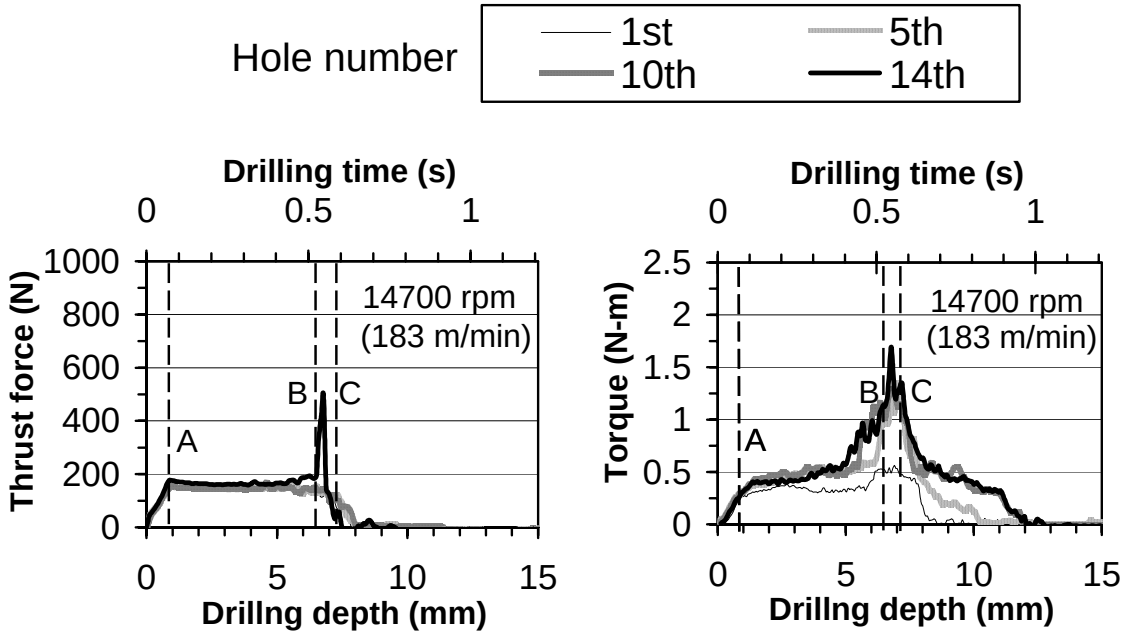

Fig. 1. Thrust force and torque of high speed drilling of Ti-6Al-4V at 14,700 rpm (183 m/min peripheral speed) and 12.5 mm/s feed rate and with cutting fluid.

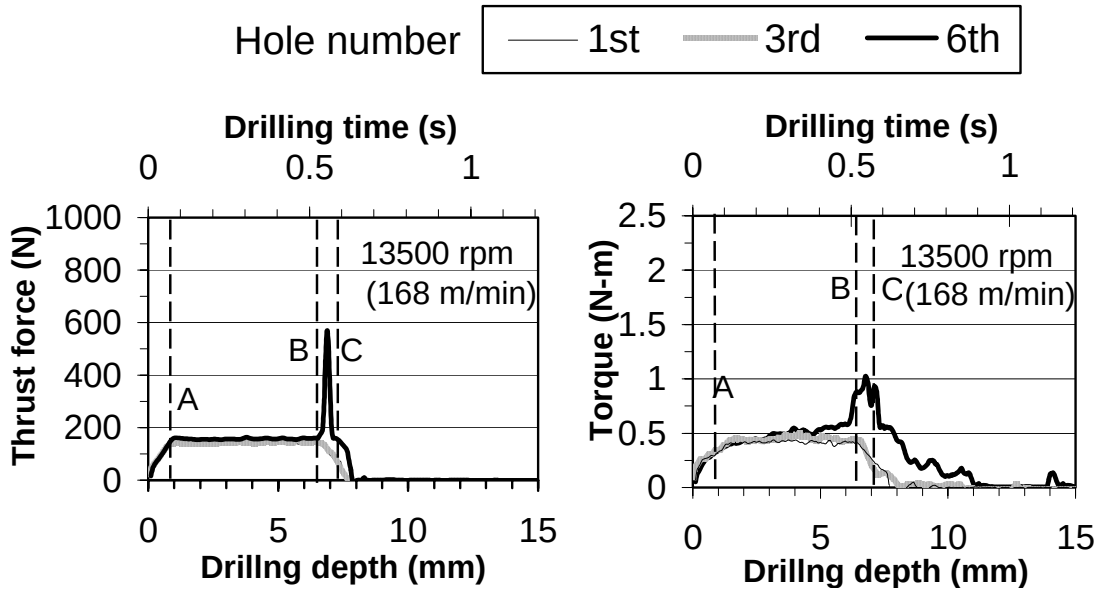

Fig. 2. Thrust force and torque of high speed drilling of Ti-6Al-4V at 13500 rpm (11.4 mm/s feed rate and 168 m/min peripheral speed) without cutting fluid.

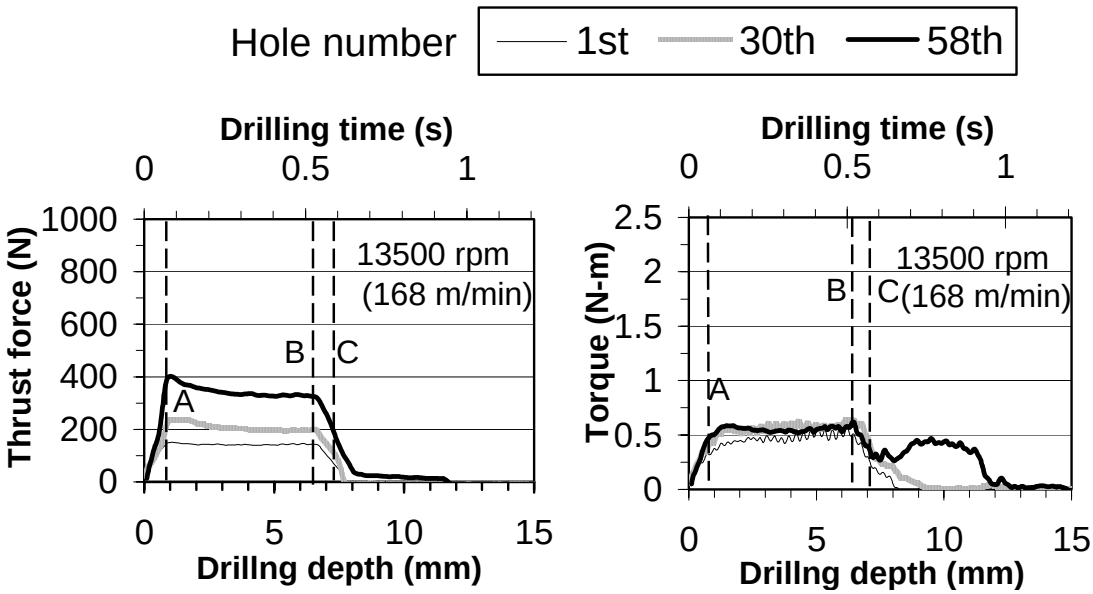

Fig. 3. Thrust force and torque of high speed drilling of Ti-6Al-4V at 13500 rpm (11.4 mm/s feed rate and 168 m/min peripheral speed) with the cutting fluid.

2. Turning test with TiC-Ni_3Al (9%) material

2.1. Tool material characteristics

As reported in the previous quarterly report, the TiC-Ni_3Al (5%) tool life was short, especially at the high cutting speed. One possible reason is the porosity of the material which results in the brittleness of the tool under high stress. One of the solutions is to increase the content of Ni_3Al binder, which reduces the material porosity, as shown in Fig. 4. Increase the binder volume sacrifices the hardness of TiC-Ni_3Al material, as shown in Table 2.

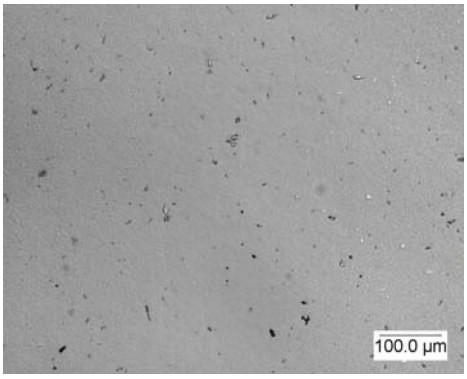

(a) TiC-Ni_3Al (5%)

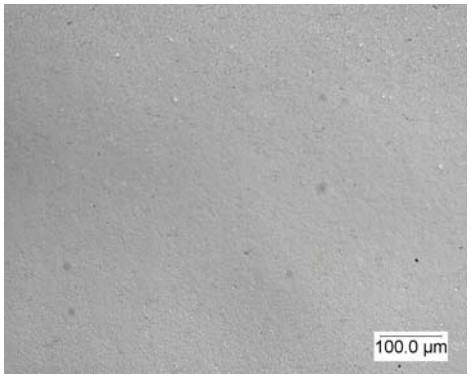

(b) TiC-Ni_3Al (9%)

Figure 4. Microstructures of TiC-Ni_3Al cermets.

Table 2. Micro-indentation hardness.

Material	HV (GPa, 200 g)
TiC-Ni_3Al (5%)	20.6
TiC-Ni_3Al (9%)	17.3
WC-Co (6%)	18.5

2.2. Turning test results

A tool insert made of TiC-Ni3Al (9%), developed by ORNL was tested in orthogonal turning of CP Ti bar with 38 mm in diameter. The tests were conducted at 48.8 and 195 m/min cutting speeds, 0.25 mm/rev feed, and 1 mm depth of cut. The cutting forces are summarized and compared with a WC-Co tool in Fig. 5. Consistently, the TiC-Ni_3Al tools showed higher cutting forces than the WC-Co tool. This was likely due to the imperfect tool geometry with low sharpness cutting edges of the TiC-Ni_3Al tools.

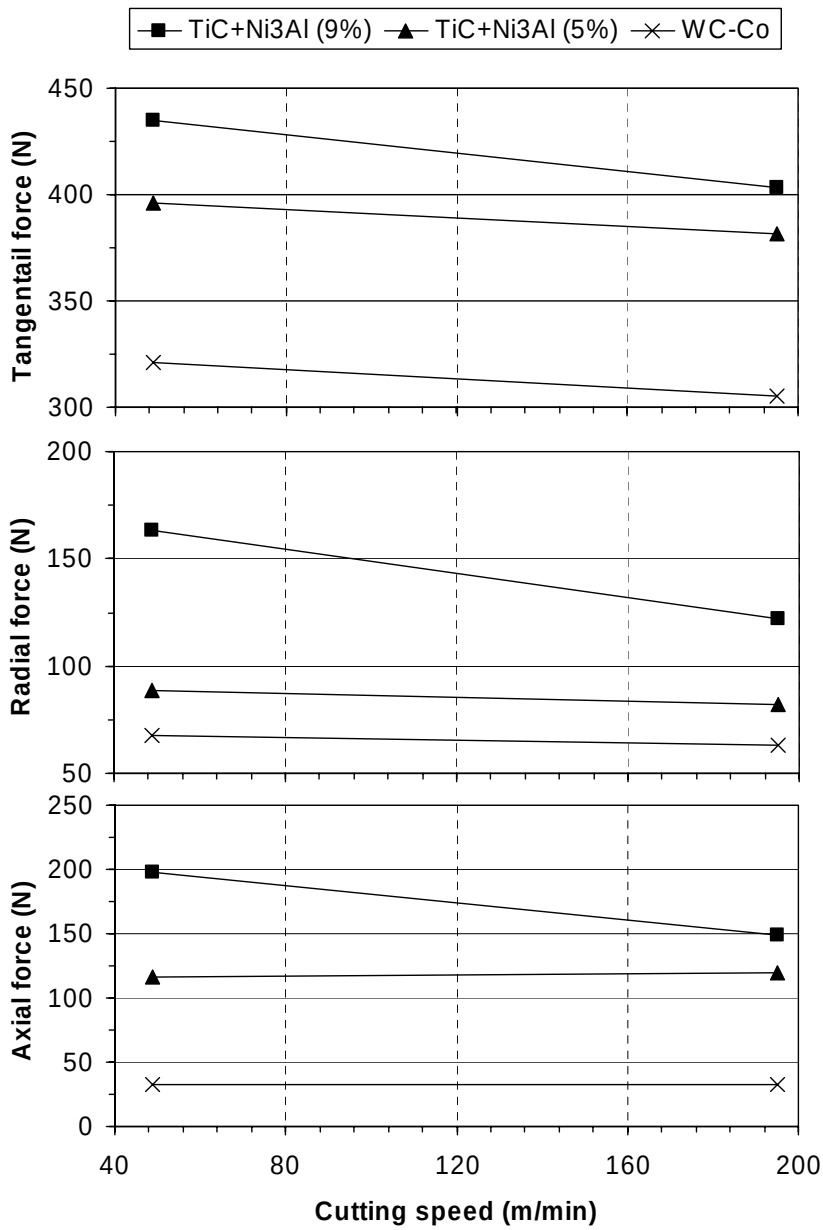

Fig. 5. Cutting forces of TiC-Ni_3Al and WC-Co tools in machining of Ti.

The tool life was also evaluated. The dominant failure mode of TiC-Ni_3Al tools is catastrophic tool breakage. Table 3 summarizes the tool life of the TiC-Ni_3Al tools compared with a WC-Co tool. Due to the high porosity as shown in Fig. 4(a), TiC-Ni_3Al(5%) tools broke at all cutting speeds. The TiC-Ni_3Al (9%) tools survived at 48.8 m/min with progressive wear after 294.4 seconds, but broke fairly quick at 195 m/min. Significantly different tool life, 9.2 and 33.7 seconds, at high cutting speed (195 m/min) were obtained on two tips of a single TiC-Ni_3Al (9%) tool insert, indicating the non-uniformity of the microstructure or the non-consistent condition of the cutting edges. The higher Ni_3Al content improves the performance of TiC-Ni_3Al tool material, but some efforts like better preparation of tool edge and surfaces are still needed in order to achieve or exceed the performance of WC-Co tool material. We have contact Kennametal, our tooling partner, and they are supportive to help us grind the ORNL new TiC tool material to the finishing shape.

Table 3. Tool life (s) in machining Ti.

	Cutting speed (m/min)		
	24.4	48.8	195
TiC-Ni_3Al (5%)	245.3	18.4	15.3
TiC-Ni_3Al (9%)	*Not tested*	>294.4	9.2/33.7
WC-Co	*Not tested*	*Not tested*	69

3. Inverse Heat Transfer Solution in Tool Temperature in Drilling of CP Ti

The high tool temperature in drilling low thermal conductivity Ti alloys is the obstacle in Ti machining. This research studies the tool temperature distribution in drilling of Ti.

The heat generation rate and drill temperature distribution during Ti drilling are difficult to measure directly. By using the idea to divide the drill cutting edges into segments called elementary cutting tool (ECT) [5], Ke [6] has developed the approach to extract the forces data acting on each ECT. At the start of drilling, one ECT after another in the drill chisel and cutting edges gradually engages into the cutting action from center of the drill. Using measured thrust force and torque at the start of drilling, cutting forces in each ECT can be calculated. The chip thickness and shear angle associated with each of the ECT can be measured from the machined chip to estimate the chip speed. Based on these cutting data, the frictional force and friction heat generation can be solved. A heat partition factor is required to find the amount of heat transfers to the tool for thermal finite element analysis. This heat partition between the drill and chip is recognized as one of the most difficult parameters to determine [7]. The inverse heat transfer method is developed in this study to overcome this problem.

Inverse heat transfer utilizes the temperature measured by thermocouples embedded on the drill flank surface as the input to predict the heat flux on the drill chisel and cutting edges. This method determines the heat partition factor using the optimization method. Thermocouples are routed from the frank surface, via through-the-drill coolant holes, to outside the tool [7]. During drilling, these thermocouples do not contact nor interfere with the chip. A validation process can be performed by comparing the drill temperature distribution results to thermocouple measurements not used for inverse heat transfer analysis.

3.1. Experimental setup

The experiment will be conducted in a Mori-Seiki TV-30 computer numerical control vertical machining center. Fig. 6 shows the experimental setup with the stationary drill and the Ti workpiece rotated by spindle. The drill was stationary because four thermocouples embedded on the flank face could be routed through coolant holes in the drill body to data acquisition system during the drilling process [7]. The workpiece was a 38 mm diameter CP Ti bar. The drill was a 9.92 mm diameter spiral point drill, Kennametal K285A03906. The spiral point drill had 135° point angle, 1.9 mm point length, and the S-shaped chisel edge. The tool material was the WC in 9.5 wt. % Co matrix (Kennametal grade K715) with 1.44×10^4 kg/m^3 density, 95 W/m-K thermal conductivity, and 203 J/kg-K heat capacity.

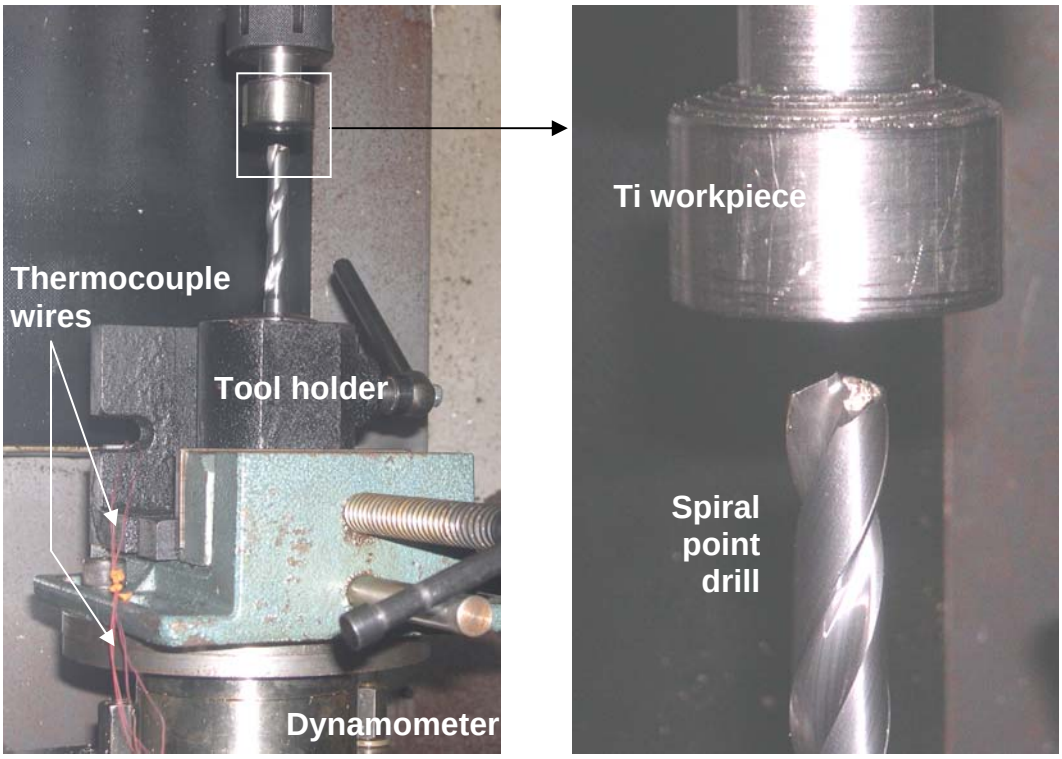

Fig. 6. Experimental setup with workpiece in the holder of spindle and drill in a vertical tool holder.

Fig. 7 shows the locations of four thermocouples on the drill frank surface. The top view of a new drill is shown in Fig. 7(a). The tip of 0.127 mm diameter type E thermocouples was installed at the edge of hand-ground slots on the drill flank face. Four thermocouples are denoted as TC1, TC2, TC3, and TC4 and arranged at different locations on the frank surface, as shown in Fig. 7(b). The XY coordinate of four thermocouples are listed in Fig. 7. The close-up view of TC1 and TC2 are illustrated in Fig. 7(c). TC1 is located close to the cutting edge away from the drill center and TC2 is placed close to the flute and away from the drill center. TC3 and TC4, as shown in Fig. 7(d), both near the cutting edge, are close to and away from the drill center, respectively. Three drilling experiments will be conducted at three spindle speeds, 780, 1570, and 2350 rpm, which correspond to 24.4, 48.8, and 73.2 m/min drill peripheral cutting

speed, respectively. The feed will remain fixed at 0.051 mm/rev. All the experiments will be conducted dry without cutting fluid.

3.2. Finite element mesh

Fig. 8 shows the finite element mesh of the drill, which is modeled by 68,757 four-node tetrahedral elements. As shown in the top view in Fig. 8(b), 13 nodes are located on the chisel edge and 11 nodes are placed on each cutting edge to achieve good resolution of the temperature distribution in the analysis of drill temperature distribution in Ti drilling.

This research is-ongoing, the optimization method is expected to calculate the heat partition coefficient. The finite element method can then calculate the temperature distribution in the drill. The temperature is expected to be high.

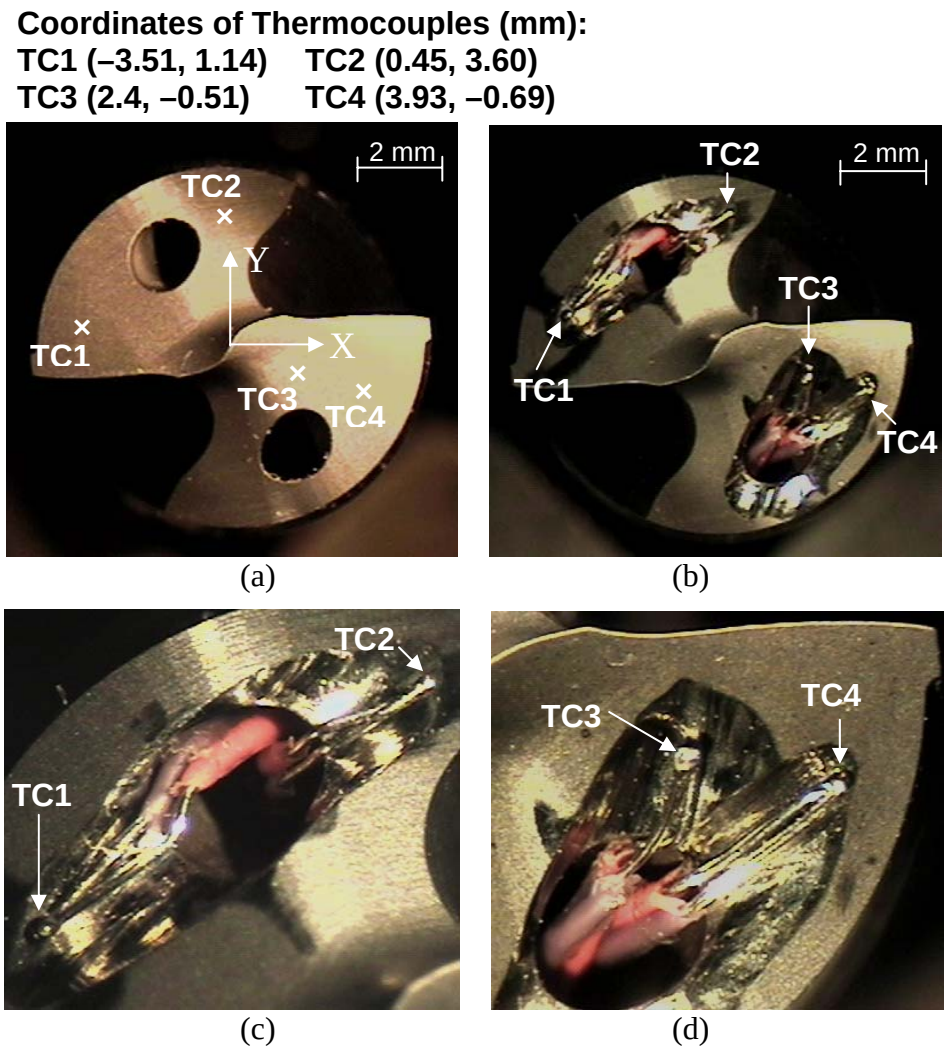

Fig. 7. Thermocouple in the drill flank face: (a) original drill, (b) drills with thermocouples embedded, (c) close-up view of TC1 and TC2, and (c) close-up view of TC3 and TC4.

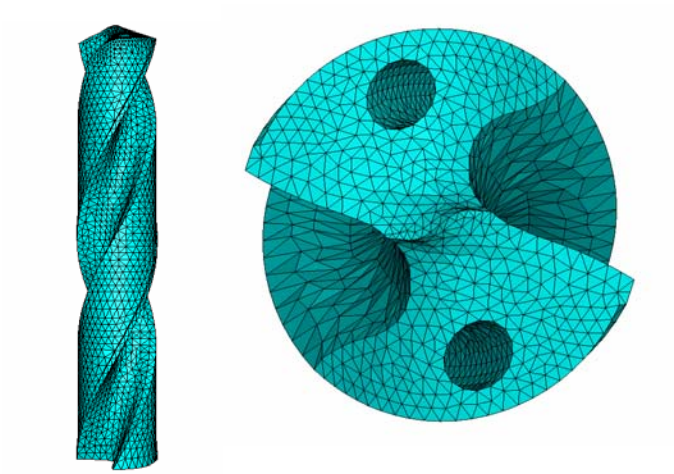

(a) (b)

Fig. 8. Mesh for the 3D finite element thermal model: (a) side view and (b) top view.

Future Work

The research will continue in high-speed drilling process development, inverse heat transfer analysis, and the exploration of new TiC-NiAl3 cutting tool material. On the thermal-mechanical coupled finite element modeling, Third Wave Systems is working on improving the drilling simulation efficiency and accuracy.

Status of Milestones

Milestone 1: Experimental study of Ti drilling.

Status: Extensive tests of Ti-6Al-4V drilling in dry and wet condition have been conducted and reported. New drilling tests are expected to start at ORNL using the Sabre machine.

Milestone 2: 3D finite element modeling of titanium drilling process.

Status: This work has current stall. We are waiting for a new version of ThirdWave Systems software on drilling.

Milestone 3: Investigation of TiC-based cutting tool material.

Status: Exploratory tests of Two TiC-Ni_3Al cermets with 5% and 9% matrix material have been conducted. Cutting forces have been measured and compared with the results when using WC-Co tool at different cutting speeds and feeds. The porosity of the material has been improved with higher Ni_3Al content, but the manufacturing technique and surface and cutting edge preparation of the tool inserts need to be improved in the future. We are working with Kennametal on this task.

Milestone 4: Measure of Ti drilling temperature.

Status: Experiments have been setup to measure the temperature in Ti machining. We are working to develop a thermal finite element model for inverse calculation of the drill temperature distribution based on the measurement results.

Communications/Visit/Travel

Albert Shih visit BorgWarner on April 15th and reviewed the Ti machining of turbocharger compressor wheels for International.

Albert Shih, Ray Johnson, Peter Blau, and Jun Qu visit BorgWarner on May 31st to review the Ti application in turbocharger and tour the BorgWarner Turbo facility at Asheville, NC.

Albert Shih visit ORNL on June 1st.

Publications

R. Li and A. J. Shih, "Finite Element Modeling of 3D Turning of Titanium," *International Journal of Advanced Manufacturing Technology* (accepted).

References

[1] A.R. Machado, J. Wallbank, 1990, "Machining of Titanium and Its Alloys-A Review," Proceedings of Institution of Mechanical Engineers, Part B: Management and Engineering Manufacture 204(1) 53-60.

[2] E.O. Ezugwu, Z.M. Wang, 1997, "Titanium alloys and their machinability-a review," Journal of Materials Processing Technology 68(3) 262-274.

[3] X. Yang, C.R. Liu, 1999, "Machining Titanium and Its Alloys," Machining Science and Technology 3(1) 107-139.

[4] M. Rahman, Y.S. Wong, A.R. Zareena, 2003, "Machinability of Titanium Alloys," JSME International Journal, Series C: Mechanical Systems, Machine Elements and Manufacturing 46(1) 107-115.

[5] A.R. Watson, 1985, "Drilling Model for Cutting Lip and Chisel Edge and Comparison of Experimental and Predicted Results I-Initial Cutting Lip Model," International Journal of Machine Tool Design and Research 25(4) 347-365.

[6] F. Ke, 2003, *Analysis and Modeling of Chip Ejection in Deep Hole Drilling Process*, PhD Dissertation, University of Michigan.

[7] J.S. Agapiou, D.A. Stephenson, 1994, "Analytical and Experimental Studies of Drill Temperatures," Journal of Engineering for Industry 116(1) 54-60.

Advanced Cast Austenitic Stainless Steels For High Temperature Components

P. J. Maziasz, John P. Shingledecker, and N. D. Evans
Oak Ridge National Laboratory

M. J. Pollard
Caterpillar, Inc.

Objective/Scope

This is the 2nd ORNL CRADA project with Caterpillar, which is focused on commercialization of the new CF8C-Plus cast austenitic stainless steel developed during the first ORNL/CAT CRADA. CF8C-Plus steel is a cost-effective performance upgrade relative to current heavy-duty diesel engine exhaust component materials, including SiMo ductile cast iron. In FY 2005, this project will complete the initial properties data base needed for component design or redesign, particularly fatigue, thermal fatigue, and creep, and studies of aged materials, including impact properties. This CRADA (Cooperative Research and Development Agreement) project (ORNL02-0658) began on July 21, 2002, and has been extended for two more years beyond the three-year expiration date of July 21, 2005. More detailed information on this project should be requested directly from Caterpillar, Inc.

Highlights

Caterpillar, Inc.

Stainless steel diesel turbocharger housings have been ordered for a low volume off-road application.

Sectioning of the large CF8C-Plus turbine housing is complete. Mechanical testing will commence next quarter.

ORNL

Initial tensile and impact testing on new commercial heats of CF8C-Plus Cu/W was completed this quarter.

ORNL testing and comparison of CF8C-Plus and Diado KN2 austenitic stainless steels for replacement of SiMo cast iron for diesel engine turbocharger housings continued this quarter.

Technical Progress, 3rd Quarter, FY2005

Background

Current cast iron heavy diesel engine exhaust manifolds and turbocharger housings are being pushed beyond their temperature capabilities as normal duty cycles go to 750°C or higher; rapid and severe thermal cycling contributes to increased failures. New materials with upgraded temperature capability and reliability for such applications must also be commercially available at a reasonable cost. The new cast CF8C-Plus austenitic stainless steel now being commercialized holds promise of being such a material. Current efforts by Caterpillar, Inc. and ORNL include completing the systematic and thorough properties data base required by designers to optimize component design, and characterizing the properties of trial or prototype commercial components.

Approach

Multiple commercial heats of CF8C-Plus have been cast by several commercial foundries, including static sand and centrifugal casting methods. Now, both large and small prototype CF8C-Plus components are also being cast. In July 2004, a large turbine housing for an industrial gas-turbine was cast by MetalTek International, Inc. from an 8000-lb heat of the new CF8C-Plus stainless steel. One goal of this project is provide characterization support for such component prototyping efforts. In FY 2004, new heats of standard CF8C-Plus (Mn+N) and a new modified CF8C-Plus steel (Mn+N+Cu+W) were also produced by MetalTek International to compare large cross-section thicknesses for centrifugally castings, and static castings with higher cooling rates, and these are currently being tested and characterized at ORNL.

Technical Progress – Caterpillar, Inc.

Sectioning of the large industrial gas-turbine housing, shown in Figure 1, is complete. Initial observations have found no obvious cases of hot tearing at the side flange where previous trials with standard CF-8C have shown indications. This is significant because fully austenitic alloys like CF8C-Plus are usually more susceptible to hot tearing, than similar steel with a much higher δ-ferrite content (standard CF8C steel has 15-25%). Further NDT analysis will be performed to ensure a complete absence of hot tears.

Fatigue test samples of the bulk material from this housing have been produced, and mechanical testing will commence this month. This will hopefully show that the properties do not change significantly in thick section components compared to smaller test castings.

Stainless steel diesel-engine turbocharger housings have been ordered for a small quantity off-road diesel engine application. Due to current supplier agreements, these are being cast to a different alloy, KN2. However, these can be compared directly to CF8C-Plus steel, and this prototyping effort should give the designers at Caterpillar confidence with cast stainless steel as well as some experience with the necessary design changes for cast stainless.

Technical Progress - ORNL

Last year, a new commercial heat of modified CF8C-Plus steel with further additions of Cu and W, was made by MetalTek, which were found to further boost the YS even more at 600-850°C. Tensile data and preliminary fatigue data are complete. Aging continued at ORNL this quarter on these steels, and creep, fatigue, thermal fatigue will be done next quarter.

Analysis of creep rupture data continued at ORNL this quarter. Clearly, the CF8C-Plus steel has 1.5-2 times more creep-rupture strength than the standard CF8C steel, as shown in Figure 2. There is a far greater creep strength advantage for CF8C-Plus relative to either SiMo ductile or Ni-resist austenitic cast irons. Analysis of the creep-rupture ductility of CF8C-Plus and CF8C steels is shown in Fig. 3, for testing at 650-850°C. Despite the substantial creep-strength advantage of CF8C-Plus compared to CF8C steel, it also has significantly more rupture ductility, mainly due to its stable austenite matrix phase that is free of as-cast δ-ferrite, which rapidly transforms to embrittling σ-phase during aging or creep.

Figure 1. 6600-lb gas turbine combustor housing centrifugally cast from CF8C-Plus stainless steel by MetalTek International, Inc. No indications of hot tearing have been observed (Mike Pollard is pictured with the casting).

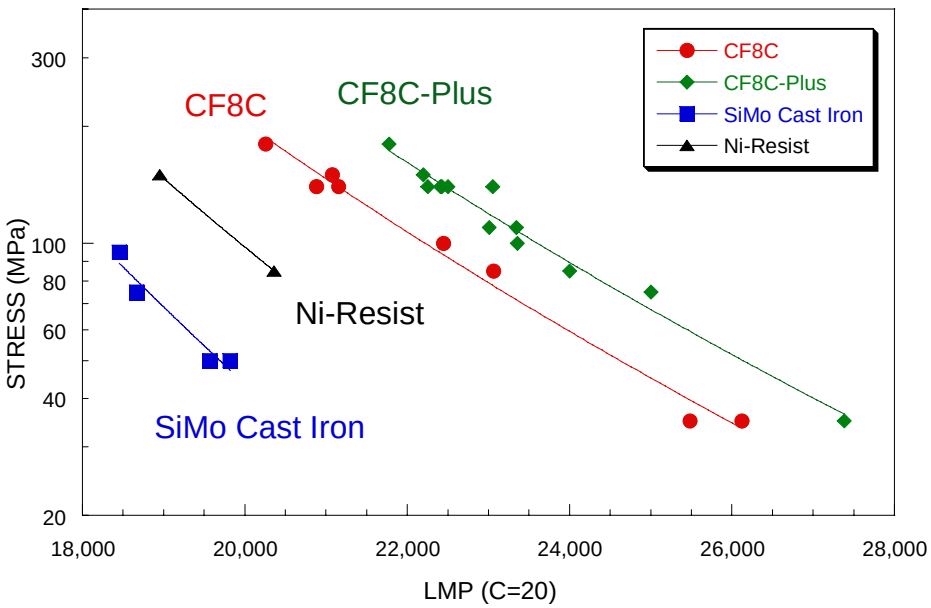

Figure 2 – Creep-rupture stress plotted versus Larson-Miller Parameter (LMP) for various creep-rupture tests run at 500-850°C at ORNL in air of various commercial heats of SiMo ductile and Ni-resist austenitic cast irons, and standard CF8C and new CF8C-Plus austenitic stainless steels. CF8C-Plus shows a significant creep-strength advantage over the standard steel or the cast irons.

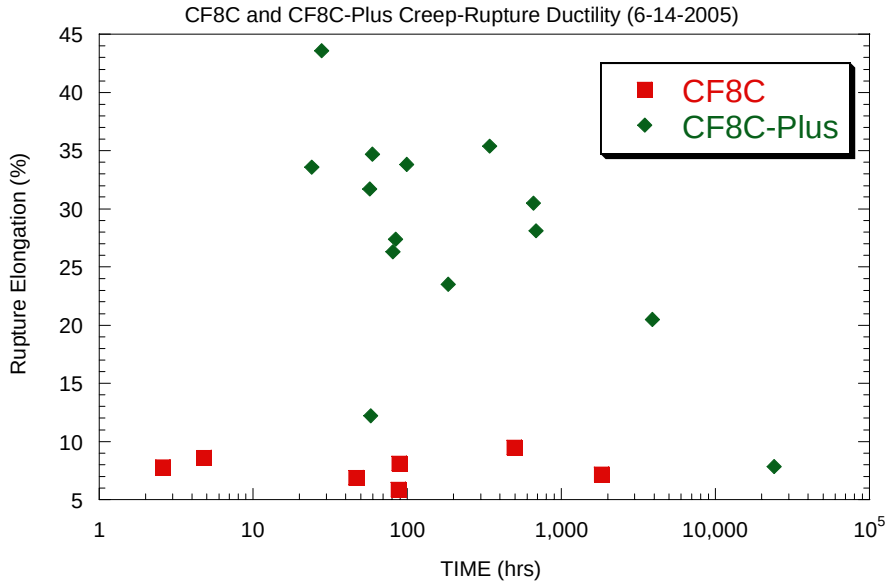

Figure 3 – Comparison of creep rupture ductility data versus rupture time for new cast CF8C-Plus steel and standard CF8C steel (same data as shown in Fig. 2), for creep-rupture testing in air at 650-850°C, and 35-200 MPa.

Finally, early in FY 2005 ORNL began testing and characterization on the Diado KN2 cast austenitic stainless steel (Fe-19Cr-12Ni-0.7Nb-0.3C, Si,S steel) and comparison to CF8C-Plus, in support of alternate turbocharger housing studies by their supplier. Comparison of as-cast, and cast + aged room-temperature tensile properties are given in Table 1. While the KN2 steel is stronger in the as-cast condition, both stainless steels have similar properties after aging, with the CF8C-Plus being slightly stronger with more ductile fracture (reduction in area). However, high temperature properties comparisons will continue next quarter, which better determines the application-relevant properties.

Table 1 – Room Temperature Tensile Properties of Cast or Cast + Aged Austenitic Stainless Steels

Alloy	Aging	YS (ksi)	UTS (ksi)	Elongation (%)	Reduction of Area (%)
CF8C-Plus	none	38.2	88.6	39.1	31.2
	750°C/3000 h	49.0	89.4	14.5	15.7
KN2	none	48.4	89.4	15.7	13.2
	750°C/1000 h	44.0	87.6	14	9.1

Communications/Visits/Travel

Detailed team communications between ORNL and Caterpillar occur regularly, at least once or twice a week. The new three-year CRADA began on July 21, 2002, when the previous CRADA ended and is scheduled to end on July 21, 2005. The two-year ORNL/Caterpillar CRADA extension was finished this quarter.

Status of Milestones (ORNL for DOE)

FY 2005 Milestones for Subtask 4.10 – 1) Complete properties measurements of new CF8C-Plus heats, including static and centrifugally cast, at 700-850°C (2/05); **complete**, 2) Commercially scale up new CF8C-Plus heats with Cu/W alloying additions for more high-temperature strength, and complete initial testing (6/05); **complete**, and 3) Extend the current CRADA for another year or more to complete testing and evaluation of prototype components cast from CF8C-Plus (7/05); **complete**.

Publications/Presentations/Awards

This quarter, CF8C-Plus steel was awarded new ORNL Technology Transfer and Economic Development (TTED) Royalty Funds to enable further aged impact, and high-temperature creep and creep-fatigue of the new commercial heats with Cu and W added.

M. J. Pollard, P. J. Maziasz and J. P. Shingledecker, "Development of Low Cost Cast Austenitic Stainless Steel for Diesel Engine and Gas Turbine Components," DOE Project Review at Advanced Materials Technology, Caterpillar, Peoria, IL, April 27,2005

P. J. Maziasz, J. P. Shingledecker, N. D. Evans, ORNL and M. J. Pollard, Caterpillar, "Development, Application and Properties of CF8C-Plus" presentation given at visit to Stainless Foundry and Engineering, Inc., Milwaukee, WI, June 16, 2005.

P. J. Maziasz, J. P. Shingledecker, N. D. Evans, ORNL and M. J. Pollard, Caterpillar, "Development, Application and Properties of CF8C-Plus" presentation given at visit to MetalTek International Inc., Waukesha, WI, June 27, 2005.

Interface Instability of a Ti_3al/Tial Nanocomposite

Luke L. Hsiung
Lawrence Livermore National Laboratory

Objective/Scope

The stability of interfaces in a TiAl-(γ)/Ti_3Al-(α_2) lamellar nanocomposites has been investigated. The objective of this study is to understand the role of lamellar interfaces on creep mechanisms of Ti_3Al/TiAl nanocomposites. Three major deformation activities have been observed as a result of the interface instability of the nanocomposite; they are interface sliding, interface migration, and interface-initiated deformation twinning.

Technical Highlights

It has been reported previously that the mobility of interfacial dislocations can play a crucial role in the creep deformation behavior of TiAl-(γ)/Ti_3Al-(α_2) lamellar nanocomposites (or nanolaminate composites). Since the operation of lattice dislocations within ultrafine γ and α_2 lamellae is largely restricted, interfacial dislocations become the major strain carriers for plasticity. As shown in Fig. 1 (a), a nearly linear creep behavior [i.e. ε (steady-state creep rate) = $k\sigma^n$, where σ is applied creep stress and $n \approx 1$] was observed in low-stress (*LS*) regime, and power-law break down ($n > 5$) was observed in high-stress (*HS*) regime. Results of TEM investigation as shown in Figs. 1 (b) and 1 (c) have indirectly revealed the occurrence of interface sliding in low-stress (*LS*) creep regime and deformation twinning in high-stress (*HS*) creep regime. These results have led us to propose that interface sliding in association with a viscous glide of pre-existing interfacial dislocations is the predominant creep mechanism in *LS* regime, and interface-initiated deformation twinning in γ lamellae is the predominant creep mechanism in *HS* regime. Stress concentration resulting from the movement and pileup of interfacial dislocations has been suggested to be the cause for the interface-initiated deformation twinning.

Accordingly, the creep resistance of Ti_3Al/TiAl nanocomposite is considered to depend greatly on the cooperative movement of interfacial dislocations, which in turn may be controlled and hindered by the interfacial segregation of solute atoms (such as W) or interfacial precipitation. Furthermore, through the in-situ TEM observation, we have also reported that the lamellar interfaces can migrate directly through the cooperative motion of interfacial dislocations. That is, the γ/γ and γ/α_2 interfaces can migrate through interface sliding and lead to the coalescence or shrinkage of constituent lamellae (i.e. microstructural instability), which results in a weakening effect when ultrafine lamellar TiAl is employed for engineering applications. More results and detailed analyses on interface instability including interface sliding and interface-initiated deformation twinning are reported here.

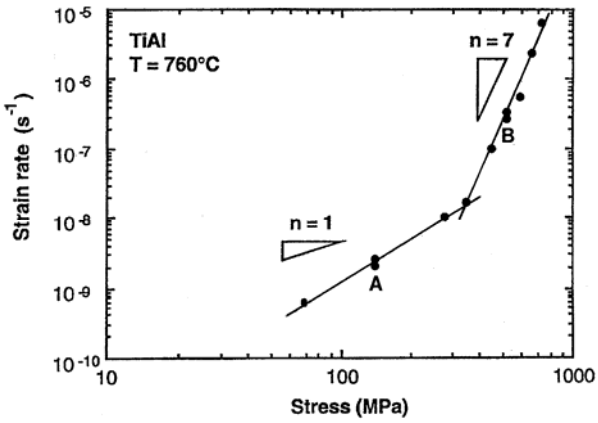

(a)

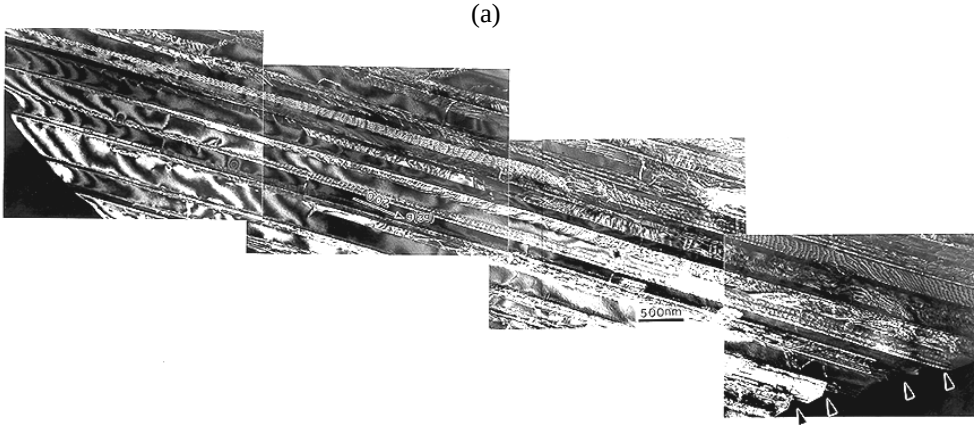

(b)

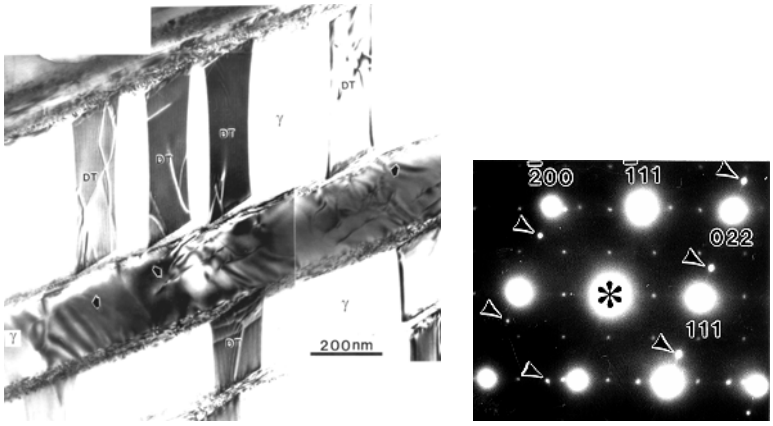

(c)

Fig. 1. (a) Steady-state creep rate plotted as a function of applied stress at 760 $^{\circ}$C for Ti-47Al-2Cr-2Nb lamellar nanocomposite showing that there existed two distinct creep regimes, i.e. low stress (*LS*) and high stress (*HS*) regimes; (b) a TEM image showing grain boundary ledges (marked by arrows) presumably formed as a result of interface sliding within a specimen creep-deformed at 138 MPa [condition A in (b)]; (c) a bright-field TEM image showing the formation of ($\bar{1}$ 11) type deformation twins (*DT*) within a specimen creep-deformed at 518MPa [condition B in (b)].

Interface sliding

In principle, the multiplication and motion of interface dislocations and lattice dislocations are major deformation mechanisms to carry deformation strain in a $Ti_3Al/TiAl$ laminate composite. Since the volume fraction of α_2 lamella is small (≤ 10%), deformation by the motion of lattice dislocations mainly occurs within the γ lamellae. Also, the free dislocations can only accommodate small strain because of their short moving distance before impinging interfaces. Thus, the motion (bowing) of threading dislocations contributes primarily to deformation strain within the γ lamellae. In general, the critical resolved shear stress ($\tau_b \approx \mu b/d$) required to bow the threading dislocations is dependent upon the thickness (d) of γ lamellae. Taking μ = 59 GPa (at 760 $^\circ$C), b = 0.28 nm, and d = 100 ~ 250 nm, the critical resolved shear stress is calculated to be τ_b = 66 ~ 165 MPa. The applied stress ($\sigma \approx 2\tau_b$) required to bow the threading dislocations is, therefore, greater than 132 ~ 330 MPa. The bowing of threading lattice dislocations is more likely to occur in a thicker γ lamella when crept in the *LS* regime. A typical observation of the bowing lattice dislocations within a γ lamella (~350 nm thick) is shown in Fig. 3. Also notice that impinged dislocation lines are left behind on a lamellar interface along the wake of the bowing lattice dislocations.

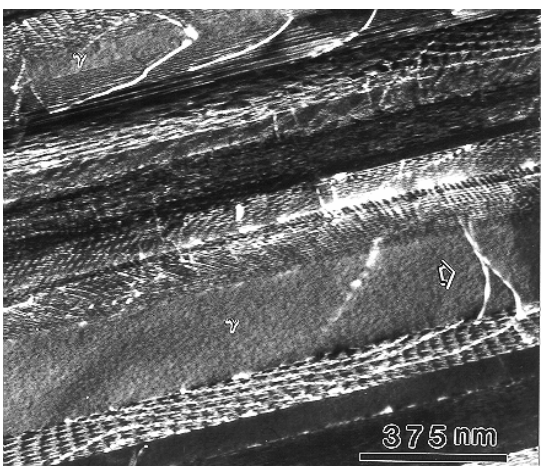

Fig. 3. WBDF image showing the bowing of lattice dislocations (marked by an arrow) within a γ lamella of a sample crept at 138 MPa.

Since the motion and multiplication of lattice dislocations within both γ and α_2 lamellae are limited in the *LS* regime as a result of the ultrafine lamellae, the motion of interfacial dislocations is anticipated to be the major source for plastic deformation. It is worth noting that the cooperative motion of interfacial dislocations resulted from an *in situ* straining experiment has been reported previously. Other evidence of the motion of interfacial dislocations is presented below. Figure 4 (left) shows the interfacial substructure of a lamellar grain in a sample crept at 138 MPa. The appearance of fringe contrasts trailing along interfacial dislocations can be readily observed. The fringe contrasts were best viewed when $2\pi \boldsymbol{g} \bullet \boldsymbol{R}$ = 2/3 or 4/3, where $\boldsymbol{g}$ is the reflection vector and $\boldsymbol{R}$ (= 1/3[111]) is the displacement vector of stacking fault in γ lamella, which suggests the formation of stacking faults on the wake of interfacial dislocations. Here, the triangular features are presumably formed by the motion of three sets of interfacial dislocation arrays with Burgers vectors: $1/6[\bar{1}\,\bar{1}\,2]$, $1/6[1\,\bar{2}\,1]$ and $1/6[\bar{2}\,1\,1]$. The formation mechanism is schematically illustrated in Fig. 4 (right), where the equilibrium γ/α_2 interface resulting from both interfacial dislocation motion (pure shear) and chemical diffusion is lagging behind the non-equilibrium interface created solely by the motion of interfacial dislocations. Here, a stacking fault forms as the first Shockley partial, $1/6[\bar{1}\,\bar{1}\,2]$, glides along the interface, but is terminated by the glide of

the second Shockley partial, 1/6[$1\bar{2}1$]. Then, another stacking fault forms as the third Shockley partial, *1/6*[$\bar{2}11$], glides along. The highly populated interfacial dislocations and stacking faults on lamellar interfaces are expected to be preferential sites for solute (impurity) segregation. These solutes subsequently act as short-range barriers for the motion of interfacial dislocations, in a manner similar to that of *Cottrell* atmosphere and *Suzuki* effect. Consequently, the viscous glide of interfacial dislocations is resulted and causes the linear creep behavior of the material in the low stress regime.

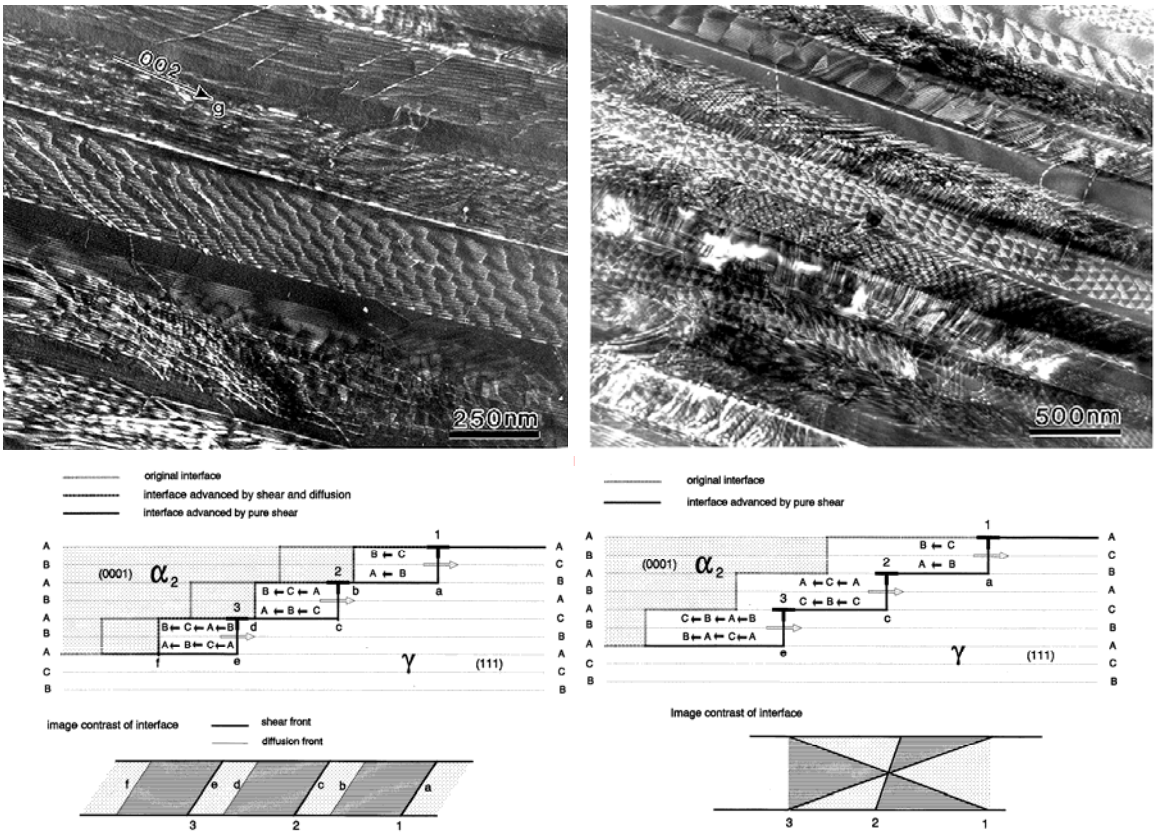

(a) (b)

Fig. 4 (Above) A WBDF image showing the appearance of fringe contrast trailing along *ID* on lamellar interfaces, A schematic illustration of the migration of γ/α_2 interface resulted from the cooperative glide of *ID* arrays and chemical diffusion. The fringe contrasts due to the formation of stacking fault ribbons on the wake of *ID* illustrated as (a) single *ID* array and (b) multiple *ID* arrays (with three different 1/6<$11\bar{2}$> Burgers vectors). The letters A, B and C stand for the stacking sequence.

Interface-initiated deformation twinning

When a nanocomposite sample is creep-deformed at 760 °C with a constant applied stress of 518 MPa under a strain rate of 3 x 10^{-7} s^{-1}, a deformation substructure associated with deformation twins is developed within γ lamellae. Typical $(\bar{1}11)$ [211]-type twin lamellae formed within γ lamellae are shown in Fig. 5. Notice that one (labeled by an arrow) of the twin lamellae in Fig. 5 (a) is still growing toward another interface. This suggests that the lamellar interface is the major source for the occurrence of deformation twinning. This twinning phenomenon can be viewed as a relaxation process to relieve the local stress concentration caused by the pile-up of interfacial dislocations. The effective stress (τ_e) at the head of the pile-up of n dislocations can be evaluated by $\tau_e = n\tau_i$ [12], where τ_i is the resolved shear stress acting on the interface. To relieve the stress concentration, deformation twinning in γ layers is therefore taking place by a dislocation reaction based upon a stair-rod cross-slip mechanism as schematically illustrated in Fig. 5 (b). For the formation of a $(\bar{1}11)$-type twin lamella, the corresponding dislocation reaction is $1/6[\bar{1}2\bar{1}]_{(111)}$ [**b1**] → $1/6[011]_{(100)}$ [**b2**] + $1/6[\bar{1}1\bar{2}]_{(\bar{1}11)}$ [**b3**]. The $(\bar{1}11)$-type twin is accordingly formed within γ lamella by successively dissociating the [**b1**] interfacial dislocations in the pile-up and emitting the [**b3**] twinning dislocations into the $(\bar{1}11)_\gamma$ plane and leaving the [**b2**] stair-rod dislocations in the $(100)_\gamma$ plane. Figures 5 (c) and 5 (d) show edge-on views of the $(\bar{1}11)$-type twin lamellae, in which their widths were measured to be varied between 3 nm and 20 nm.

The formation of [**b2**] stair-rod dislocations at the intersections between twin and α_2 lamellae is evidenced in Figs. 6(a) and 6(b), in which the array of *1/6*[011] stair-rod dislocations becomes invisible [Fig. 6(a)] or visible [Fig. 6(b)] when a reflection vector (***g***) 200 or 021 is used for imaging. It is noted that the individual stair-rod dislocation is not resolvable because of a narrow distance (0.25 nm) between two stair-rod dislocations. The formation of [**b3**] twinning dislocations for the $(11\bar{1})$-type twin lamella is evidenced in Figs. 6(c) and 6(d), in which the array of *1/6*[112] twinning dislocations becomes visible [Fig. 6(c)] or invisible [Fig. 6(d)] when a reflection vector 111 or $\bar{2}02$ is used for imaging. The significance of the proposed mechanism is to reveal that there are several barriers to be overcome in order to activate the twinning reaction. These barriers include (1) the repulsive force between the interfacial (Shockley) and stair-rod dislocations, (2) the increase of line energy due to the dislocation dissociation, and (3) the increase of interfacial energy due to the formation of twin faults. Among which the repulsive force (F) between the interfacial (Shockley) and stair-rod dislocations is considered to be the rate-limiting process. That is, a critical stress (τ_c) is required to activate for the twinning reaction, i.e. to activate the dissociation reaction for twinning. Assuming an isotropic elasticity, the critical stress (τ_c) can be approximately evaluated as: $\tau_c b_1 = F \approx \eta\mu b_1 b_2 \cos\theta/2\pi r$, where, $\eta = 1$ for screw dislocations and $\eta = 1/(1-\upsilon)$ for edge dislocations, and υ is Poisson's ratio (~0.3); μ is shear modulus (~56 GPa at 760°C), b_1 = 0.163 nm, and b_2 = 0.094 nm for Shockley and stair-rod dislocations, respectively; θ (= 54.4°) is the angle between $(\bar{1}11)$ and (100) planes, and *r* (0.25 nm) is the distance between the two dislocations. The critical stress (τ_c) required for twinning is thus approximately 1.95 GPa for screw dislocations and 2.79 GPa for edge dislocations.

In the case of a low applied stress (138 MPa), the resolved shear stress (τ_i) acting on the interface plane is about 69 MPa (assuming Schmid factor = 0.5), the number of pile-up dislocations required to create a sufficient stress concentration (i.e. $\tau_e = n\tau_i \geq \tau_c$) for twinning to occur is $n \geq 29$. In the case of a high applied stress (518 MPa), the resolved shear stress acting on the same interface plane is about 259 MPa, and the number of pile-up dislocations required for twinning to occur is $n \geq 8$. Thus, the accumulation creep strain required to onset the viscoplastic twinning is smaller and therefore easier to reach. Besides,

the average velocity of dislocations is relatively faster when tested under a high applied stress since the strain rate is higher, which gives a shorter time to develop a pile-up configuration when tested under high applied stresses. That is, the viscoplastic twinning is more feasible to take place when the nanocomposite is creep-deformed under high applied stresses.

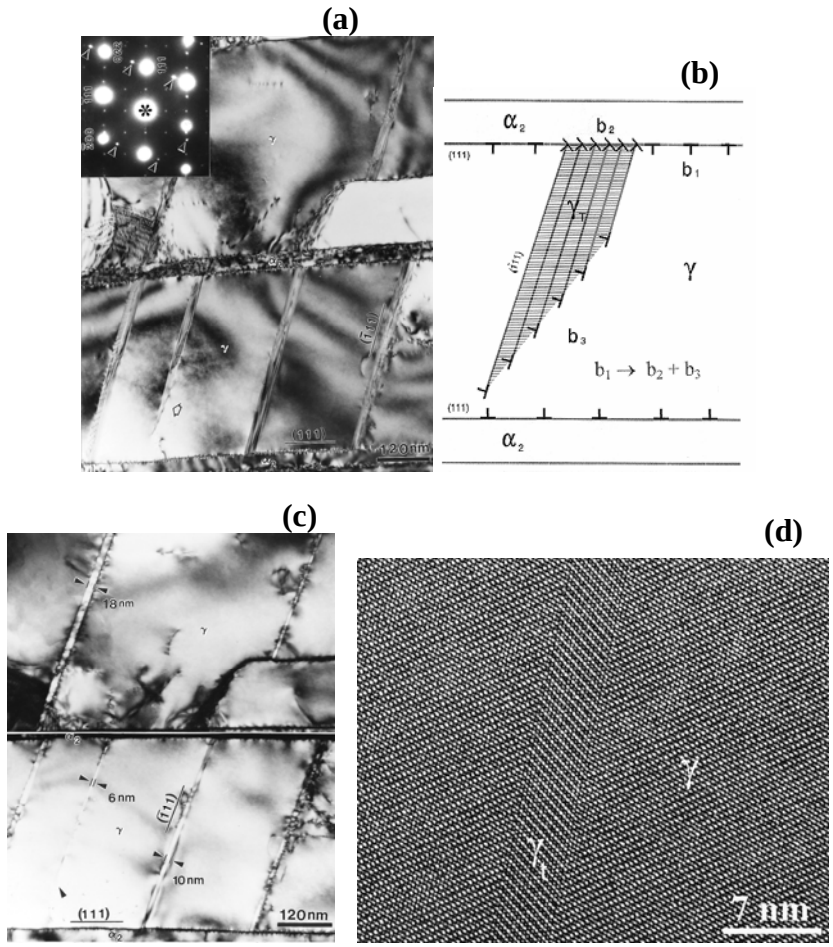

Fig. 5. (a) A dark-field TEM image shows several ($\bar{1}11$) type twin lamellae formed within a γ lamella; (b) Schematic illustration of the nucleation of a ($\bar{1}11$) type twin lamella (γ_t) from a γ/α_2 interface, where $\mathbf{b_1}$, $\mathbf{b_2}$, and $\mathbf{b_3}$ denote the interfacial, stair-rod, and twinning dislocations, respectively; (c) and (d) Edge-on views of twin lamellae show the widths of the ($\bar{1}11$)-type twin lamellae.

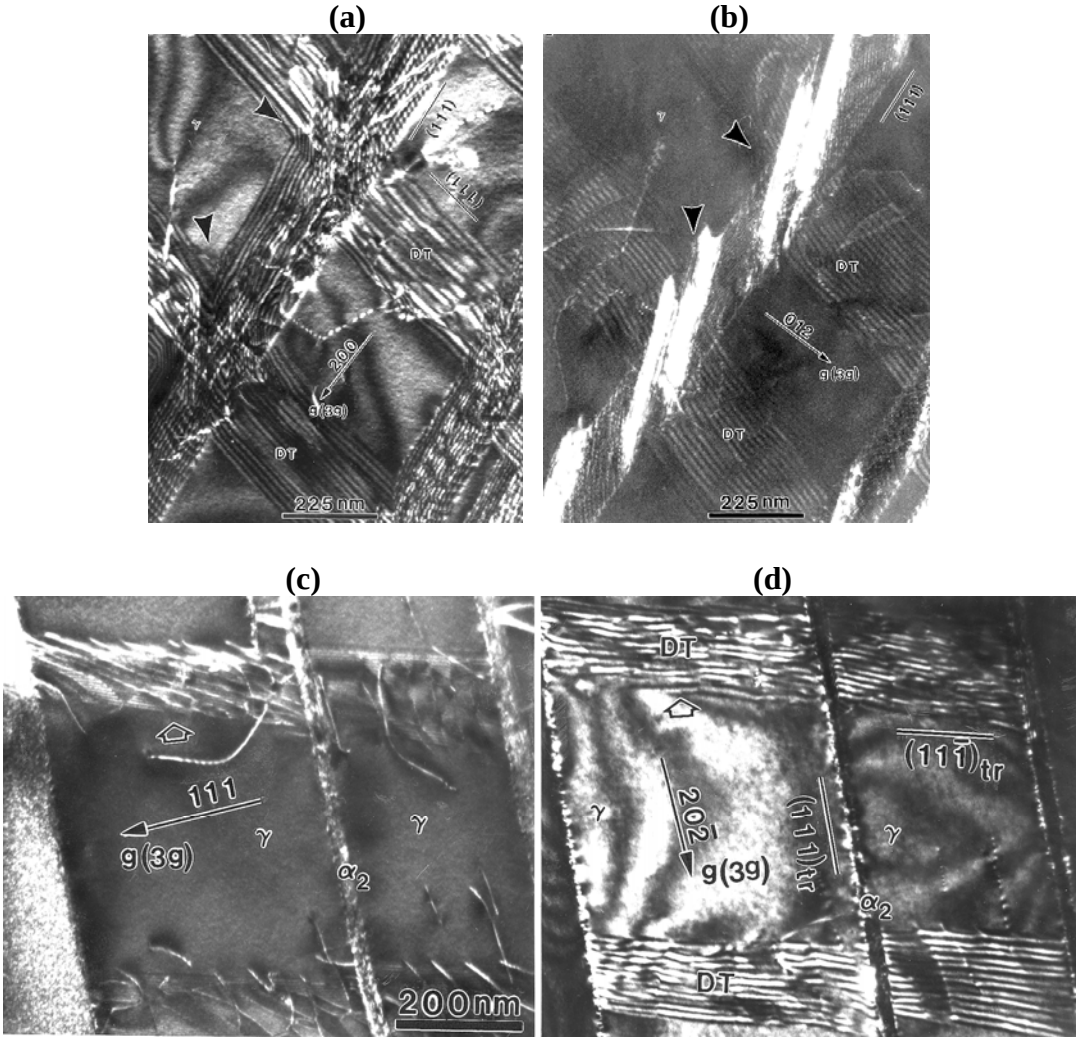

Fig. 6. WBDF TEM images show the ***g•b*** contrast visibility analyses [13] for the arrays of [**b2]** *1/6*[011] stair-rod dislocations formed at the intersections (indicated by arrows) between the ($\bar{1}11$)-type deformation twins (DT) and α_2 lamellae: (a) **Z** (zone axis) ≈ [$0\bar{1}2$], ***g*** *= 200,* ***g•b*** *= 0* (invisible), (b) **Z** ≈ [$0\bar{1}2$], ***g*** *= 021,* ***g•b*** *=1/2* (visible); and the analyses for the arrays of [**b3]** *1/6*[112] twinning dislocations of the ($11\bar{1}$)-type deformation twins: (c) **Z** ≈ [$\bar{1}2\bar{1}$], ***g*** = 111, ***g•b*** = 2/3, (visible), and (d) **Z** ≈ [$\bar{1}2\bar{1}$], ***g*** = $20\bar{2}$, ***g•b*** = 1/3 (invisible).

<u>Status of FY 2005 Milestone</u>

Investigation of the impact damage of Ti_3Al/TiAl nanocomposite using two stage light-gas gun is currently underway.

High Density Infrared Surface Treatment of Materials for Heavy-Duty Vehicles

T. N. Tiegs, D. C. Harper, F. C. Montgomery, and C. A. Blue
Oak Ridge National Laboratory

Objective/Scope

High Density Infrared (HDI) technology is relatively new to the materials processing area and is gradually being exploited in materials processing. For many applications in heavy-duty vehicles, superior properties, such as corrosion and wear resistance, are only required at the material surface. The project using HDI technology will be exploratory and will examine the application of wear-resistant coatings based on hard-metal type compositions.

Technical Highlights

Earlier work had shown that adherent coatings of hardmetal compositions could be applied to a variety of metal substrates (D-2 tool steel, 4140 alloy steel, and cast iron). As reported previously, samples were fabricated that used ceramic particles only (e.g. WC or TiC) for the coating with no binder addition. The idea was that the sintering temperature for these plain carbides is significantly higher than the melting point of the substrates. Consequently, because no binder additions (i.e. Ni or Ni_3Al) are present, sintering and cracking would be inhibited, which was a problem with earlier samples. Finally, this would allow the coating to heat up to a sufficiently high temperature so that the underlying substrate would melt and be wicked into the coating by capillary action.

Samples were fabricated with varying coating thickness (50 and 100 µm) and particle type (WC, TiC, W, or WC/W). The samples were IR treated at numerous exposure conditions. Cracking of the coatings was observed in a similar behavior to previous tests where the binder was included. A preheat step helped to minimize the cracking. However, getting the coatings hot enough to melt the underlying substrate was extremely sensitive. The conditions to go from little bonding to where extensive melting of the entire sample occurred was very narrow. Control of the coating process without the incorporation of binder particles in the coating is very difficult. Additional samples are being planned where binders are again used in the coatings.

Status of Milestones

On schedule.

Communications/Visits/Travel

None.

Problems Encountered

None.

Publications

None.

High Temperature Aluminum Alloys

Yong-Ching Chen
Cummins Inc.

Objective/Scope

Work at Cummins has identified three potential paths to improve the high temperature strength and fatigue resistance of aluminum casting alloys. These paths have been partially investigated under cooperative agreement DE-FC05-97OR22582. Each path showed some promise and further work is needed to determine the useful applications.

Task 1. Ternary Phase Diagrams

This task involves a ternary phase aluminum alloy utilizing rare earth metals to provide precipitate size control and stability. Limited information on these alloys indicates high temperature strength and stability, however, the predicted cost of the alloy is high. Additional work shall be performed to determine if additional rare earth (or other metal) elements which produce beneficial properties at a reasonable cost. Cummins shall develop ternary phase compositions by means of modeling of the equilibrium phase diagram, castings and evaluating the properties of alloys identified.

Task 2. NASA-Developed Process

This task involves a conventional aluminum alloy, which has been chemically modified by a process developed at NASA-Huntsville. The elevated temperature properties reported by NASA are attractive, but it is preferred for Cummins to use alloy with lower silicon content. Eck Industries purchased the license for the NASA-developed technology on high silicon casting alloy and has expanded the range to include conventional low silicon casting alloys. Limited testing of these modified conventional low silicon alloys at Cummins has not shown the property improvement anticipated. Physical and mechanical property measurements shall be performed on specimens provided by NASA and by Eck to characterize the material and determine the optimal properties possible by this method.

Task 3. Particulate-Reinforced Alloy

This task involves a particulate loaded aluminum alloy patented by Chesapeake Composites Inc. The nano-phase particulate at 50 volume percent provides adequate high-temperature strength in early experiments, however, the particulate loaded alloy could only be forged or squeeze cast so complex shape capability is limited. Cummins shall fully characterize the specimens previously made to determine the mechanical behavior of the alloy. Casting modifications shall also be investigated to determine shape capability for the alloy.

Task 4. Reporting Requirements

Quarterly reports and final reports

Task 5. Quality Assurance Requirements

Technical Highlights

Task 3. Particulate-Reinforced Alloy

Task Summary -
This task involves a nano-phase particulate loaded aluminum alloy patented by Chesapeake Composites Inc. A patented, low cost, liquid metal infiltration process is utilized to produce a billet form ready for secondary operations. This composite material combines the enhanced elevated temperature strength, toughness, and ductility of dispersion strengthened (DS) alloys with the stiffness and low CTE of metal matrix composites (MMCs). It was claimed that this composite can be readily turned using WC tooling and drilled and tapped using high-speed steel tools. Potential applications include pistons, compressor wheel, and engine components.

Initial tensile and fatigue tests of 1090 Al and 2024 Al alloy reinforced with nanoscale Al_2O_3 particles (DSC) at elevated temperatures showed impressive results. Almost 100% improvement in tensile strength and yield strength was obtained on the DSC material as compared to those of the current production materials. No degradation in the tensile strength and fatigue strength was observed in the DSC material after 500 hours of thermal soaking at 400ºC.

A potential increase in pressure ratio from turbochargers has been requested by diesel engine manufacturers. To increase pressure ratio means to increase operation temperature of compressor wheels (impellers). Current aluminum alloys used for impellers are being used at their critical temperatures and little chance to further increase their operating temperatures. Titanium alloys are the current solution for higher temperature application, but they extremely expensive for this application. The proposed nano-particle dispersion strengthened aluminum matrix composites show a promise to meet the requirements.

In order to further verify that the DSC material exhibit adequate mechanical strength to meet the operation requirements, mechanical and physical properties of DSC materials will be measured. Chesapeake Composites Corporations and PCC-AFT manufactured billets of DSC material with 1.7 in. diameter and 7.0 in. long. The DSC billets contain 40 volume percent of Al_2O_3 nano-particles were infiltrated with 1090 aluminum alloy. Figure 1 shows one of the as-infiltrated DSC billets. Samples were taken from the billets for testing.

Figure 1. As-infiltrated DSC billets for material property testing

(1). Physical Properties Measurements

Samples of a DSC material were machined for thermophysical property testing from room temperature to 400°C. Thermal diffusivity (α) was measured using the laser flash technique. Bulk density (d) values were calculated from sample geometry and mass. Specific heat (C_p) values were obtained using a differential scanning calorimeter and thermal conductivity (λ) values were calculated as a product of the above quantities, i.e. $\lambda = \alpha C_p d$. Thermal expansion was measured using a dual push-rod dilatometer.

The density of the DSC material was measured to be 2.991 g/cm^3, which is about 12% heavier than that of the A354-T6 alloy (2.677 g/cm^3). The higher density needs to be taken into consideration during design since the compressor wheels made of DSC material will have higher reciprocal weight compared to those made of traditional aluminum alloy such as A354 alloy.

Figure 2 displays the thermal conductivity of the DSC material as a function of temperature. It is noted that the thermal conductivity of the DSC material decreases as the temperature increases. This is most likely due to the presence of high percentage of Al_2O_3 particles inside the aluminum matrix. The thermal conductivity of the DSC material was found to be much lower than that of either 354-T6 alloy or 355-T6 alloy. The lower thermal conductivity in the DSC material may result in higher operating temperature.

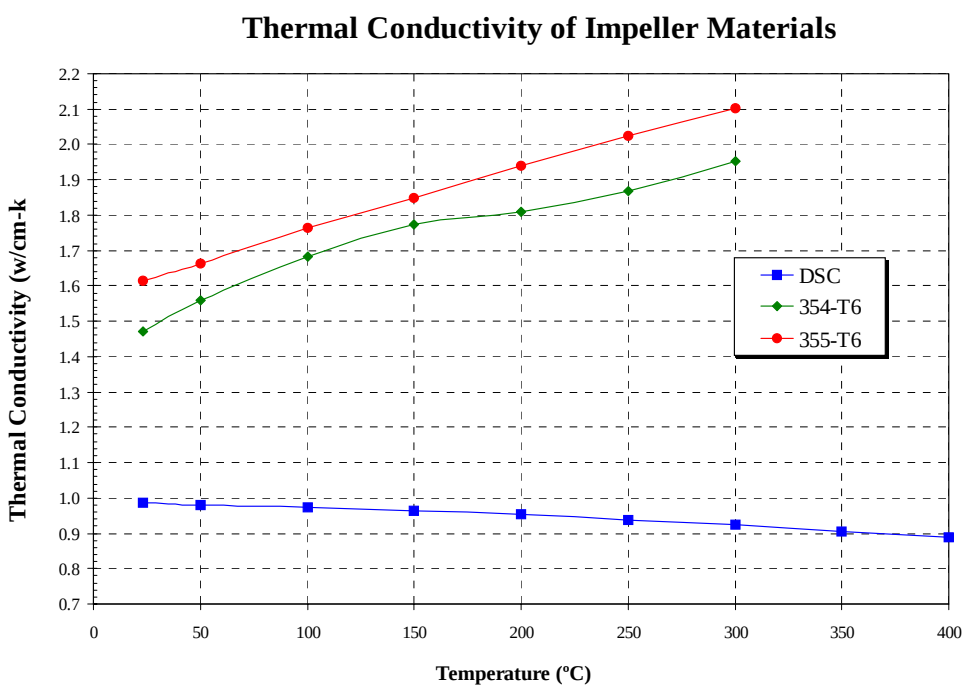

Figure 2. Thermal conductivity of the DSC material, 354-T6, and 355-T6 aluminum alloys.

The mean thermal expansion coefficient of the DSC material increases as the temperature increases, Figure 3. The mean CTE of the other two aluminum alloy, 354-T6 and 355-T6 alloy, are compared in Figure 3. It is noted that the mean CTE of DSC material was significantly lower than either 354-T6 alloy or 355-T6 alloy. The lower mean CTE was also most likely due to the presence of high percentage of Al_2O_3 particles inside the aluminum matrix of the DSC material. The lower CTE in the DSC material compared to 354-T6 or 355-T6 alloy may indicate smaller dimensional changes during operation.

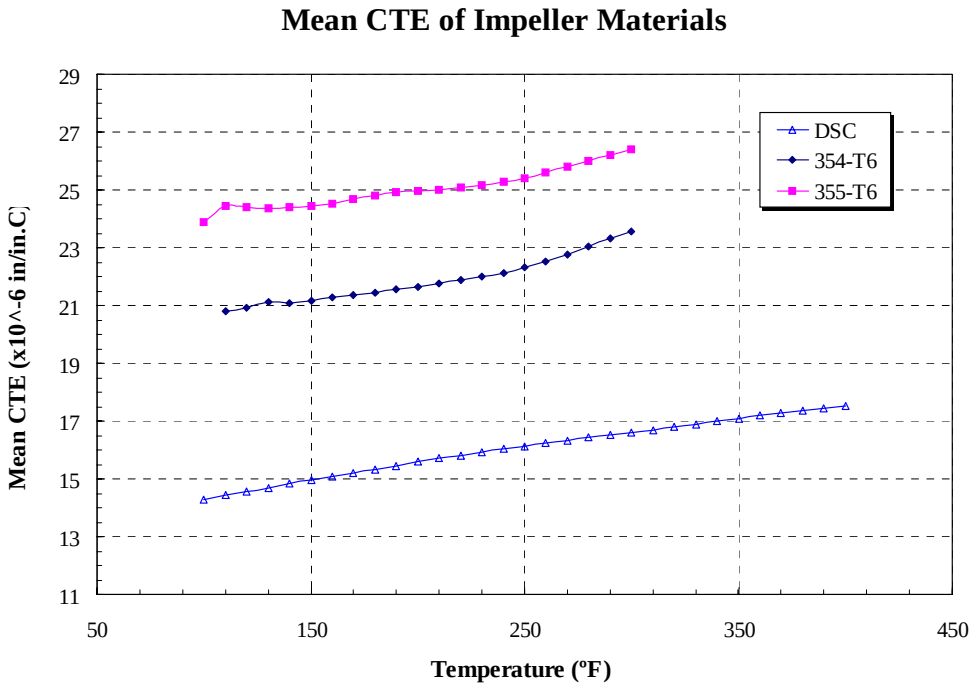

Figure 3. Mean coefficient of thermal expansion (CTE) of the DSC material, 354-T6, and 355-T6 aluminum alloys.

(2). Tensile Tests

Tensile samples with dimensions of 4.2 mm-diameter x 18 mm-gage length were prepared from the DSC billet for tensile testing at room temperature, 200ºC, 300ºC, and 400ºC without supplemental thermal soaking. Figure 4 shows the tensile strength of the DSC material as a function of temperature. The tensile strength of the DSC material tested in 2002 was also plotted for comparison. It is noted that the tensile strength of the DSC sample produced lately were much lower than that tested in 2002. The percent elongation and reduction of area at room were almost zero. Some samples broke quickly before yielding such that no yield strength was available. The much lower tensile strength of the DSC samples manufactured in 2005 was unexpected. Further microstructural examination was conducted to understand possible causes for the low tensile strength.

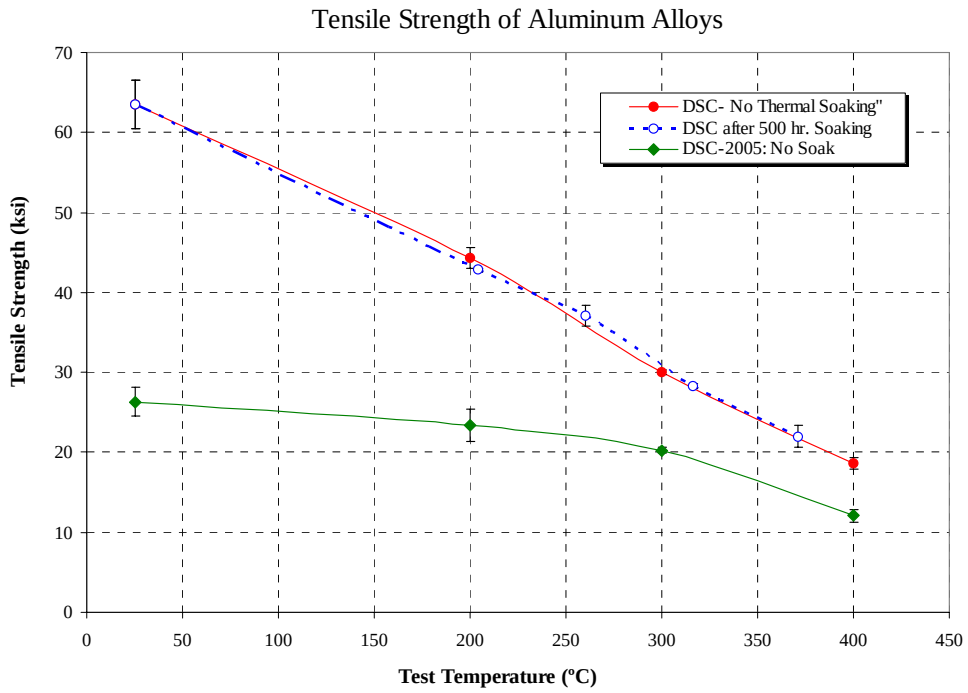

Figure 4. Elevated temperature tensile strength of the DSC material manufactured in 2005 and DSC material manufactured in 2002.

(3). Microstructure Examination

One of the DSC billets manufactured in early 2005 was sectioned in seven locations for macrostructure analysis (Figure 5-a). Seven samples were then polished using an automatic polishing system. Macro-photographs were taken of each sample to determine any defects present in the cross-sections. Figure 5-(b) shows two representative cross-sectional views in locations #3 and #4. Overall, no macro defect was observed in all cross-sections, except in cross-section #7, where some clusters of aluminum veins were observed. Microstructure at location #1 is shown in Figure 6 at 100X and 500X, respectively. Some aluminum veins were observed throughout the matrix.

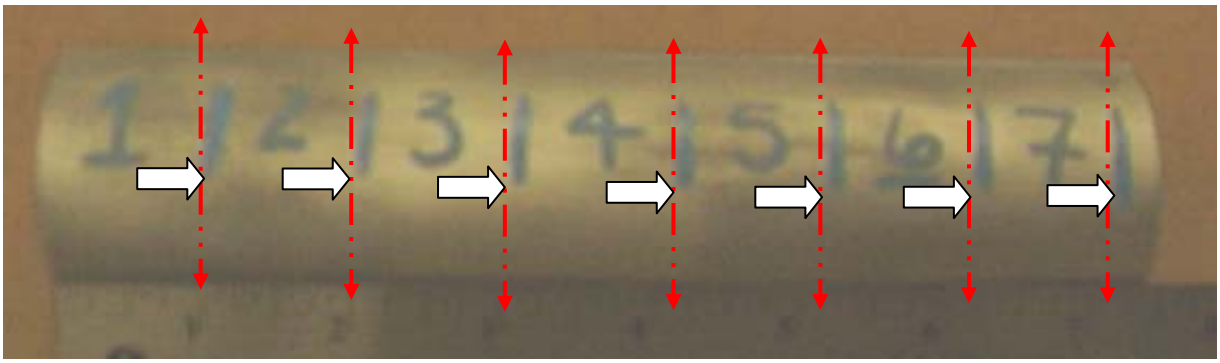

Figure 5-(a). Photograph of alumina composite billet prior to sectioning for macro examination. The locations of the cuts are one inch apart and represented by the red lines. The white arrows signify the side of the sample that was polished for further examination.

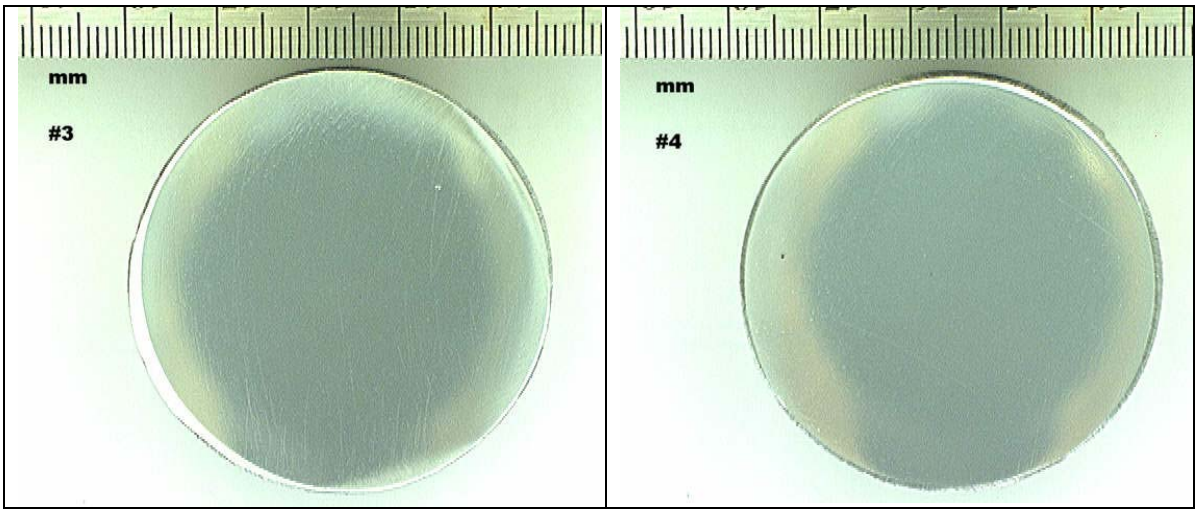

Figure 5-(b). Cross-sectional views of locations #3 and #4 showed no macro defects.

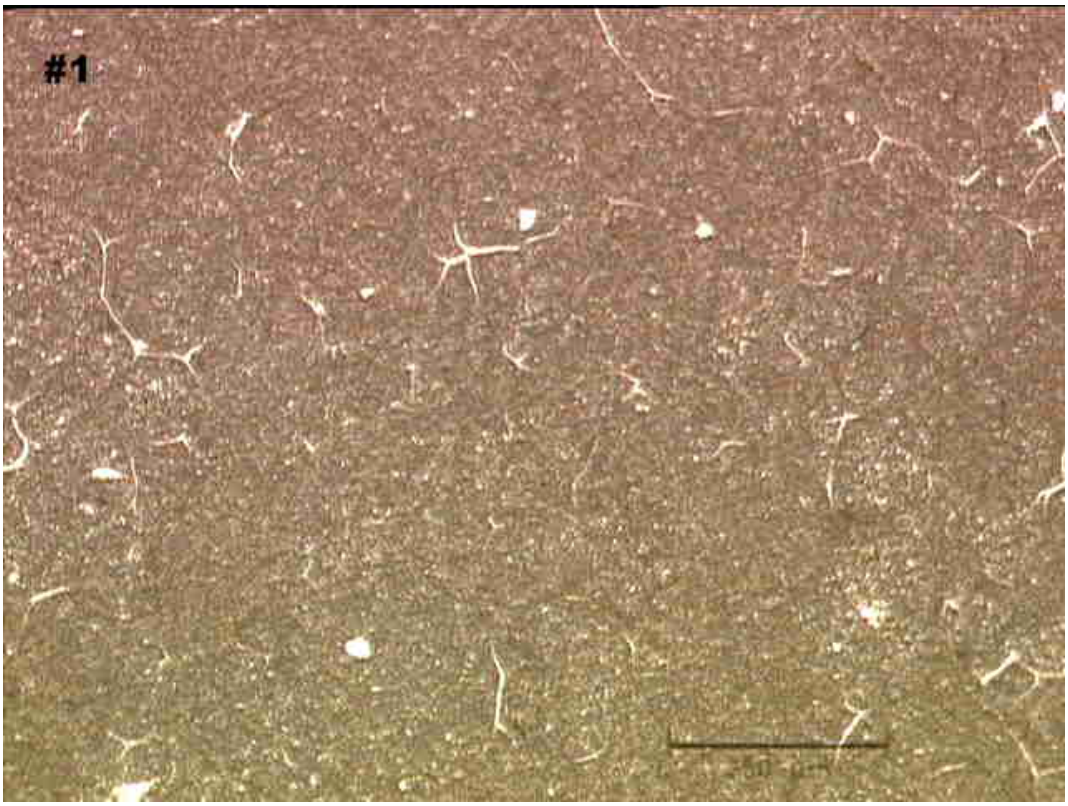

Figure 6-(a). Metallographic sample at location #1 taken at 100X.

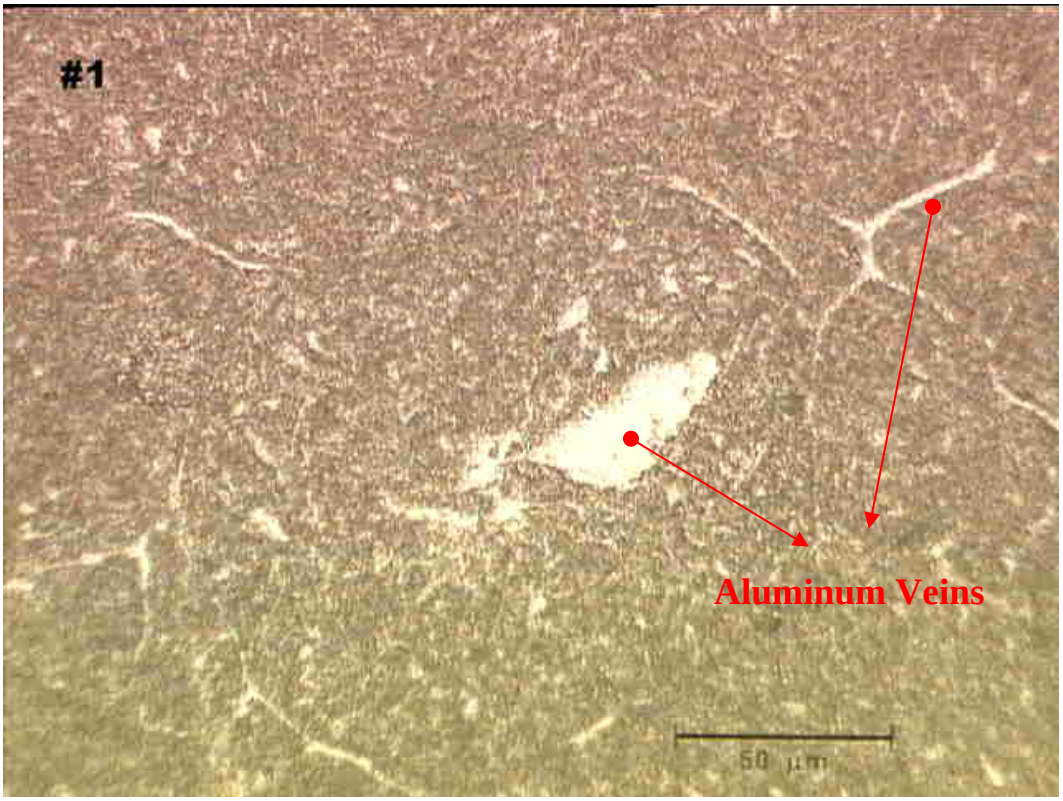

Figure 6-(b). Metallographic sample at location #1 taken at 500X.

In cross-section #4, a large defect with a dimension of about 250 microns was observed (Figure 7-a). The defect was further analyzed by using energy dispersive spectrometer (EDS) equipped with a scanning electron microscope (SEM). Figure 7-(b) displays the elemental dot maps of some key elements. The EDS analysis showed the presence of Si, Ca, K, Zr, Al, O and Fe in the defect. According to the supplier, the make-up of the defect was most likely zirconium silicate. Potassium (K) could be a defect found in the zircon, which was used as a spray dryer. The defects appeared to be contamination from the dry spray process that was used to make fine alumina powder.

The presence of aluminum veins together with defects resulted in lower strength of the current batch of DSC billets as compared to the billets provided in 2002.

In order to compare the microstructure of the current billets and that of the billets exhibited much higher tensile strength shown in Figure 4, five tested tensile bars prepared from the DSC billets manufactured by Chesapeake Composites in 2002 were submitted for microstructure analysis to determine if defects were present in the material. The tensile bar samples were tested previously at varied temperatures and after a 500-hour soak. Figure 7 shows the comparison between the tensile sample tested in 2002 and the billet samples manufactured in 2005. It is noted that the tensile sample tested in 2002 exhibited less cellular structure and much finer grain size as compared to the billet sample manufactured in 2005. Very little or no aluminum veins were observed in the tensile sample tested in 2002. The difference in the microstructure had resulted in significant difference in the tensile strength of the DSC billets.

According to the supplier, a different manufacturing process was used in making fine aluminum powders needed for making performs. The different in the quality of the powders had resulted in the dramatic difference in the final tensile strength. The quality of the current DSC billets was considered unsatisfactory and further process development is needed by the supplier to get material close to past strength and quality.

Overall Summary:

1. Physical property measurements of the DSC material were completed. The DSC material exhibited a density of 2.991 g/cm^3, which is about 12% heavier than that of the A354-T6 alloy.
2. The thermal conductivity of the DSC material was found to be much lower than that of either 354-T6 alloy or 355-T6 alloy. The lower thermal conductivity in the DSC material may result in higher operating temperature.
3. The mean CTE of DSC material was significantly lower than either 354-T6 alloy or 355-T6 alloy. The lower CTE of the DSC material may indicate smaller dimensional changes during operation.
4. The tensile strength of the DSC sample produced in 2005 was much lower than that of the billets tested in 2002. The inferior strength of the current DSC billets was most likely due to the presence of aluminum veins and defects inside the aluminum matrix.
5. The quality of the current DSC billets is not satisfactory. Further process improvement is needed by the supplier.

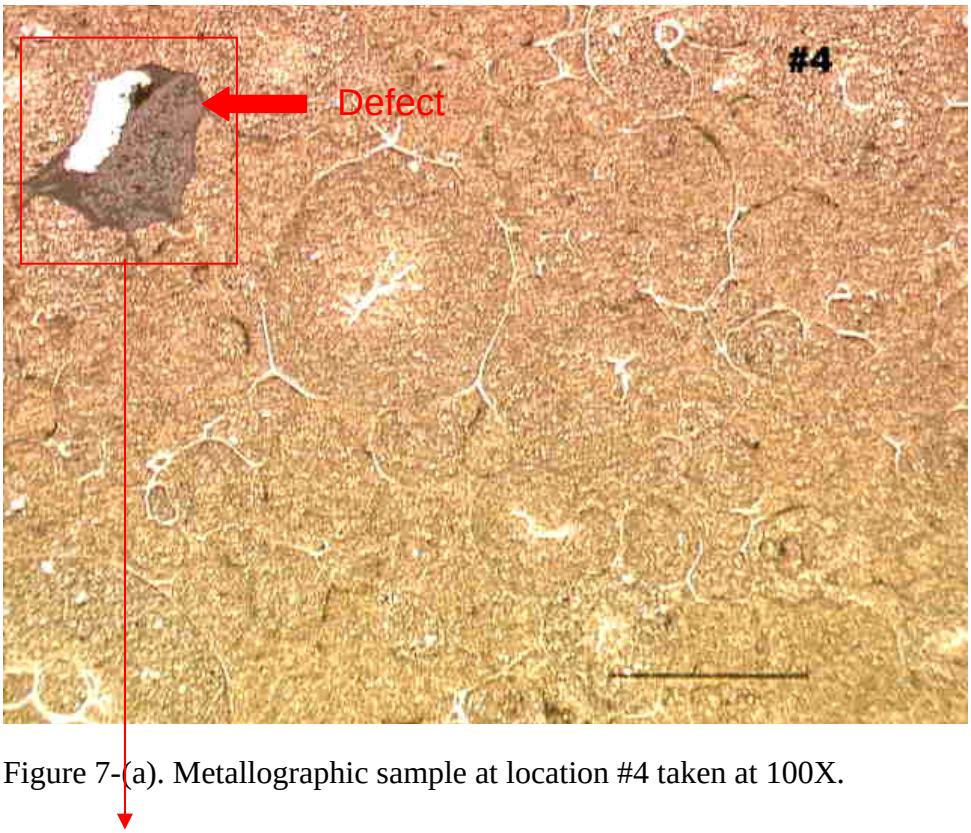

Figure 7-(a). Metallographic sample at location #4 taken at 100X.

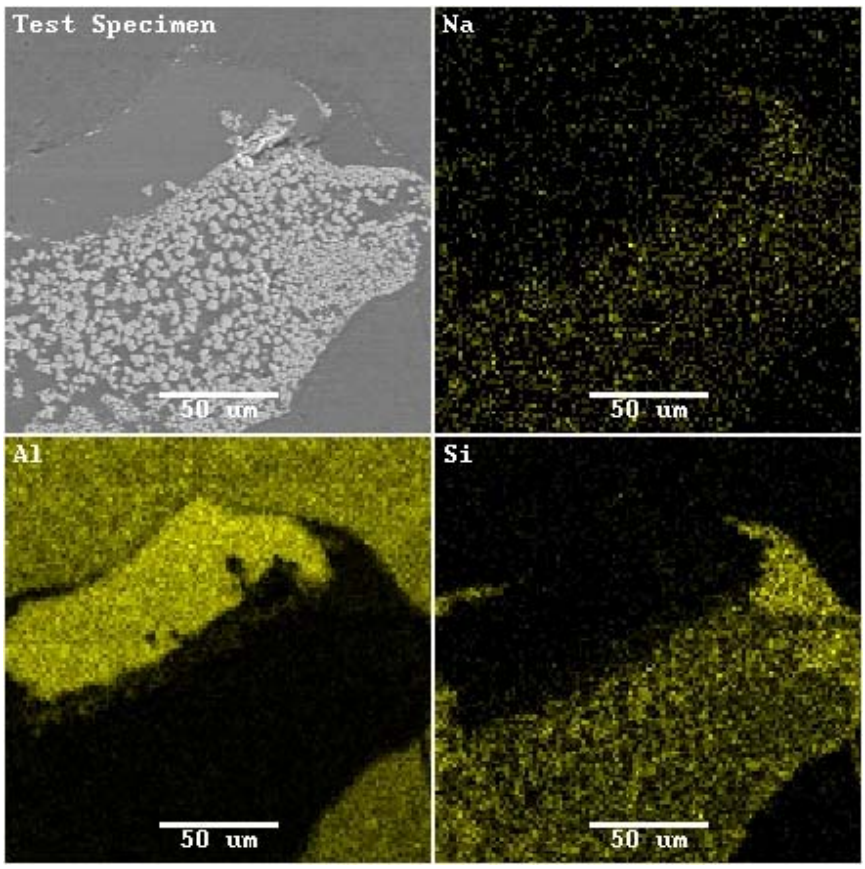

Figure 7-(b). EDS photographs for the defect in Sample #4. The yellow in the photographs represents the element present in the defect. Al, Si, and Na are represented above.

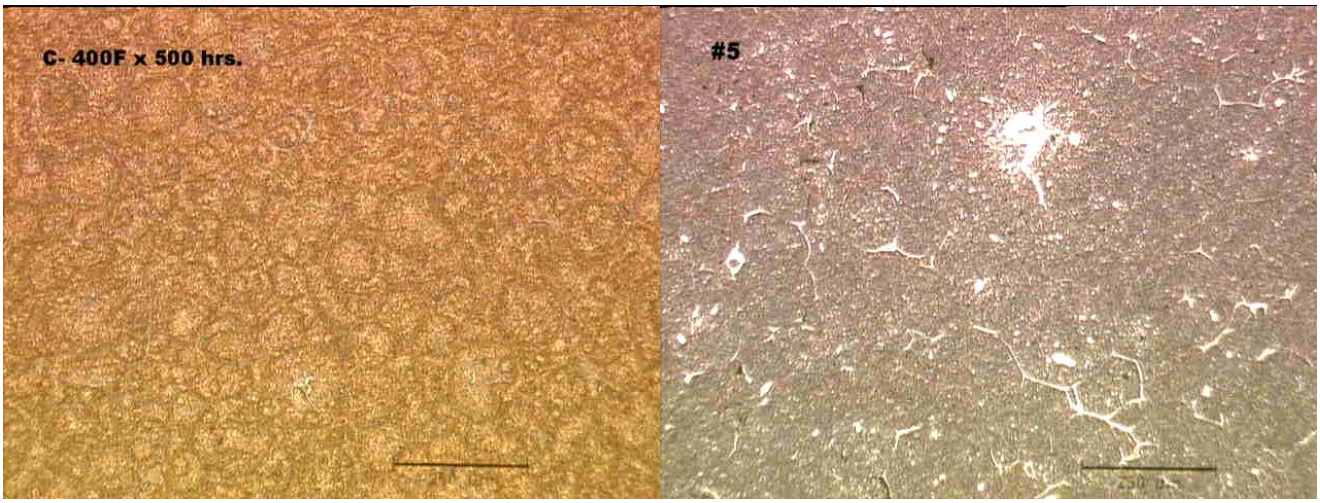

Figure 8. Comparison of the microstructure of tensile sample to billet sample of different batch at 100X. The microstructure of billet contains a larger number of large veins and defects.

Mechanical Behavior of Ceramic Materials for Heavy Duty Diesel Engines

A. A. Wereszczak, H. Wang, M. K. Ferber, and M. Lance
Oak Ridge National Laboratory

Objective/Scope

The application of more ceramic components in engines and transportation systems would be enabled if they could be confidently manufactured and machined faster (i.e., more cost-effectively) and if mechanisms that limit their mechanical performance were understood, predictable, and controlled. This project quantifies "quasi-plasticity/fracture thresholds" in ceramics (e.g., cubic oxides and non-oxides, nanoceramics and nanocermets, piezoelectric ceramics, micaceous ceramics, and traditional structural ceramics) and examines the competing mechanisms that dictate when and how quasi-plasticity or fracture dominates the other during controlled and instrumented static and dynamic indentation and scratch testings. The thorough understanding of the competition of fracture and quasi-plasticity in ceramics will enable improved and faster means of ceramic component manufacturing and surface engineering (e.g., ductile regime machining) and maximize mechanical performance when surface condition (e.g., bending) or when surface-located events (e.g., wear, impact) are service-life-limiters in engine and transportation system components.

Technical Highlights

A substantial amount of instrumented scratch testing occurred during the present reporting period. Testing of silicon nitride focused on the evaluation of Ceradyne's Ceralloy 147-31N, which is a reaction-bonded material used in cam roller followers. Evaluation of three 99.9% aluminas having mean sizes of 2, 15, and 25 µm (see Fig. 1) also proceeded - the rationale behind the alumina testing is to evaluate scratch response as a function of controlled grain size with the same chemical composition. Additionally, the testing of alumina affords the opportunity to map out residual stresses about the contact or scratch damage using optical fluorescence. Scratch damage evolution and its quantification are being related to machining and wear performance.

The interpretation of the load histories during scratch testing with respect to microstructural examination is ongoing. Normal and tangential forces are continuously monitored during the (pendulum) scratch test. Examples of these with associated microstructural damage are shown in Figs. 2-3 for Ceralloy 147-31N, and Figs. 4-5, 6-7, and 8-9, or the 2, 15, and 25 µm alumina, respectively. SEM observations show that there is an apparent grain size effect on the scratch responses; in particular, scratch forces oscillate more significantly during the scratching of larger-grained alumina corresponding to a greater amount of lateral crack formation.

Status of FY 2005 Milestones
Establish dynamic indentation and instrumented scratch testing facilities. Completed.

Communications/Visits/Travel
A. Wereszczak visited G. Quinn and J. Swab at NIST on 12 April 2005 to discuss the project's dynamic indentation work.

A. Wereszczak and H. Wang visited R. Bradt at the University of Alabama at Tuscaloosa on 20 April 2005 to discuss the project's dynamic indentation work.

Several discussions were held with Delphi's N. Hakim regarding PZT stacks for fuel injectors and their future characterization.

Publications
H. Wang and A. A. Wereszczak, "Mechanical Responses of Silicon Nitride Under Dynamic Indentation, in press, *Ceramic Science and Engineering Science Proceedings*, 2005.

G. Subhash, M. A. Marszalek, A. A. Wereszczak, M. J. Lance, "Scratch Resistance and Residual Stresses in Longitudinally and Transversely Ground Silicon Nitride," in press, *Ceramic Science and Engineering Science Proceedings*, 2005.

A. A. Wereszczak and T. P. Kirkland, "Exclusivity of Strength-Limiting Intrinsic and Hybrid Flaws," in press, *Ceramic Science and Engineering Science Proceedings*, 2005.

H. Wang, A. A. Wereszczak, and M. K. Ferber, "Characterization of Dynamic Indentation of Silicon Nitrides by Using Vickers Indentation, in preparation.

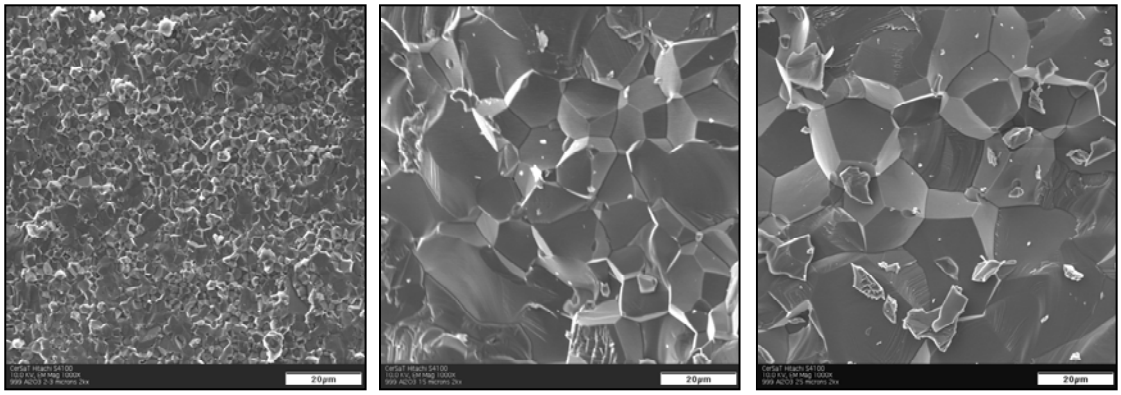

Figure 1. Microstructure of 99.9% aluminas with mean average grain size of (left) 2 µm, (middle) 15 µm, and (right) 25 µm.

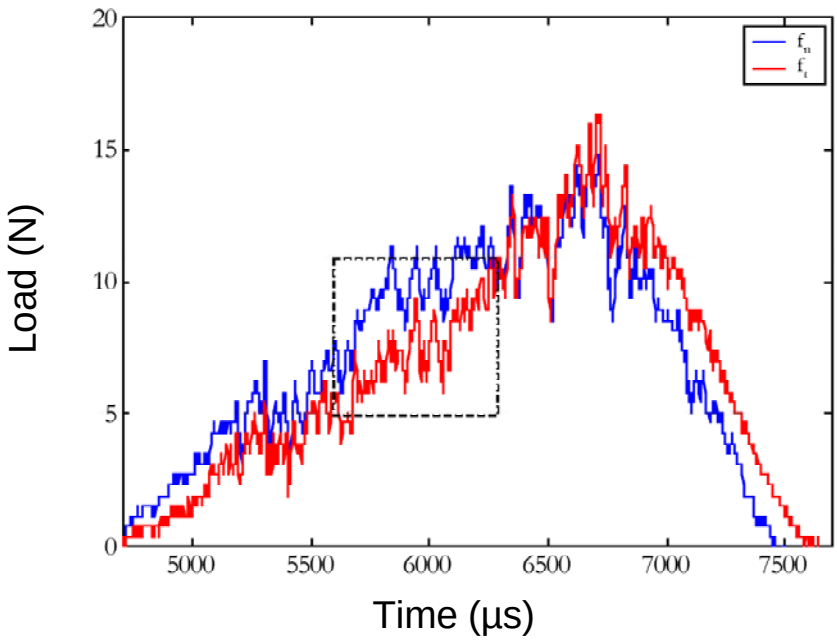

Figure 2. Example of normal (blue) and tangential (red) load histories during a Ceralloy 147-31N silicon nitride scratch test.

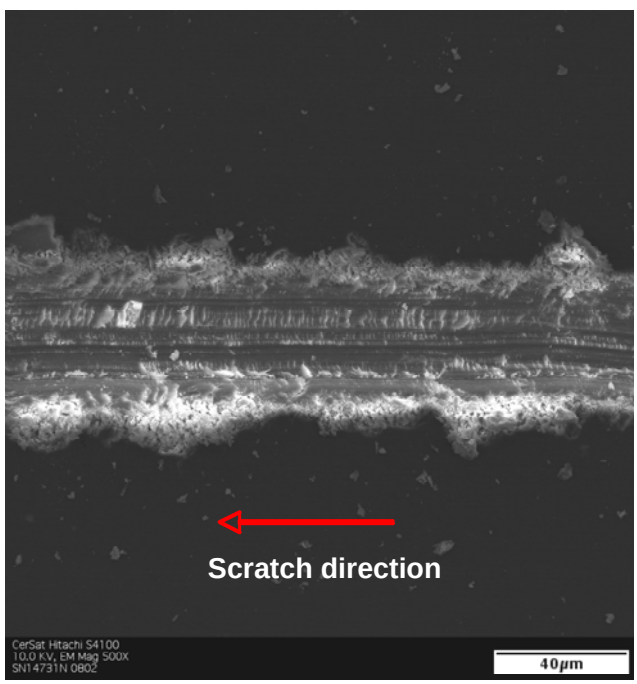

Figure 3. Scratch on Ceralloy 147-31N associated with boxed region in Fig. 2.

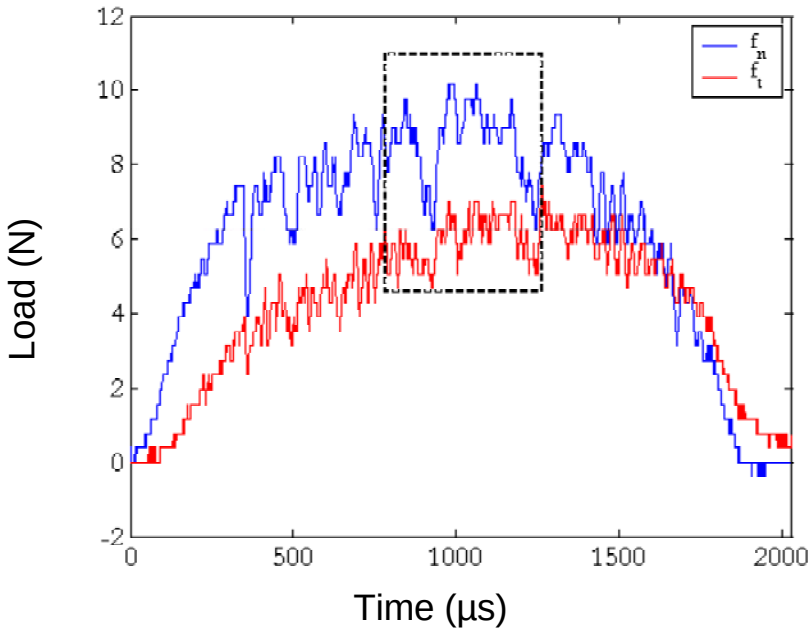

Figure 4. Example of normal (blue) and tangential (red) load histories during a 99.9% 2-µm alumina scratch test.

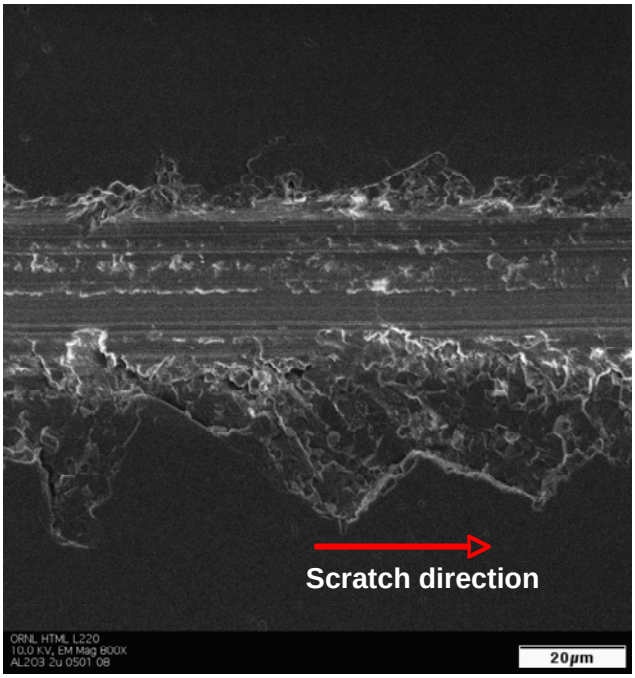

Figure 5. Scratch on 99.9% 2-µm alumina associated with boxed region in Fig. 4.

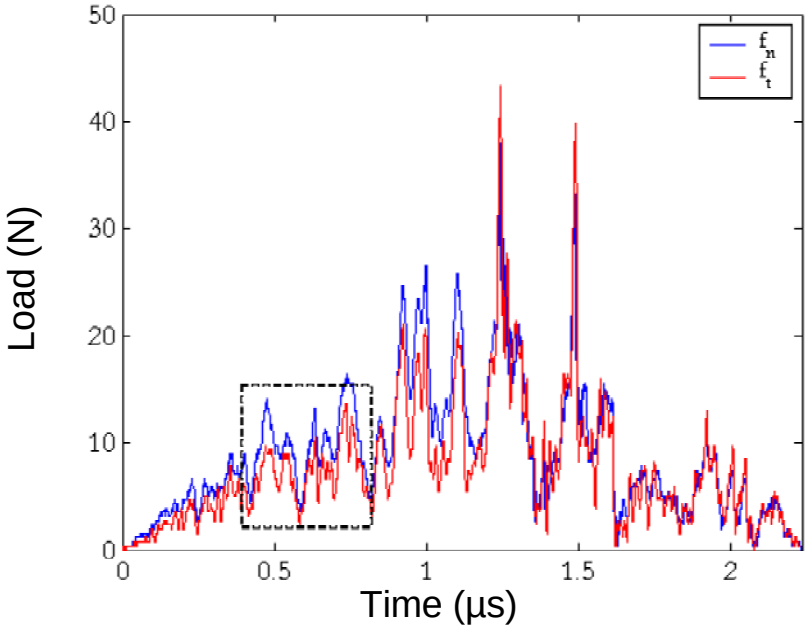

Figure 6. Example of normal (blue) and tangential (red) load histories during a 99.9% 15-μm alumina scratch test.

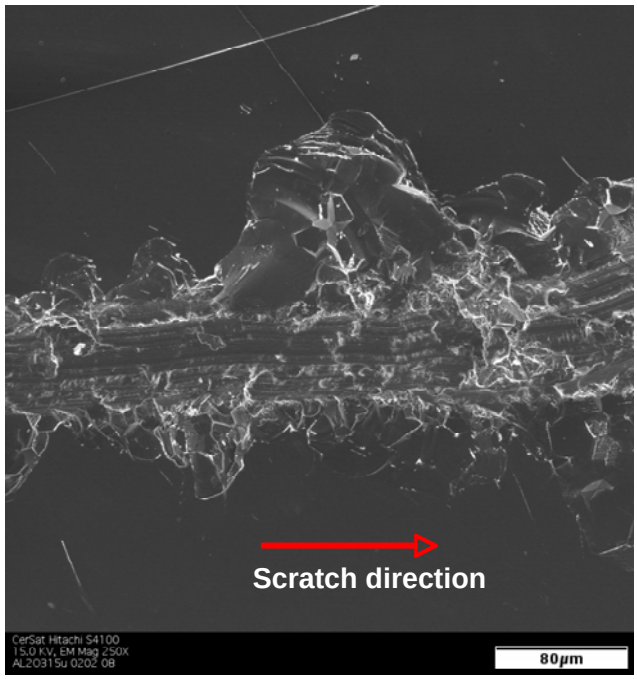

Figure 7. Scratch on 99.9% 15-μm alumina associated with boxed region in Fig. 6.

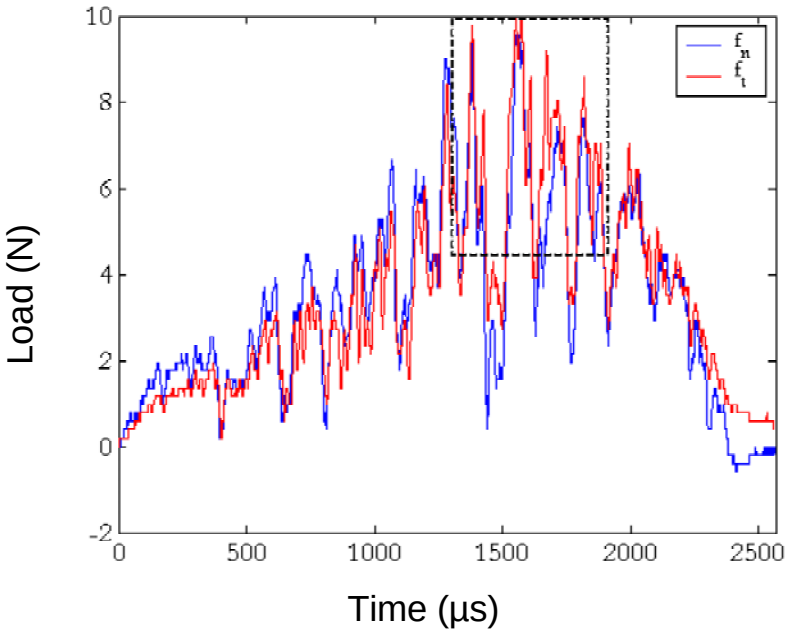

Figure 8. Example of normal (blue) and tangential (red) load histories during a 99.9% 25-μm alumina scratch test.

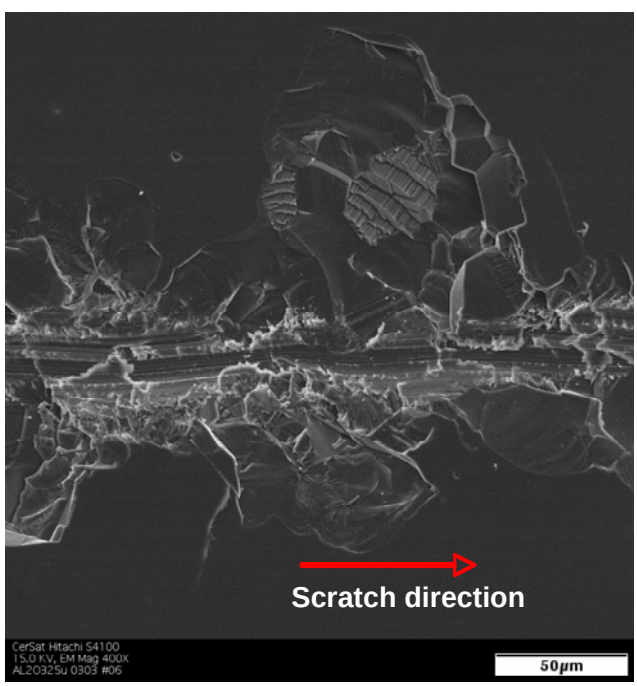

Figure 9. Scratch on 99.9% 25-μm alumina associated with boxed region in Fig. 8.

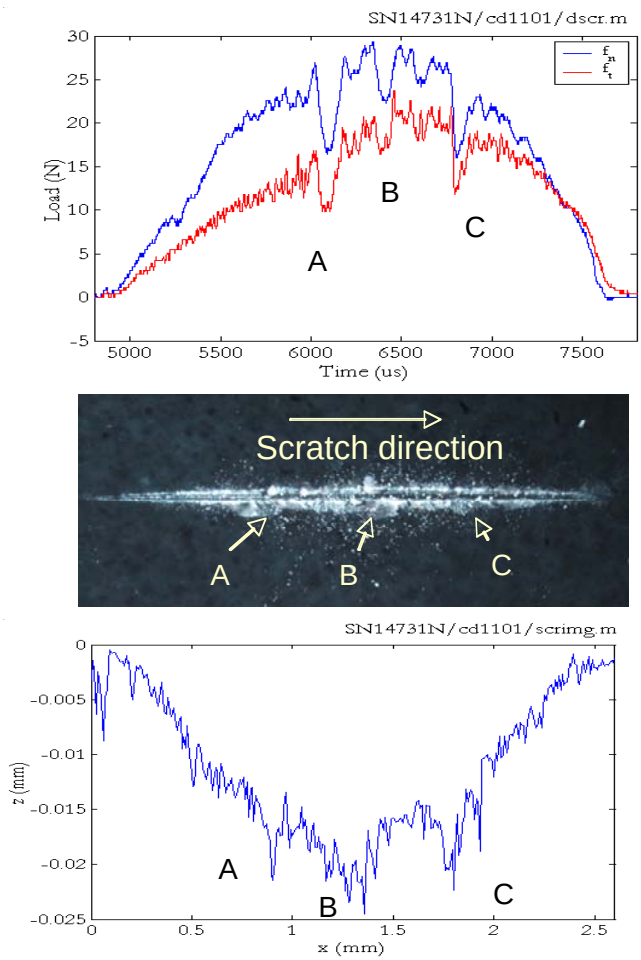

The scratch forces vary accordingly with the groove formation where valleys A, B, C in the signals correspond to the detached lateral cracks (chips).

The outline of scratch varies correspondently with the above force signals; valleys A, B, C indicate the possible torn groove bottom points due to the major chip formation.

Figure 10. Evidence of lateral crack formation is evident in the normal and tangential load histories (top graph) and in depth changes too (profilometry - bottom graph).

Next Generation Ceramics for Heavy Vehicle Propulsion Applications

Paul F. Becher
Oak Ridge National Laboratory

Objective/Scope

In addition to lower specific weight, ceramics have a number of attractive properties for application as components in various heavy vehicle systems such as electrochemical properties needed to develop advanced sensors and wear resistance and low coefficients of friction to increase life in moving components. Significant new opportunities are beginning to evolve with the advent of nanocrystalline materials. Initial findings show that nanocrystalline ceramics have substantially improved electrochemical properties, which are being explored in sensors for combustion and emissions controls, and auxiliary power sources. Studies have also revealed that ceramics with grain sizes < 100 nanometers can exhibit very high hardness, which may translate to greater wear resistance either in the form of coatings or components (e.g., for valve train components) or to create low friction surfaces to enhance engine performance.

The goal being to develop the technology to form "green" (unfired) bodies of nanocrystalline particles to allow one to devise pressureless sintering profiles to produce dense monolithic bodies with grain sizes < 100 nm. This is aimed at finding approaches to produce sizeable monolithic bodies for subsequent evaluation. The second thrust focuses on the mechanical and wear behavior of nanocrystalline ceramics and the influence of external parameters (e.g., stressing rate, temperature, environment (e.g., air, vacuum), and electric fields (in collaboration with researchers at North Carolina State University) on the plastic deformation behavior.

Technical Highlight

Pressureless sintering of zirconia nanocrystalline bodies shifted to the use of granulated dried powders derived from <20 nm particulates of zirconia. The granulation process allows one to make coarse particles (e.g., < 75 mesh) that can be formed into larger bodies by conventional cold uniaxial and isostatic pressing. This approach allows us to evaluate the sintering of large size bodies where the challenges in achieving fully dense bodies with ≤ 100 nm increase exponentially with increase in scale of the body, (e.g., by increasing the thickness for disks with centimeter scale diameters).

Preliminary vacuum sintering trials have shown that dense I mm thick disks of zirconia-1.7 mol. % yttria bodies can be obtained with grain sizes of 100 nm using an unmodified transient sintering profile. Current efforts are focused on increasing the density of the unfired bodies prepared from granulated powders and optimization of the sintering conditions to enhance the densification of thicker bodies.

Status of Milestones

New project

Communications/Visits/Travel

Continued weekly teleconferences with Prof. Jim Adair, Pennsylvania State University, and staff to discuss processing of nanocrystalline ceramics.

Publications

None

High Speed Machining of Titanium Project

Rahul Aphale
Third Wave Systems, Inc.

Objective/Scope

Develop Drilling Model for Solid Tools-

Development of Drilling modeling capability continued for the months of April 05 through June 05. Algorithms and computational formulatios were completed for steady state and exit state stage modeling. Development of graphical user interface for steady state and exist state stage modeling continues to be worked on. Benchmark simulations were performed at Third Wave Systems for verification of the model.

Technical Highlights

Figure 1 shows initial mesh generated for a Steady state stage simulation for Ti-6Al-4V material. Speed of 734 RPM and feed rate of 0.05 mm/rev was selected for this simulation. The Drill is positioned inside the workpiece such that it starts at full chipload from the beginning of the simulation. User specifies initial starting depth while generating the initial mesh. Benefit of performing steady state stage simulations is that it gives stedy state data relatively quickly. Figure 2 shows chip formation from steady state stage simulation. Results from this simulation will be compared against experiemental force measurements being conducted at the University of Michigan.

Status of FY 2005 Milestones

Development of Drilling Model is in process on schedule as per Milestone for FY 2005.

Communications/Visits/Travel

Group meeting for project particants was held on May 6th in Dearborn Michigan. Drilling Status updates were presented at the meeting and discussed with Dr.Jun Qu of ORNL and Rui Li of University of Michigan.

Publications

None.

References

None.

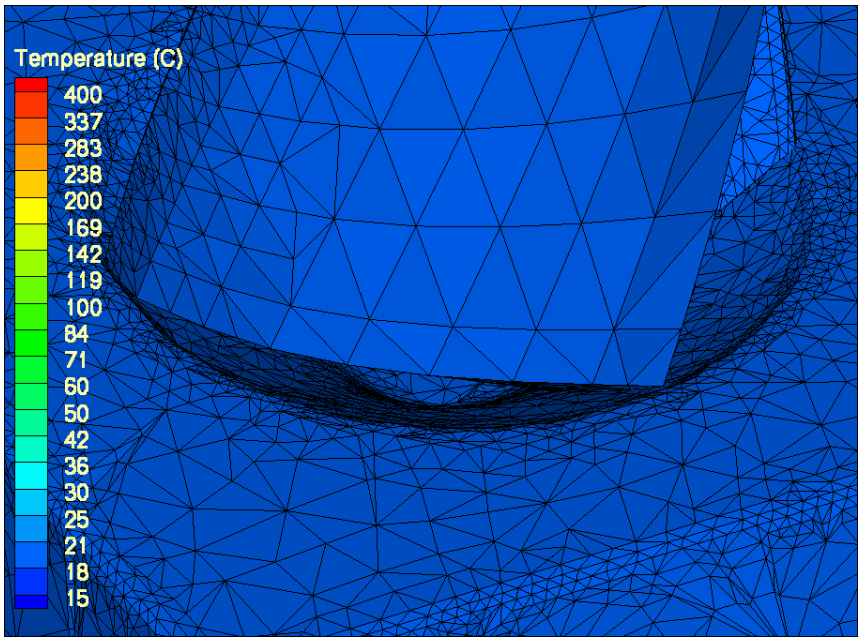

Figure 1. Initial Mesh Generated for steady state stage drilling

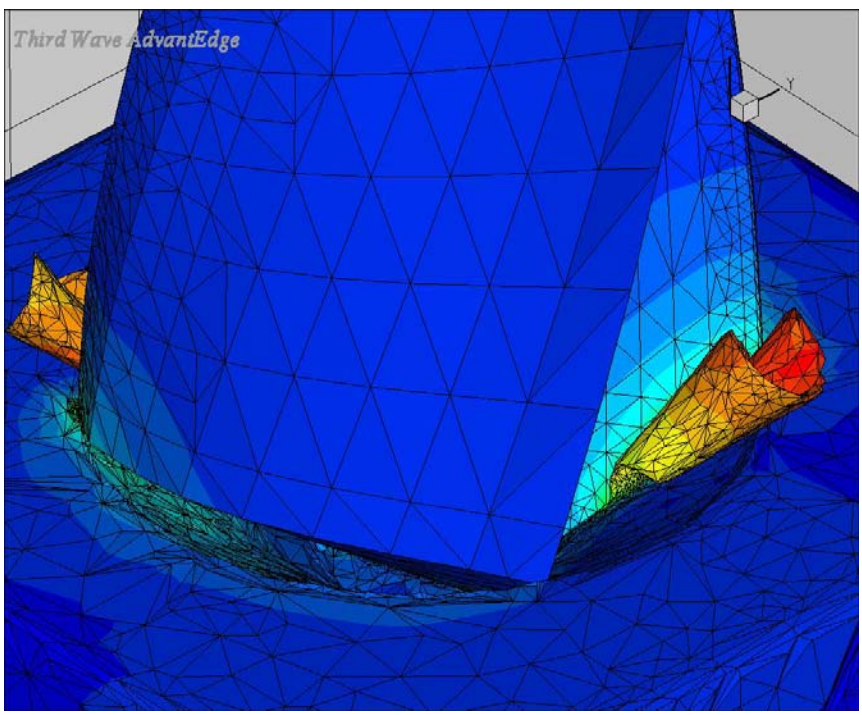

Figure 2. Initial Mesh Generated for steady state stage drilling

Synthesis of Nanocrystalline Ceramics

James H. Adair
Pennsylvania State University

Objective

Advanced particle processing will be used to produce dense, bulk nanocrystalline oxide ceramics. Two routes to obtaining well-dispersed powders (i.e., comminution and colloidal processing) will be emphasized. The large surface areas of such powders lead to large quantities of adsorbates, which must be removed both to enhance particle packing and subsequent sintering. Both reactive atmosphere and microwave thermolysis have merit and will be evaluated to eliminate adsorbates at low temperatures. This project will scale-up the processes to be able to produce dense YSZ ceramics with grain sizes less than 100 nm having sample dimensions ≥ 25mm in diameter by ≥3 mm in thickness to be delivered to ORNL for further testing. Additional effort will focus on fabrication of said samples with grain sizes < 50 nm for testing by ORNL staff.

Background

Particle processing has the potential to produce dense, bulk nanocrystalline materials with a variety of chemical compositions and architectures including composite materials. Outstanding challenges in particle processing to form bulk, dense nanograin-sized materials include the dispersion of the nanosize particles and control of gas evolution from the very high surface area compacts during sintering. Typically, nanometer size particulates suffer from a high degree of agglomeration, which results in poor particle packing (green densities < 40% of theoretical) and inhibits sintering and promotes undesirable grain growth. Two routes to obtaining well-dispersed powders include comminution and colloidal processing. Recent advances in colloidal processing have obtained high green densities (>50% of theoretical) with 8 nm YSZ particulates, which preliminary sintering efforts resulted in a translucent, fully dense 45 nm grain sized ceramic. Finally, gas evolution during sintering can occur due to the very high surface areas of nanoparticulate green bodies and disrupt sintering processes. While the thermodynamics and kinetics in the gas phase evolution reactions are reasonably well established, the fundamental science and engineering aspects must be addressed for each nanoparticulate system. Recent considerations indicate that innovative gas phase treatments (e.g., injection of reactive gases during the sintering cycle) can be used to overcome the undesirable effects of evolution gases from the nanoparticulate bodies during sintering.

The focus of research during the past quarter has been the preparation of dry-pressed yttria-doped zirconia pellets for sintering studies as well as the construction of a fast-fire furnace and dilatometer system. Pellets with a greater thickness were prepared in order to evaluate its effect on sintering behavior. Samples have been produced as thick as 5 mm with a consistent density between 47-49%TD using pan-dried, granulated powder. Uniaxial compression (25,000 psi, 170 MPa) followed by isostatic compression (30,000 psi, 200 MPa) resulted in crack-free, high green strength pellets.

In previous experiments, the effect of variations in washing procedures on drying and compaction behavior of nano-zirconia has been evaluated. It has been found that granulated bicine-washed zirconia compresses to a higher green density and exhibits higher green strength than oxalate-washed powder prepared in the same way. It is believed that bicine acts as a binder and lubricant between particles, whereas, oxalate crystallizes between particles upon drying, forming rigid necks which are difficult to fracture. A recent TGA study revealed near-identical weight loss events in zirconia powders washed with oxalate, bicine, and pH-adjusted deionized water. This suggests that the same organics are present in each sample, namely bicine, which is adsorbed on particle surfaces during hydrothermal synthesis. Furthermore, this also suggests that oxalate does not displace bicine during washing, and, as dispersion has been readily achieved in oxalate, bicine, deionized water, and ethanol, there is no advantage to adding oxalate or excess bicine. As a result, as-synthesized suspensions are now washed in deionized water which has been adjusted to pH 9 to minimize yttria dissolution.

Work planned for the next quarter includes verification and repetition of sintering results using the fast-fire furnace system as well as analysis of pore structure evolution during compaction and firing by multi-point BET and temperature-programmed desorption analysis.

Development of Titanium Alloys for Heavy-Duty Diesel Engines

Nan Yang, Jeremy S. Trethewey, Mike J. Pollard, Jesus Chapa-Cabrera and John A. Grassi
Caterpillar Inc.

Introduction

The present cost of producing titanium has significantly decreased, and the forecast is for the decreasing trend to continue, making titanium alloys an attractive alternative to other strong, lightweight materials. Turbochargers on diesel engines play an integral role in meeting emission regulations and controlling fuel economy. Caterpillar Inc. has introduced the use of two turbocharger systems on some on-highway diesel engines in order to meet current and future emission regulations. The presence of two turbocharger systems challenges the already limited under-hood space for on-highway truck applications. Therefore, the development of an alternative turbocharger system that is smaller and lightweight is of great interest.

Project Objectives

The purpose of this program is to develop one or more heavy-duty diesel engine components using titanium alloys. The chosen engine components must demonstrate an improvement in fuel efficiency while reducing emissions. Caterpillar has selected the turbocharger wheel as an engine component to be fabricated from titanium aluminide (TiAl). Additionally, Caterpillar has designed a turbocharger that will utilize the TiAl turbine wheel.

In order for the new design to meet the performance specifications of two turbocharger systems, a high strength, lightweight turbine wheel must be developed, which is the primary objective of this project. Thus, lightweight titanium materials (e.g. TiAl) are among the critical technologies for the successful development of this new turbocharger design that will meet transient emission regulations while improving the fuel efficiency and responsiveness of the engine in various applications.

Approach

An interdisciplinary team has been organized at Caterpillar to develop the TiAl turbine wheel. Staff members from the Advanced Materials Technology (AMT) lead and manage the project development efforts. Experts from the Large Engine Center (LEC) Air Systems division work with Engine Research to design and bench test the turbo wheel. Manufacturing and Process engineers from the Mossville Engine Center (MEC) work with machining experts at the Advanced Production Technologies to develop a cost competitive manufacturing implementation plan.

Quarter Summary

Supplier Readiness

A TiAl turbine wheel has been designed for application in the C175 engine. The new turbine wheel design will be validated via engine testing later this year. A batch of gas stand/engine test quality turbine wheels of the new design has been requested from Supplier A. Specimen bars requested from Supplier A for creep and TMF tests should be received in mid-July. Supplier B

is still developing their casting technology for larger size TiAl turbine wheels. The project plan was modified to reflect the new design availability dates.

Materials Characterization

Mechanical tensile testing at room and elevated temperatures was recently completed for the material from Supplier A. The results are being analyzed and compared to the results from Supplier B. A summary of the tensile testing results of the materials from Supplier A and B will be incorporated in the next quarterly report. Measurements for the thermophysical properties have been completed for the materials from both Supplier A and B. Apparent differences in thermal conductivity and coefficient of thermal expansion (CTE) could account for dissimilar thermomechanical behavior between the two materials. A lower thermal conductivity and higher CTE would result in larger thermal strain/stress in the turbine wheel at engine operating conditions.

Computer simulation will be conducted based on measured thermophysical properties to analyze the strain/stress difference for the two TiAl materials at the engine operating conditions. Thermomechanical Fatigue (TMF) testing conditions will be selected based on the simulation results. The TMF testing will begin in the next quarterly reporting period. The specimen geometry for creep testing has been determined and the tests will begin during the same period. The creep tests to be conducted at relatively lower stress and lower temperature will be performed at ORNL.

Friction Welding

Successful friction welding (FW) was accomplished to produce joints between TiAl turbine wheels and Ti-6Al-4V bars. Joining the TiAl turbine wheel to its shaft is a critical technology for this project. In the previous FW trials, cracking that occurred during the later stage of the process presented one of the main technical challenges in the project. Based on the input from the FEA simulations, part geometry has been modified and process controls have been incorporated. With these modifications, the most recent iteration of friction welding trials has produced crack-free joints with tensile strength higher than the base TiAl material.

Representative photographs of these TiAl turbine wheels joined by FW are shown in Figure 1. All of these FW joints are free of visual cracks. Using non-destructive evaluation (NDE) techniques, no crack or defect could be identified on the weld or heat affected zone (HAZ). As shown in Figure 2 (a), the Eddy current technique is not able to capture any surface or subsurface cracks at the joint. Also, in Figure 2 (b) and (c), ultrasonic inspections did not detect any radial crack at the weld, demonstrating the weld interface is rather uniform. All of these inspection results indicate the joint quality has been significantly improved over the previous FW trials. Mechanical tensile tests show that the highest strength obtained is about 380 MPa. All of the tensile test specimens failed at least several millimeters away from the welding interface in the TiAl turbine wheel side, which is out of the HAZ. Figure 3 shows the fracture surface nearly 20 mm away from the joint interface, in which case the stem is completely pulled out of TiAl turbine wheel. Based on the origin of failure, it is reasonable to assume the joint strength is higher than that of the base TiAl material. It should be noted that the TiAl base material failed below its normal strength due to bending loads introduced during the test. The tensile specimens

could not be adequately aligned to avoid the bending load because the specimens are not standard bars and no suitable fixtures were readily available for these tests.

The FW conditions used to produce the best quality for the successful joints have also been used for joining TiAl turbine wheels from another supplier to Ti-6Al-4V bars. Among the three trials, however two failed due to thermally induced cracks. The third trial, though free of visual fractures, is yet to be examined using NDE techniques. The difference in the friction welding results between the TiAl materials from various suppliers is attributed to the difference in their thermophysical properties. A more thorough analysis of the welding results and comparison of the thermophysical properties between the materials from the suppliers are yet to be made. A modification of the welding conditions used for the TiAl turbines will be completed in order to produce a quality joint.

Using a Taguchi matrix, twenty friction-welding trials at different conditions were compiled to evaluate the joining of steel to Ti-6Al-4V bars. Consequently, samples of the steel bars and TiAl bars have been joined without any visual thermal cracks. These joined bars are to be examined using NDE techniques followed by mechanical testing. The samples from these welding trials are yet to be examined and the results will be presented in the next quarterly report.

Brazing

As an alternative joining method, we have examined brazing TiAl to 4140 steel specimens. Different brazing alloys are being evaluated to determine if a braze joint between γ-TiAl and 4140 steel can be as strong as the TiAl base metal. Previous trials have focused on Ti-base or Ti-containing alloys, but these tend to form brittle Ti-Fe intermetallics at the steel/joint interface.

Several brazing trials were completed to analyze the effects of brazing with different alloy systems. The first set of trials used a compressive force to hold the samples together. Once the braze alloy melted, the gap would be reduced to near zero. The tensile test results of these trials are shown in Figure 4. All of the samples fracture at the braze joint. In general, the brazing strength increased as the time at temperature decreased. This effect occurs because holding at temperature allows greater diffusion (and therefore phase formation) to occur. The formation of brittle intermetallics lowers the strength of the joint. The strength of these joints might be limited by the absence of any measurable gap. This allows the TiAl and steel to be in closer contact during the brazing, possibly increasing the likelihood of brittle phase formation.

Further trials were completed on Alloy D to optimize the joint strength while maintaining a measurable gap. The gap was fixed at 80 μm (may have changed slightly during brazing), and the samples were held at the brazing temperature for 30 seconds. This resulted in partial fracture of the TiAl instead of the braze joint during tensile testing. Figure 5 shows TiAl still brazed to the steel surface after tensile testing. However, this process has not produced a sample that fully fractures in the TiAl. In addition, the joint strength has varied significantly.

It was assumed that the portions not fractured in the TiAl were caused by poor wetting, since the grinding marks were still visible on the steel surface. However, SEM analysis revealed that a very thin Ti-Fe intermetallic formed at the steel/braze interface despite the relatively wide gap, short time at temperature, and low solubility of Fe and Ti in the braze alloy. In areas that did not

fail in the TiAl, fracture occurred at this Fe-Ti intermetallic layer. Therefore, modifications must be made to the brazing process to limit the time at temperature, or create a physical barrier to diffusion of Ti to the steel/braze interface.

Foreign Object Damage (FOD) Testing

Catastrophic damage due to impacts from a foreign object is a primary concern when using materials with limited ductility in a turbine application. The first round of testing that was outlined in the previous quarterly report has been completed. The blade arrays of six turbine wheels (each wheel has 11 blades) have been impacted and results have been collected. This study aims to examine the following sets of questions:

- **TiAl vs. Nickel-based blades:** What impact energy is required to initiate failure in a production nickel-based blade? What failure modes are observed? How do the impact energy and failure modes compare to TiAl blades from Supplier A and TiAl blades from Supplier B?
- **Blade thickness:** How does the thickness of the TiAl blades affect their ability to withstand foreign object impacts? What must the blade thickness of a TiAl blade be to sustain the same damage as a production Ni-based blade?

The test setup is pictured in Figure 6. The projectile is loaded at the rear end of the feed-tube and projected towards the stationary turbine wheel by a burst of high-pressure Helium. A set of two lasers and receptors measures the projectile's velocity as it exits the feed-tube. The projectile impacts the blade in the circled region of Figure 6. For the first round of impact trials, a 2.5 mm diameter 52100 chrome steel ball was used as the projectile.

It was found that Supplier A's thin TiAl blades (~2.16 mm) withstood impacts up to ~140 m/s before fracturing while the thick TiAl blades (~2.67 mm) withstood impacts up to ~225 m/s before fracturing. The Ni-based blades (~1.14 mm) withstood impacts up to ~500 m/s before a hole is spalled through the blade. It is not surprising that the Ni-based wheels withstand much higher impact energy (~mv^2) before failing. The apparent "brittle" nature of the TiAl initiates the cracking/fracture damage while the ductile nature of the Ni-based blade accommodates this damage with plastic deformation until the impact energy reaches the material's ultimate strength. Figure 7 shows the types of deformation seen in TiAl blades.

Lacking statistical data to draw definite conclusions, a critical observation is that the damage in all TiAl impacts is localized. The stationary TiAl turbine wheel did not shatter when impacted with a foreign object. A wheel rotating at 100,000 rpm may demonstrate a different behavior, but this has not yet been tested.

Since the current 52100 chrome steel ball has relatively high hardness, density, stiffness and strength, it is not representative of the oxide scale that would be a typical foreign object in the operating environment of a turbine wheel. To more closely emulate the behavior of an impact with oxide scale, alumina spheres will be used for the remainder of the trials. A more thorough report on this study will be presented in the next quarterly report.

TiAl Cost Model – EHK Technologies

Ed Kraft completed an economic model of investment casting which can be used to determine the major cost drivers, and study the effects of alternative process routes. This economic model was constructed using understanding of the investment casting process gained from visiting several facilities, plus discussions with many suppliers of equipment and materials to this industry. The data included in the model are primarily those obtained from the industry suppliers, and verified as reasonable by comparison with proprietary data of investment casting companies. No proprietary data is explicitly included in the model. The model was developed using one of Caterpillar's γ-TiAl alloy turbine rotors as the basis.

For any alloy, material source or process scenario studied, casting feedstock is the major cost driver. No other factor comes close to the importance of casting feedstock in overall manufacturing cost. The next most important cost factor is electric power, followed by casting yield. "Business Costs" are added to manufacturing costs to arrive at Price in this analysis. These factors may be subject to negotiation between buyer and seller. Particularly in a situation where one factor (raw material in this case) is such a high portion of cost, this Business Cost factor may be reduced by such negotiation.

Presentations & Relevant Travel

A presentation was given to DOE staff members for an annual program review on April 27. One of the authors traveled to MTI in South Bend, IN on April 11, 12 and 13, and June 13, 14 to conduct the friction welding trials (TiAl / Ti6Al4V wheel to bar, and 4140 steel/Ti6Al4V and 304 SST/Ti-6Al-4V bar to bar). Another author traveled to the University of Dayton Research Institute (UDRI) in Dayton, OH to carry out FOD tests.

Plans for Future Work

Upon successful joining of smaller TiAl turbine wheels to Ti-6Al-4V bars, the joining technology is to be scaled up to the larger TiAl turbine wheels. A design of experiments for FW of the large size TiAl turbine wheels will be completed. The experiments will then be carried out with the objective of achieving a quality joint between TiAl and Ti-6Al-4V in the large size TiAl turbines comparable to the smaller TiAl turbine wheels. The 4140 steel bars will then be friction welded to the Ti-6Al-4V bars that are already joined to TiAl turbine wheels to complete the development of a robust joint. Upon receiving the materials from Supplier A, TMF and creep test will start in the next quarter.

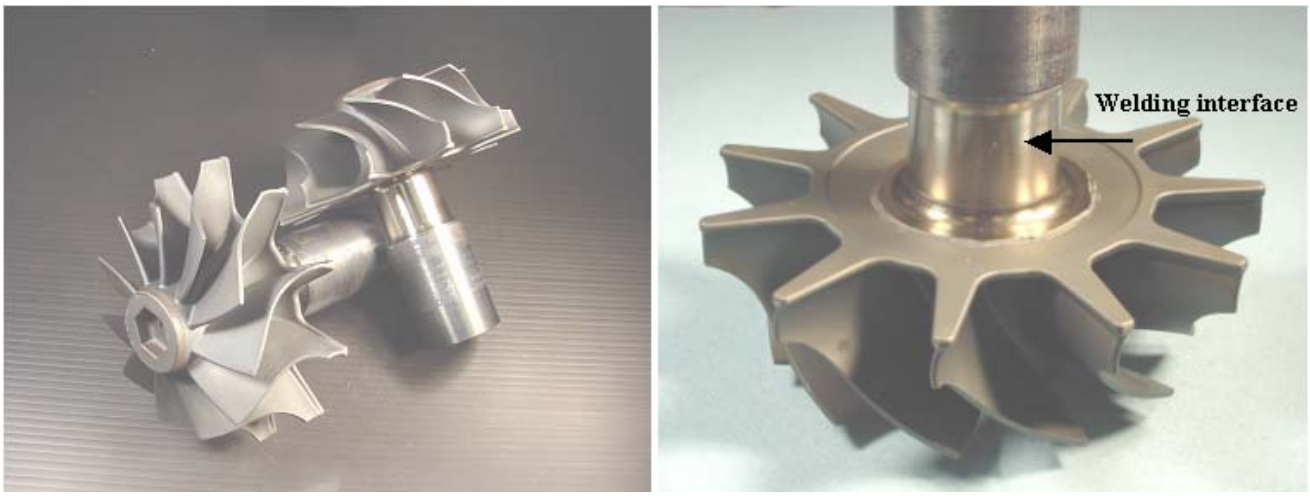

Figure 1. TiAl turbine wheels welded to Ti-6Al-4V shafts by friction welding.

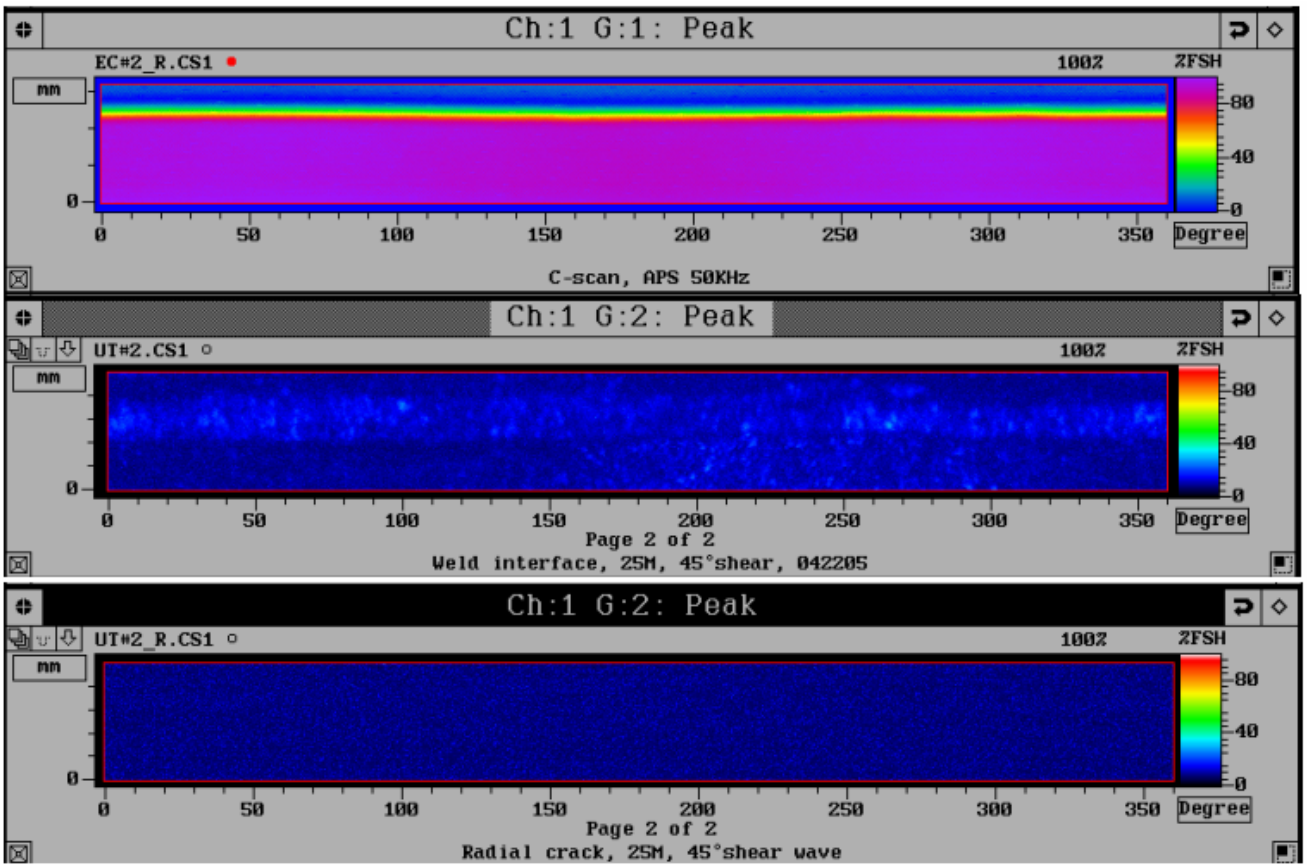

Figure 2. NDE results at the weld and heat affected zone. No surface or near surface cracks could be detected using Eddy current technique (a); ultrasonic inspections also indicate that the welding interface is uniform (b) and free of radial cracks (c).

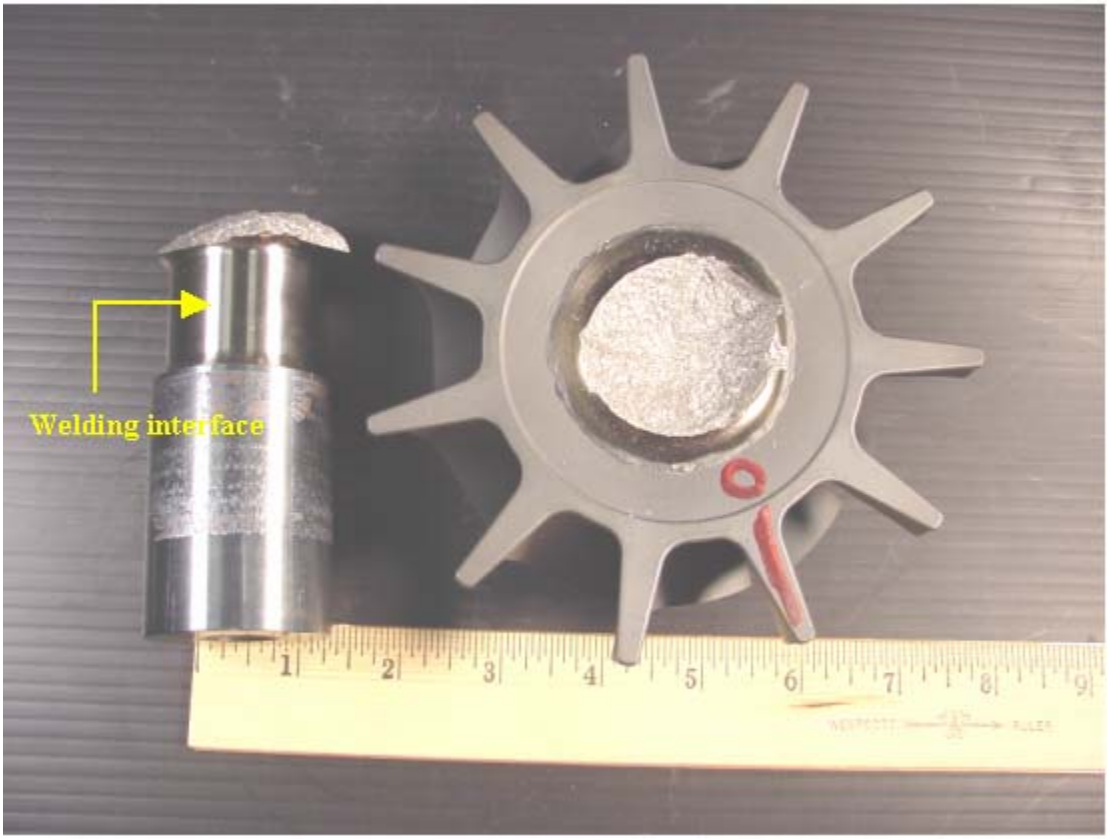

Figure 3. Friction welded TiAl turbine wheel failed about 20 mm away from the friction welding interface in mechanical tensile test. The hub of TiAl turbine wheel is completely pulled out of TiAl wheel.

Trial	Braze Alloy	Preheat	Hold Time	Force (MPa)	UTS (MPa)	Comment
1	A	none	1 min.	10	264	
2	B	none	1 min.	10	295	
3	B	none	5 min.	10	231	
5	B	540C 20min	20 s	10	320	
6	B	540C 20min	20 s	40	211	Severe Steel Deformation
7	C	none	20 s	10	277	
11	D	none	30 s	10	320	

Figure 4. Initial brazing trial tensile test results.

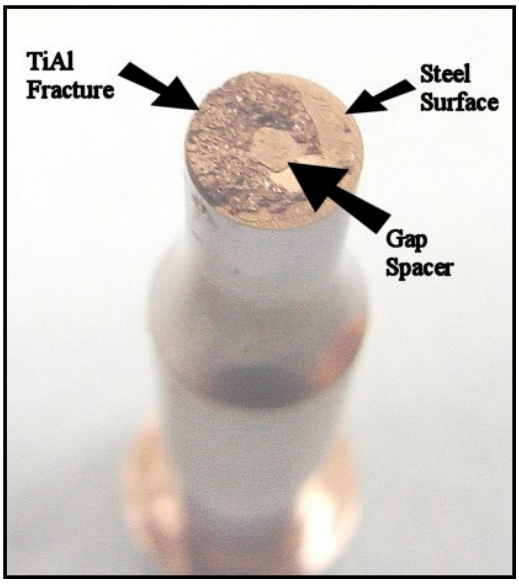

Figure 5. Fracture surface of brazed joint using alloy D showing areas of bonding of TiAl to the steel.

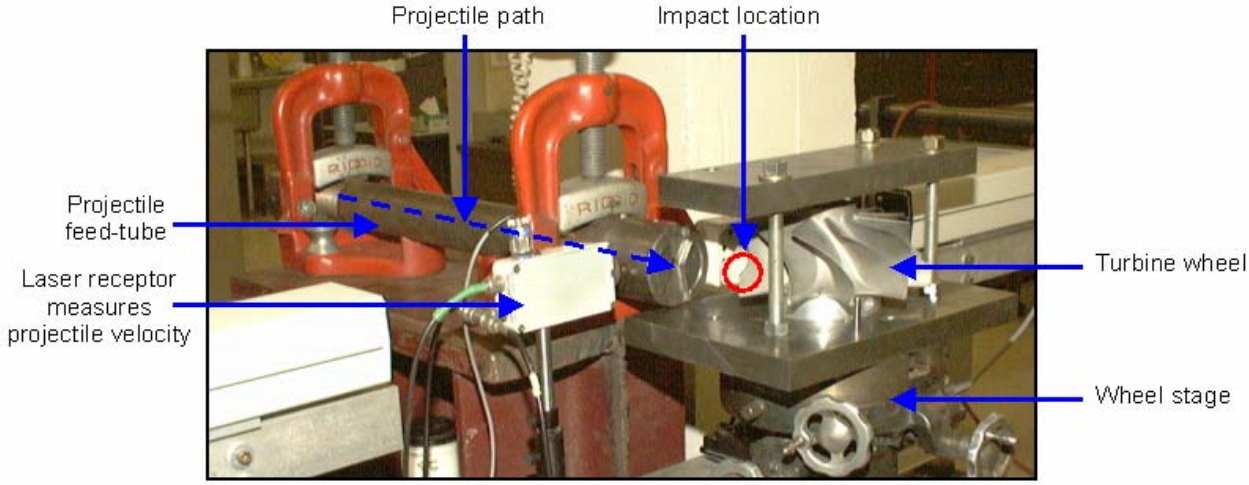

Figure 6. Turbine wheel FOD experimental test setup

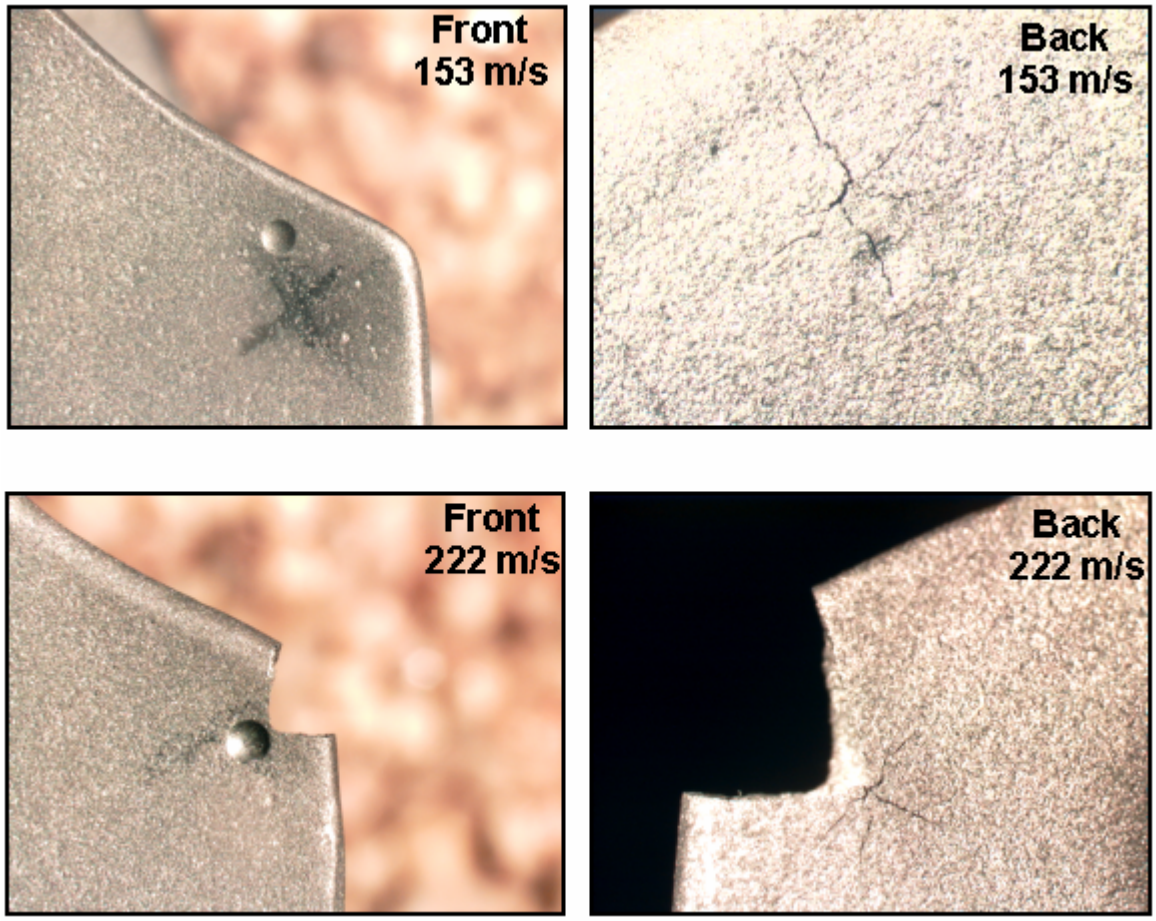

Figure 7. Representative images of TiAl blade (2.16 mm thick) FOD failure

Rolling Contact Fatigue

A. A. Wereszczak and W. Wang
Oak Ridge National Laboratory

O. M. Jadaan
University of Wisconsin-Platteville

Objective/Scope

The understanding and control of contact damage behavior of ceramics under rolling and sliding conditions are enablers to more widespread utilization of ceramics as cam followers, valves, valve seats, and other important transportation-related components. International interest exists to understand the fundamentals of rolling contact fatigue (RCF) of ceramics and coated metals because greater control (or minimization) of RCF will result in longer life of such components. Rolling contact fatigue is internationally studied through a variety of test methods and analytical approaches; interest exists in the present project to link their measured performances. Toward that, RCF studies (primarily of Si_3N_4) involving both international and domestic interactions are being pursued in Annex III of the International Energy Agency (IEA) agreement.

Technical Highlights

C-Sphere Analysis

Quite a bit of progress involving the C-sphere strength testing occurred during the present reporting period. This specimen was conceived and developed to measure strength of bearing-grade Si_3N_4 balls and to relate that to surface-located strength-limiting flaws (e.g., machining damage) ***and to ultimately link those flaw populations to rolling contact fatigue performance***. A slot was machined into the balls to a set depth to produce the C-sphere geometry. C-sphere specimens are then diametrally compressed to produce a monotonically increasing hoop tensile stress at their surface that ultimately caused their fracture (see Fig. 1). Strength is determined using the combination of failure load, C-sphere geometry, and FEA.

The stress field was used to determine C-sphere effective areas and effective volumes as a function of Weibull modulus. A quarter symmetry model for the C-sphere specimen is shown in Fig. 2 with the mesh distribution that was ultimately used to evaluate its effective volume and area. Solid95 tetrahedral elements were used, and a 100 N point load was applied to the sphere's apex. The mesh contained 52703 elements and 76682 nodes. As can be seen from Fig. 2, finer mesh density was used in the region where high tensile stresses would develop, gradually getting coarser towards the area where the load is applied and the overhang section. The ball from which the specimen was simulated had the dimensions of a 12.7 mm diameter and a slot width of 6.35 mm.

The issue of artificially high stress concentration within the narrow zone under the applied point load and its effect on the computed effective sizes was considered. In the virtual world of FEA, the load is applied as a perfectly concentrated point load, which causes stress singularity in that region. This is an idealization of what physically takes place where distributed load acting over

a narrow area is actually applied. In other words, as the mesh gets finer the stress under the load will increase indefinitely making the model and hence the effective sizes mesh dependent.

To understand the issue of stress singularity under the point load, both nodal and element first principal stress distributions are shown in Figs. 3-4 for the intermediate and fine mesh models, respectively. A nodal plot smoothes the stress distribution by averaging the stresses at that point in all the elements having that node in common. This smoothing is masking the very high stresses taking place within the individual elements, which if not removed would yield erroneous effective size calculations. This is because when the effective size is computed, the stress distribution is normalized with respect to the maximum effective stress in the component. If this maximum effective stress were incorrect, due for example to a localized stress concentration, as is the case for this model, then the computed value would be incorrect. In order to unmask the high nodal stresses, element stress plots are used which display the actual nodal stresses as computed for each element.

The nodal and element first principal stress distributions for the C-sphere specimen using the intermediate mesh model are shown in Fig. 3. As can be seen from the nodal plot, the maximum tensile stress is computed to be 132.1 MPa taking place at the side of the sphere as expected. However, when the element stress plot is examined, the high tensile stress (306 MPa) region shifts to the area under the load, which is obviously an artifact of the point load effect. For the fine mesh model (Fig. 4), both nodal and element stress plots show the highest tensile stress region to be under the point load, with the maximum first principal nodal and element stresses increasing to 244 MPa, and 644 MPa, respectively. Figures 3 and 4 clearly show that the stresses under the load are extremely mesh dependent and will keep changing as the mesh changes, while for the rest of the specimen the stresses have long converged even for the coarse mesh specimen model.

In order to take out the effect of localized stress concentration on the effective size calculations, the artificially high stressed elements under the load were removed. The remaining elements, comprising the vast majority of the specimen, were then used to assess the specimen's effective sizes. The nodal and element stress distribution plots for the C-sphere model are shown in Fig. 5, with the highly stressed elements carved out. One would then observe from these plots how the maximum tensile stress of 132 MPa shifts back to the side of the specimen where it should be. The fact that both the nodal and element stress plots yield the same stress distribution indicates that the suspect elements were successfully removed and that the remaining model can now be used to compute the effective sizes. Hence, it is the model in Fig. 5 that was utilized to compute the effective area and effective volume for the C-sphere specimen.

The effective area (A_e) and effective volume (V_e) as function of Weibull modulus for the C-sphere specimen are illustrated in Figs. 6-7, respectively. The effective sizes were computed using the following equations:

$$A_e = \left(\frac{\sigma_0}{\sigma_e}\right)^m \ln\left(\frac{1}{1-P_f}\right)$$

$$V_e = \left(\frac{\sigma_0}{\sigma_e}\right)^m \ln\left(\frac{1}{1-P_f}\right)$$

where σ_0 is the scale parameter, m is the Weibull modulus, σ_e is the maximum effective stress (computed by CARES/Life), and P_f is the probability of failure (computed by CARES/Life). The effective sizes are independent of the scale parameter since they only vary with geometry, loading, and the Weibull modulus. Hence, the scale parameter was assigned a random value in order to carry out the reliability and effective size calculations.

Experimentation

To achieve familiarity with the new C-sphere geometry, approximately 30 finished Si_3N_4 spheres were machined according to Fig. 1 and were strength tested. The failure loads and geometrical parameters are now being combined to calculate strength and those results will be included in the next Quarterly report.

All four machined ball sets have been received (see Table I). Bournemouth University is using the one larger diameter set to reduce to a 12.7 mm diameter using an internally developed lapping procedure that will essentially yield a fourth (lapped) finish condition.

Table I. Grinding Conditions for Silicon Nitride Spheres.

Diameter & Finish	Step	Wheel	Removal	Removal per pass
12.7 mm / 0.500"	1 (roughing)	accepted practice		0.001”
	2 (induce damage)	100 grit	0.004”	0.001”
Coarse	3 (finishing)	600 grit	0.0005”	0.0001”
13.2 mm / 0.520"	1 (roughing)	accepted practice		0.001”
	2 (induce damage)	100 grit	0.004”	0.001”
Coarse	3 (finishing)	600 grit	0.0005”	0.0001”
12.7 mm / 0.500"	1 (roughing)	accepted practice		0.001”
	2 (induce damage)	180 grit	0.004”	0.001”
Fine	3 (finishing)	600 grit	0.0005”	0.0001”
12.7 mm / 0.500" RCF-Conventional	“Accepted” practice for RCF test bar finishing			

The utility of using resonant ultrasound spectroscopy (RUS) to quantify elastic properties of Si_3N_4 balls, to assess consistency of those properties, and (hopefully) be able to non-destructively proof test them or identify pre-existing flaws is under exploration. H. Trivedi of UES (an Air Force Research Laboratory contractor) forwarded numerous Si_3N_4 balls that were damaged from their RCF testing for attempted RUS characterization and that is underway. Part of those supplied balls included pristine Toshiba TSN-03NH balls whose elastic properties were measured with the RUS and compared with those of NBD 200 and SN101C silicon nitrides.

Their comparison is shown in Fig. 8 and it was observed that the TSN-03NH balls showed the least amount of variability in those properties of the three Si_3N_4 compositions. The elastic properties of the three 12.7 mm diameter sets listed in Table I were also measured with RUS and those results are shown in Fig. 9. Several of the balls showed variability but it may be argued that close clustering of data suggest that most of the ball diameters and material density were uniform and that machining condition did not affect that.

Miscellaneous

Wei Wang, a PhD candidate co-advised by Prof. Mark Hadfield at Bournemouth University and ORNL's Wereszczak, commenced his 6-month research visit at ORNL during Quarter 3. Mr. Wang is performing three-ball-on-rod testing while at ORNL and assisting in the C-sphere strength and material characterization.

Japan's AIST will start a three-year standardization project of RCF testing funded by Japan's METI, Japan, in Quarter 4 and the present project will collaborate. AIST's W. Kanematsu invited this project participation for the purpose of performing three-ball-on-rod RCF testing. The UK and Germany will also participate. AIST will provide materials for the testing.

Status of FY 2005 Milestones

Characterize the effect of sub-surface machining damage on Si_3N_4 rolling contact fatigue performance and submit paper to the open literature on the results and interpretations. [09/05] *Delayed - the machining of the last set of ceramic balls was delayed and they were just received late in the 2nd quarter.*

Communications/Visits/Travel

- Discussions with Mark Hadfield (Bournemouth University, UK) occurred regarding the RCF testing and characterization of their bearing grade Si_3N_4's.
- Discussions with Vimal Pujari (Saint-Gobain Advanced Ceramics, Northboro, MA) occurred regarding the RCF testing and characterization of their bearing grade Si_3N_4's.
- Wereszczak will be traveling to the UK early in Quarter 4 to visit R. Morrell at the National Physical Laboratory (Teddington), M. Hadfield at Bournemouth University (Dorset), and P. Warren at Pilkington (Ormskirk). Rolling contact fatigue or Hertzian indentation or both will be themes during all three visits.
- Wereszczak and Wang will be visiting H. Trivedi at UES (Dayton, OH) in Quarter 4 to discuss RCF testing interactions.

Publications

- A. Wereszczak, W. Wang, O. M. Jadaan, and M. J. Lance, "Strength of a C-Sphere Specimen", abstract submitted to the January 2006 Cocoa Beach conference.
- Y. Wang, M. Hadfield, W. Wang, and A. A. Wereszczak, "Rolling Contact Fatigue of Ceramics," in internal review, to be published as a DOE/ORNL Technical Memorandum.

References

None.

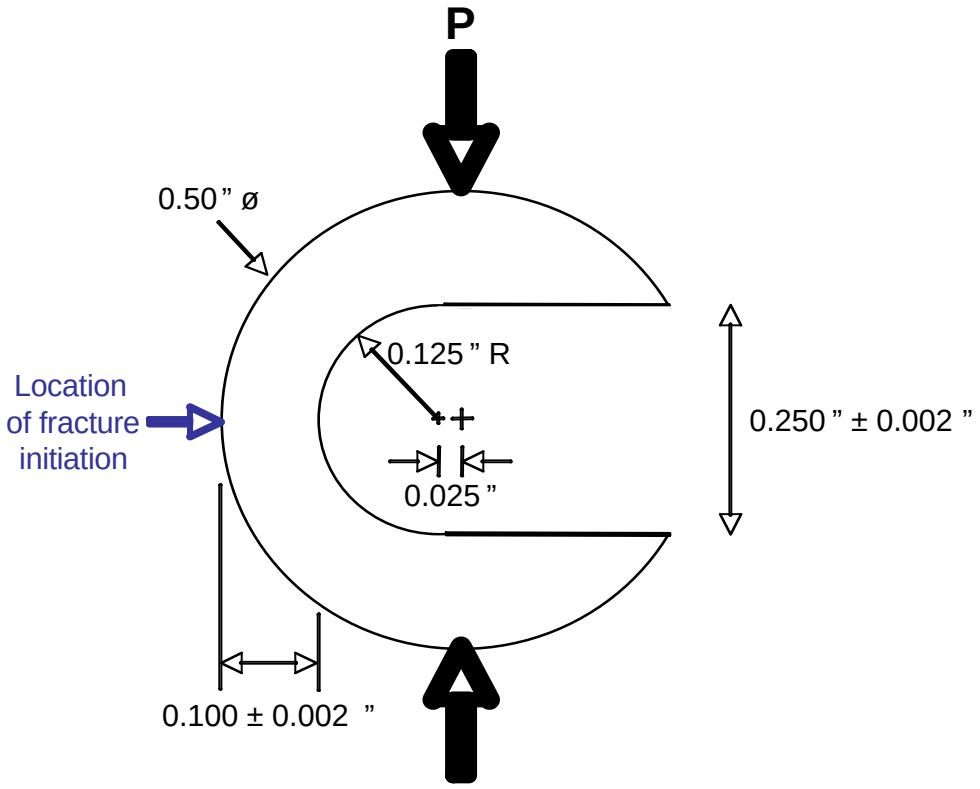

Figure 1. Schematic of the “C-Sphere” test specimen and its diametral compressive loading. Fracture will initiate at the outer surface and propagate radially inward.

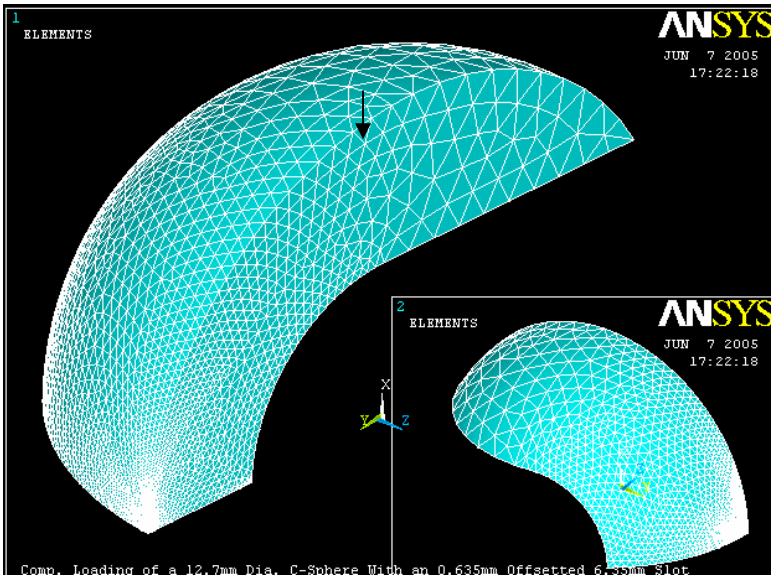

Figure 2. Mesh distribution for ¼ symmetry model of the C-sphere specimen, having 52703 elements and 76682 nodes. Three different mesh densities were used to evaluate the specimen and they were coarse (8497 elements), intermediate (16090 elements), and fine mesh (shown-52703 elements).

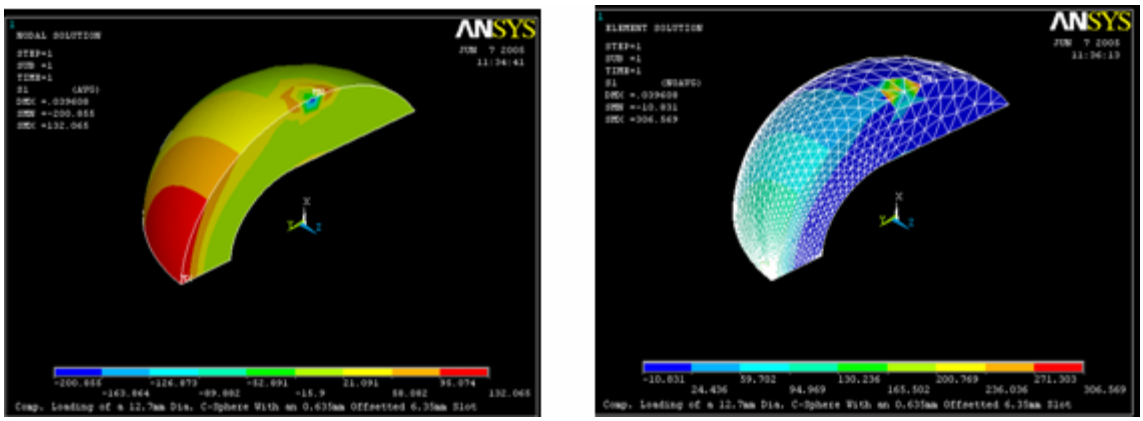

Figure 3. Nodal first principal stress distribution (left) and element first principal stress distribution (right) for the C-sphere specimen, using the intermediate mesh model.

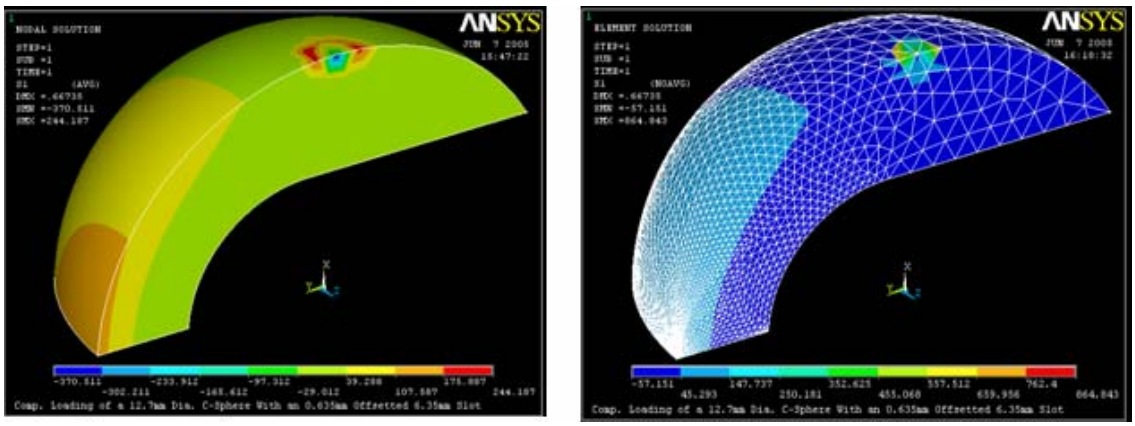

Figure 4. Nodal first principal stress distribution (left) and element first principal stress distribution (right) for the C-sphere specimen, using the fine mesh model.

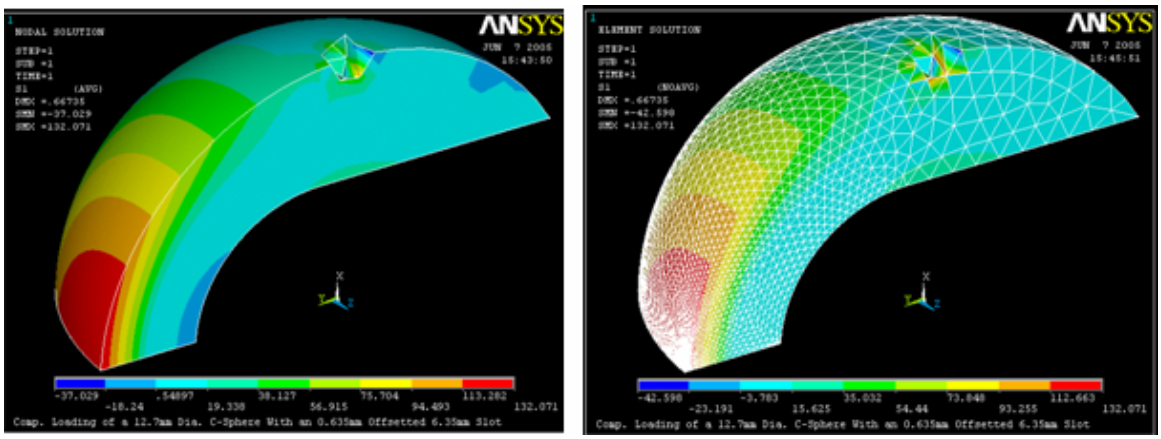

Figure 5. Nodal first principal stress distribution (left) and element first principal stress distribution (right) for the C-sphere specimen using the fine mesh model with the elements within the high stress concentration zone (under the load) carved out. This is the model used to evaluate the effective sizes whose results are shown in Figs. 6-7.

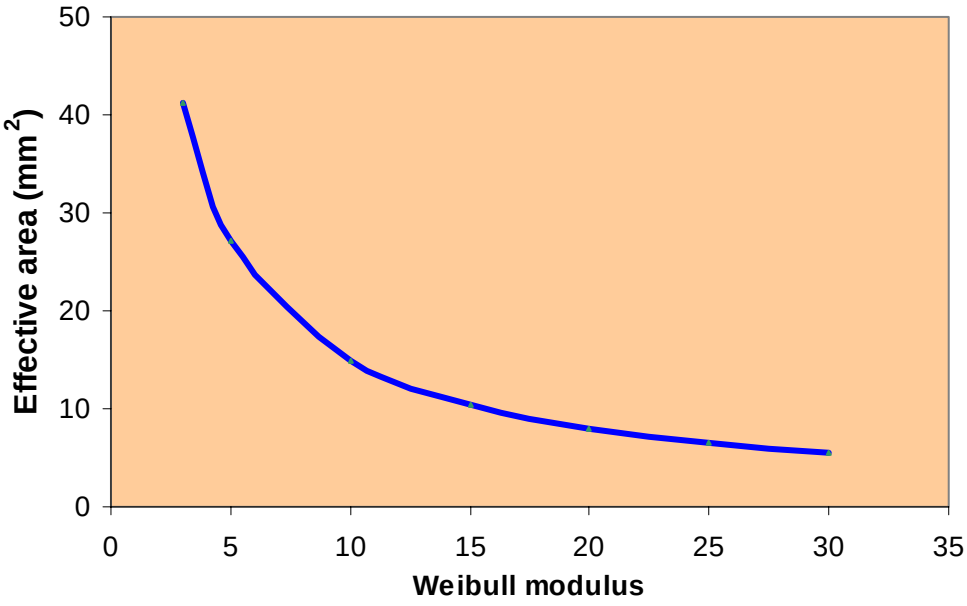

Figure 6. Effective area vs. Weibull module for the C-sphere specimen.

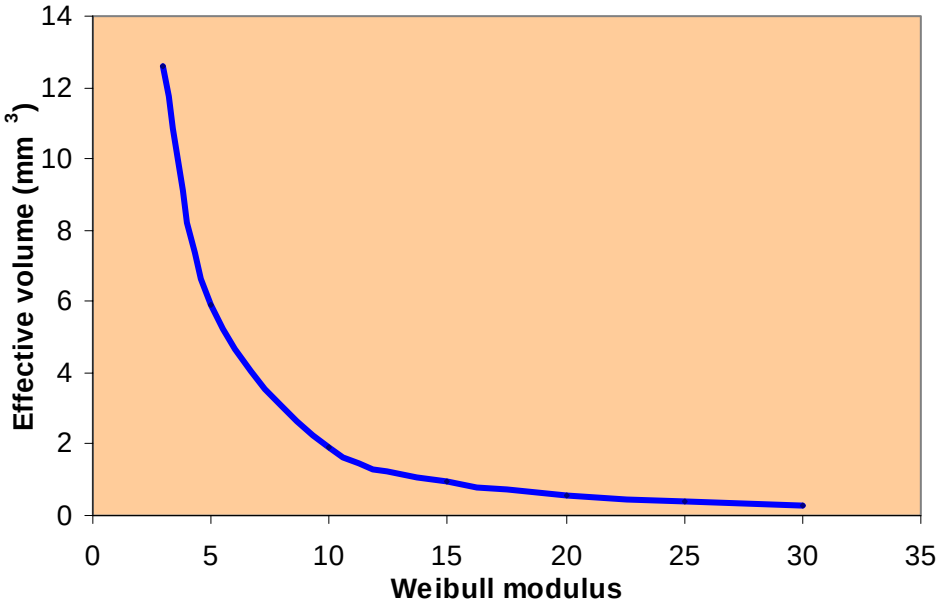

Figure 7. Effective volume vs. Weibull module for the C-sphere specimen.

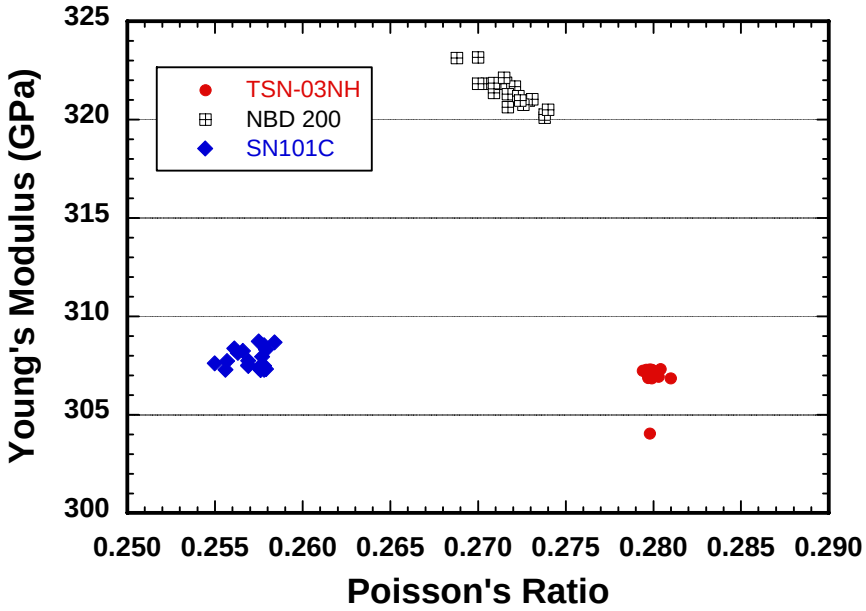

Figure 8. Elastic modulus and Poisson's Ratio distributions for three bearing grade Si_3N_4 materials as measured with RUS.

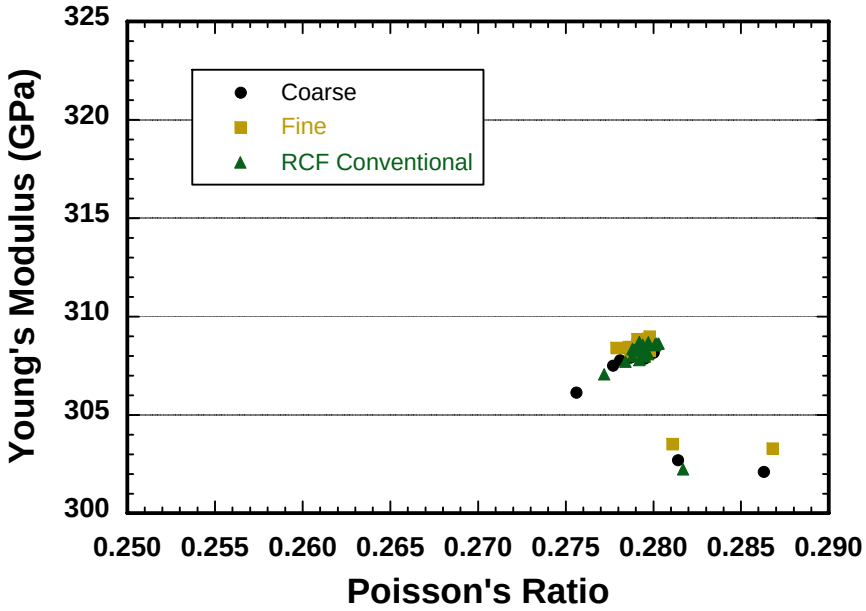

Figure 9. Elastic modulus and Poisson's Ratio distributions for Ceralloy 147-31N Si_3N_4 balls as measured with RUS. The three sets were machined per the conditions in Table I.

Implementing Agreement for a Programme of Research and Development on Advanced Materials for Transportation Applications

M. K. Ferber
Oak Ridge National Laboratory

Objective/Scope

The current mission of the IA-AMT is to investigate promising new technologies for evaluating and ultimately improving the performance of materials for transportation systems. The primary motivation for this activity is the fact that new material technologies are required to increase efficiency and reduce harmful emissions in these systems. Examples of these technologies include (1) light weighting to improve fuel efficiency, (2) surface engineering to improve the resistance to wear and contact damage, (3) development of durable coating systems for thermal, wear, and environmental management, and (4) development of revolutionary materials (structural ceramics and ceramic matrix composites) for operation at much higher temperatures and pressures. As discussed below, the research activities within the IA-AMT focus specifically on (1) the identification of promising new technologies for improving materials performance and (2) the development of specialized characterization techniques for validating the applicability of this technology to improve material properties while maintaining acceptable life-cycle costs.

Technical Highlights

This reporting period work continued on the evaluation of the laser spallation test for the measurement of coating adherence [1, 2]. In this test, the tensile forces required for coating debonding are generated by a pulsed laser focused on the back of the substrate. This initial impingement generates a compressive wave, which on reflection becomes tensile. Specific tests utilized commercial hardware for Laser Shock Peening (LSP), which is a relatively new surface treatment for generating compressive stress fields in the near surface regions of metallic materials. When applied to selected regions of engineering component such as gas turbine airfoils, these stress fields can greatly improve resistance to fatigue and increase tolerance to foreign object damage. The depth of the compressive residual stresses is typically much greater than those induced by conventional shot peening. As illustrated in Figure 1, the technique involves the production of mechanical shock waves by using a laser to generate a plasma over a small spot on the surface. This plasma is formed by the vaporization and subsequent ionization of a sacrificial material such as black tape or paint, which is first applied to the region to be treated. An over-layer of water, which is transparent to laser radiation, is used to confine the expansion plasma such that a shock wave is driven into the component. The surface and near surface regions are subject to plastic deformation if the pressure of the shock wave is greater than the yield strength of the material under shock conditions. In plane compressive stresses arise as the undeformed material attempts to restore the original shape of the surface.

The compressive pulse that is generated on the front face will be reflected as tensile pulse from the rear surface. If the tensile stresses are of sufficient magnitude they can lead to spallation of material located at the rear surface [3]. If a thin coating is present along the rear surface, these same tensile stresses can cause coating spallation [4].

The present study evaluated the adherence of a thermal barrier coating (TBC) system consisting of (a) bond coats of either vacuum plasma-sprayed (VPS) Ni-22Cr-10Al-1Y or VPS Ni-23Co-18Cr-12Al-0.3Y, (b) air plasma sprayed (APS) yttria stabilized zirconia (YSZ), and (c) substrates of either single-crystal (SX) Rene N5 or Mar M. In all cases the substrates were in form of 25 mm diameter disks approximately 6 mm in thickness. Typical bond coat and top coat thicknesses were 100 and 250 µm, respectively.

As reported previously, the as-sprayed coatings were found to spall when the incident power density exceeded 1 GW/cm^2. The coatings were subsequently aged at 1150°C for 10 and 100 hours in order to grow an alumina scale on the metallic bond coat. Based on previous studies, the presence of this scale is expected to weaken the interface. These samples are currently being tested using LSP; results will be reported in the net quarterly.

Status of Milestones

(1) Develop draft plan (Annex IV proposal) for implementation of lightweight materials activity. **(Completed: 09/04)**.

(2) Complete Annex II-Subtask 13 effort and issue report. **(Draft prepared-12/04).**

Communications/Visits/Travel

Author visit Brad Beardsley at Caterpillar Technical Center to discuss possible collaborations in the area of coating characterization.

Publications

[1] "Implementing Agreement For A Programme Of Research And Development On Advanced Materials For Transportation Applications (IA-AMT), Strategic Plan," March 2004, available on web site IA-AMT.ornl.gov.

References

[1] P. A. Steinmann and H. E. Hintermann, "A review of the mechanical tests for thin-film adhesion." Journal of Vacuum Science Technology A, Vol. 7, No. 3, 1989, pp. 2267-2272.

[2] J. Valli, U. Makela, and A. Matthews, "Assessment of Coating Adhesion." Surface Engineering, Vol. 2, No. 1, 1986, pp. 49-53.

[3] M. Boustie, F. Cottet, Y. Chauveau, and S. A. Marta, "Spalling of Aluminum and Copper Targets by Laser Shocks," pp. 741-50 in Shock-Wave and High-Strain-Rate Phenomena in Materials, edited by M. A. Meyers, L. E. Murr, and K. P. Stadhammer, Marcel Dekker, Inc., New York, 1992.

[4] M. Boustie, E. Auroux, and J. P. Romain, "Application of the Laser Spallation Technique to the Measurement of the Adhesion Strength of Tungsten Carbide Coatings on Superalloy Substrates," Eur. Phys. J. AP, 12, 47-53 (2000).

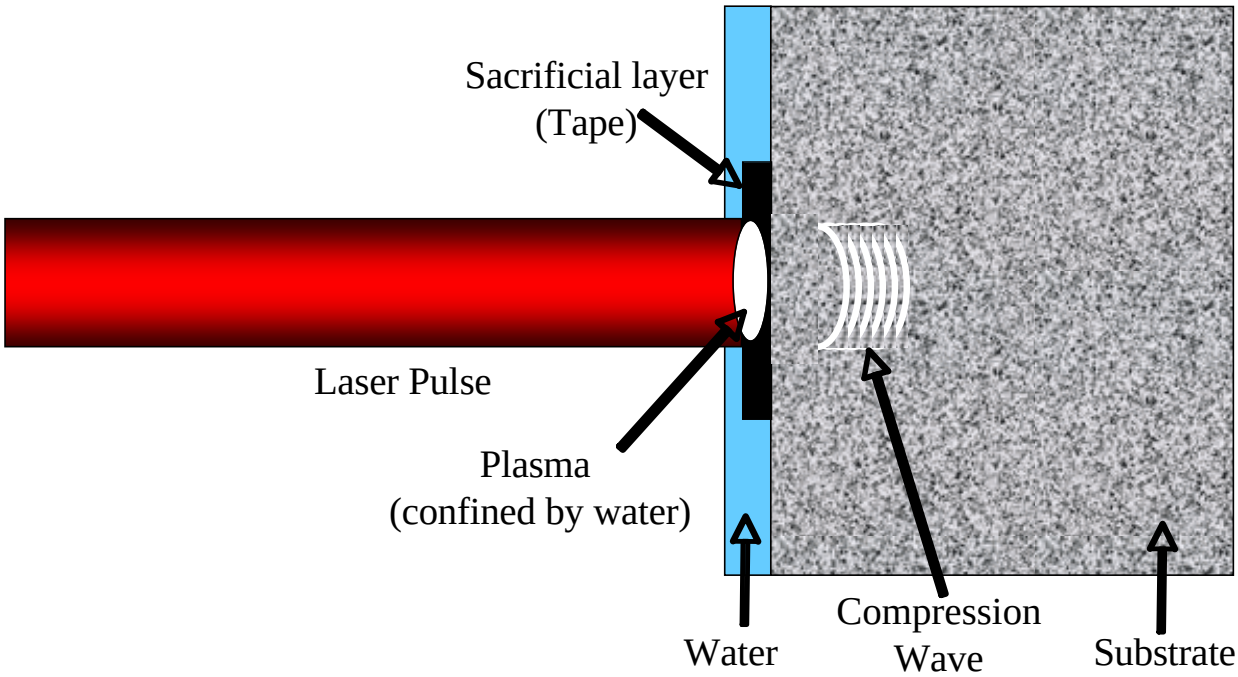

Figure 1: Schematic representation of the LSP process.

Mechanical Property Test Development

George Quinn
National Institute of Standards and Technology

Objective/Scope

This task is to develop mechanical test method standards in support of the Propulsion Systems Materials Program. Test method development should meet the needs of the DOE engine community but should also consider the general USA structural ceramics community as well as foreign laboratories and companies. Draft recommendations for practices or procedures shall be developed based upon the needs identified above and circulated within the DOE engine community for review and modification. Round robins will be conducted as necessary. Procedures will be standardized by ASTM and/or ISO.

Technical Highlights

1. General

Work continues on a Guide to Practice for Fractography that is now about 75% complete. Work on split cylinder flexure testing resumed and test data was collected on new zirconia specimens received from Cummins.

2. Fracture Toughness

No activity this period.

3. Fractography

Work continued on a NIST user-friendly "Guide to Best Practice" for fractographic analysis. This document will be about 300 pages long with hundreds of figures illustrating key fractographic markings in ceramics and brittle materials. It will complement the ASTM standard C 1322, Standard Practice for Fractography and Characterization of Fracture Origins in Advanced Ceramics.

Small revisions to five flaw definitions in the ASTM C 1322 Standard Practice for Fractography were balloted. Two negatives were obtained. These negatives were discussed at the Reno meeting of ASTM Committee C-28 Advanced Ceramics on May 16th, and were found to be nonpersuasive. The final revised 2005b version of C1322 was reviewed and has been sent to press. This concludes all our planned revisions to this standard for the time being.

4. Flexural Strength Testing of Cylindrical Ceramic Specimens

A limited amount of work resumed on this subtask this quarter in conjunction with the split cylinder testing described in the next paragraph. As part of our fixture design work, we tested one oversized steel dowel rod in our flexure fixture that has special cradles to hold round specimens as shown in Figure 1. We did this in order to ascertain whether minor yielding in the steel cradles (which had been detected after doing some ceramic tests) was due to fixture overload or an artifact of a transient load pulse when the ceramic specimens fractured. The yielding was only on a tiny portion of an edge of the cradles, but we decided to investigate the source of the deformation to possibly refine our new fixture design. The fixture and hardened steel dowel were loaded to static loads well above those used in the ceramic strength tests and then unloaded for inspection. No deformation whatsoever was detected in the steel fixture parts or the hardened steel dowel rod. This tends to confirm the notion that a shock–pulse in the fixture when the ceramic test pieces broke was the cause of the observed small deformations.

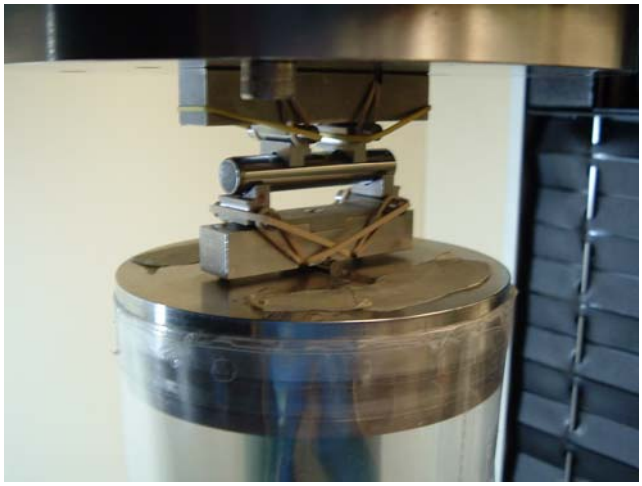

Figure 1 Steel dowel rod dummy specimen in the same four-point bend fixtures that were used to test split cylinder specimens as described in section 5 below. Special cradles hold the round specimens in the fixtures that are normally used to test rectangular bend specimens. Slight deformations on the cradle edges were observed after the ceramic strengths tests described below.

5. Split Cylinder Flexural Strength Testing

New zirconia rod specimens have been received from Cummins. Some of these were split into two halves and each half was tested as shown in Figure 2. The four-point testing was with effective spans of 20 mm x 40 mm. The three point was with a 40 mm span. The strength outcomes are

shown in Table 1 and Figure 3. Three-point strength numbers for the same batch of material that were obtained by Cummins on full cylindrical rods are shown in table 1 for comparison. The good news is that the 3-point strengths of the split rods are nearly identical to those of the full rods. The 4-point strengths are less which is not surprising in light of the usual Weibull size effects.

A remarkable finding was that although the split cylinders had the usual strength variability associated with ceramics, the strengths of the two halves of a particular rod were remarkably consistent. That suggests that the strength limiting flaws are very consistent within any given rod. A comprehensive fractographic analysis and maximum likelihood estimation (MLE) analysis for the Weibull parameters will be done for these specimens.

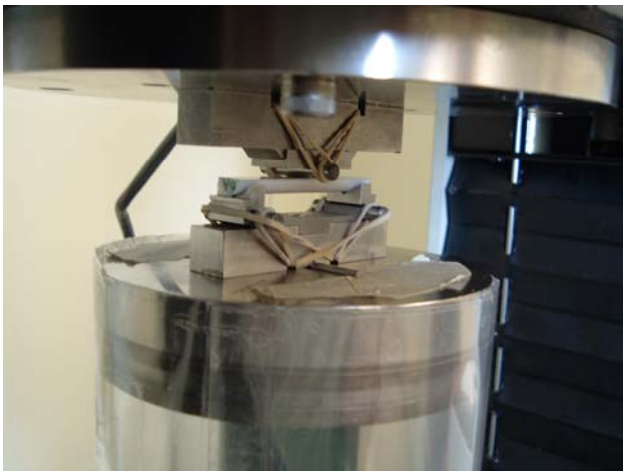

Figure 2 New split cylinder strength tests were conducted on zirconia rods that had been sliced in two lengthwise.

Table 1 Flexural strength data for zirconia cylindrical rods and split rods

Test	N (number of specimens)	Avg. Strength (MPa)	Std. Dev. (MPa)	Weibull modulus*	Weibull Char. Str.* (MPa)
Manufacturer data 3-point, full-sized cylinders	10	731	-	-	-
NIST 3-point, split cylinders	20	737	45	19.6	759
NIST 4-point, split cylinders	20	646	45	17.5	663

* Preliminary estimates. Linear regression

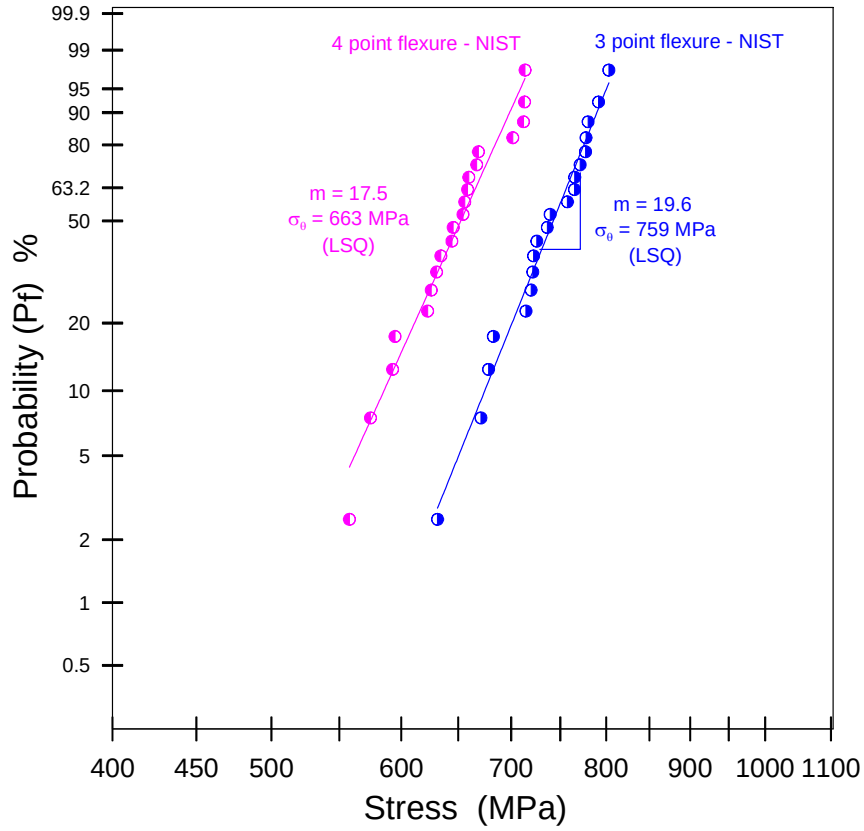

Figure 3 Flexural strengths of split zirconia rods tested measured at NIST. Preliminary Weibull parameter estimates are noted. The two distributions are very similar and appear to be shifted in accordance with the customary Weibull size effect.

The Weibull effective volume and effective areas for split cylinders are very difficult to estimate. There are no closed form solutions in the literature for these configurations. Nevertheless, as shown in analytical work by the author in two papers on the Weibull volumes and surfaces for rods and rectangular specimens,[1,2] no matter what the cross section geometry, round square or other, the ratio of the 3-point to 4-point strengths is the same. This is an astonishing result. Furthermore, it does not matter whether the flaws are surface- or volume-distributed and whether Weibull surface or volume scaling is used. This is a peculiar effect of the stress gradients being the same in the two configurations which is the case if they have the identical cross section shape and size. Hence:

$$\frac{\sigma_{3pt}}{\sigma_{4pt}} = \left(\frac{V_{E,4pt}}{V_{E,3pt}}\right)^{\frac{1}{m}} = \left(\frac{m+2}{2}\right)^{\frac{1}{m}} \left(\frac{L_4}{L_3}\right)^{\frac{1}{m}}$$

and since the span lengths in 3- and 4-point were the same ($L_4 = L_3$),

$$\frac{\sigma_{3pt}}{\sigma_{4pt}} = \left(\frac{m+2}{2}\right)^{\frac{1}{m}}$$

Thus, using an average Weibull modulus of 18.6 (data from table 1) the strength ratio should be 1.134, which is in superb agreement with the 1.140 shown in table 1 for either the characteristic strengths or the average strengths. This is a very gratifying outcome.

6. Hardness

No activity.

7. Diametral Compression

No progress this quarter.

8. Other

ASTM Committee C-28, Advanced Ceramics support

Information was sent to Dr. Stephen Gonczy about possible updates to the long standing ASTM standard C 1198 for elastic modulus determination of ceramics by forced resonance. Ballot items will be prepared for the next cycle to update this standard.

Status of Milestones

412149	Prepare ballot-ready first ASTM draft of cylindrical rod flexure strength test	Overdue
412151	Prepare review paper on flexural testing of cylindrical rods.	Overdue

Communications/Visits/Travel

G. Quinn provided some fractographic assistance to C. Lewinsohn at Ceramatec on the interpretation of breakage patterns in four-point flexure specimens.

G. Quinn reviewed some analytical work by Stephen Duffy on C- ring and O-ring strength test methods.

G. Quinn contacted Theo Fett, Jakob Kübler and R. Morrell in Europe about possible problems with the single edged V-notched beam method for obtaining fracture toughness data.

G. Quinn assisted B. Mikijelj at Ceradyne with questions pertaining to the indentation size effect in ceramic hardens testing and also on the use of the NIST hardness standards reference materials for Knoop and Vickers hardness.

G. Quinn met Prof. Keizo Uematsu of Nagoaka University at NIST for discussions on flaw characterization in ceramics, the silicon nitride ball bearing standard specification in ISO, and also a proposed fracture toughness by indentation standard in ISO technical committee TC 206, Fine Ceramics. Adoption of a Vickers indentation crack length method as an ISO standard for fracture toughness would be a mistake. The method is unreliable.

Publications and Presentations

1. G. D. Quinn, L. K, Ives, and S. Jahanmir, "On the Nature of Machining Cracks in Ground Ceramics: Part I: SRBSN Strengths and Fractographic Analysis," Machining Science and Technology, 9 (2005) 169 - 210.

2. G. D. Quinn, L. K, Ives, and S. Jahanmir, "On the Nature of Machining Cracks in Ground Ceramics: Part II: Comparison to Other Silicon Nitrides and Damage Maps," Machining Science and Technology, 9 (2005) 211 - 237.

3 G. D. Quinn, L. K. Ives, and S. Jahanmir, "Machining Cracks in Finished Ceramics," pp. 1-14 in *Fractography of Advanced Ceramics, II*, ed. J. Dusza, R. Danzer, and R. Morrell, TransTech Publ., Zurich, 2005.

References

1 G. D. Quinn, "Weibull Effective Volumes and Surfaces for Cylindrical Rods Loaded in Flexure," J. Am. Ceram. Soc., 86 [3] (2003) pp. 475-478.

2 G. D. Quinn, "Weibull Strength Scaling for Standardized Rectangular Flexure Specimens," J. Am. Ceram. Soc., 86 [3] (2003) pp. 508-510.

Surface Modification of Engineering Materials for Heavy Vehicle Applications

Stephen Hsu, Xaiolei Wang, Lewis K. Ives, Huan Zhang, Yanan Liang and Charles Ying
National Institute of Standards and Technology

Objectives

- Organize an international cooperative research program on an integrated surface modification technology under the auspice of the International Energy Agency (IEA)
- Design and identify surface features and patterns that can achieve friction reduction and enhanced durability for heavy duty diesel engine components.
- Develop understanding and appropriate models to explain the texturing effects on frictional characteristics. Develop appropriate thin films and coatings to achieve synergistic and complementary relationship with texturing to enhance performance.
- Discover and develop surface chemistry for protecting the films and coatings which work in synergy with the coatings.

Approach

- Determine the effect of size, shape, pitch, and patterns of surface textural features on friction under 1) high speed, low load regime; 2) high load, high speed regime; 3) high load, low speed regime.
- Develop cost effective fabrication technologies for creating surface textural features on various surfaces including metals, ceramics, and coatings.
- Develop test methodology to measure the effects of the textures on friction
- Conduct research to develop an integrated system approach to combine the best practices in thin films, coating, and surface chemistry for performances unrealizable by individual approach alone.
- Concurrently, organize an international cooperative research program under the auspice of the International Energy Agency (IEA) to pool resources and share this energy conservation technology worldwide.

Accomplishments this quarter

International Energy Agency activities

- Completed the organization of a Special Symposium on Surface Texture Design in conjunction with COST 532 (European Cooperative Research consortium on Triboscience and Tribotechnology) conference, Oct. 12-15, 2005 in Porto, Portugal.
- Attended the IEA End Use Working Party (EUWP) meeting on April 18-19, 2005 and presented the End of Term report on behalf of the IEA Implementing Agreement on Advanced Materials for Transportation. The EUWP voted to recommend four years' extension of the IEA work to Committee on Energy Research and Technology (CERT).
- Organized and recruited international participants from China, Australia, Finland, Japan, UK, Belgium to participate in the integrated surface technology activity.

Technical research

- Completed the initial development effort on enhanced selective electrochemical etching technique in combination with photolithography on steel surfaces.

- Successfully demonstrated that cavitation played a role under high speed high load conditions in a single dimple observation apparatus.
- Initiated an elasto-plastic lubrication model development effort to describe the friction reduction mechanism of surface textures under boundary lubrication conditions.

Introduction

Frictional losses are inherent in most practical mechanical systems. The ability to control friction offers many opportunities to achieve energy conservation. Over the years, materials, lubricants, and surface modifications have been used to reduce friction in automotive and diesel engine applications to promote energy efficiency. However, in recent years, progress in friction reduction technology has slowed because much obvious inefficiency has been eliminated. A new avenue is needed.

Recently, laser ablated dimples on surfaces have shown friction reduction properties and have been demonstrated successfully in conformal contacts such as seals where the speed is high and the load is low. The friction reduction mechanism in this regime appears to depend on the size, patterns, and density of dimples in the contact. The success of dimples in reducing friction has opened a new avenue for friction control for engine applications.

The objective of this project, therefore, is to explore the feasibility of surface texture designs to control friction in energy transmission devices. For long durability, the textures have to be protected by thin films/coatings and appropriate lubricating chemistry over a broad range of operating conditions. The final outcome of the project is to develop design guidelines for various engine component technologies to be implemented worldwide through international cooperation through IEA.

To achieve worldwide energy conservation, a concomitant international cooperative research under the auspice of the International Energy Agency is being conducted to pool resources from various countries to accelerate this technology development. Towards this end, UK, China, Australia, Finland, Sweden, Israel, and Japan have agreed to participate under the IEA annex IV on surface technology.

Approach

Previously, experiments were conducted to examine various surface textures on steel surfaces using photolithography and chemical etching. Using the same area coverage (% of area occupied by the surface textural features), surface features such as grooves, triangles, ellipses; circles were compared under high speed low load conditions similar to the seals operating conditions. Results suggested that: 1) surface texture size and shape had significant influence on friction; 2) orientation of the surface features with respect to the sliding direction changed the friction; 3) the primary effect of surface textures is to accelerate the transition into hydrodynamic lubrication regime. What is the fundamental friction reduction mechanism in this regime is still not clearly understood.

From energy efficiency point of view, friction reduction under high load low speed conditions has much higher impact factor. When we ran the same surface texture patterns under boundary lubrication conditions, instead of friction reduction, we get friction increase due to increased surface roughness effect. A collaborative effort with Northwestern University using a sophisticated elastohydrodynamic friction model confirmed our experimental observations.

Basically, under boundary lubricated conditions (high load low speed), the edge stresses around the dimple increase friction rather than decrease friction.

We then proceeded to develop a new surface textural feature with an inclined plane at the bottom of the feature to artificially generate a hydrodynamic wedge effect under plastic deformation loading; we call this elasto-plastic lubrication model. Last quarter, we achieved significant friction reductions using steel on steel contacts under boundary lubricated conditions. This quarter, we focus on developing a low cost chemical etching technique to produce small dimples without inclined planes to see whether we can achieve friction reduction.

Technical highlight

When we used hard metals such as 52100 steel, the initial high contact pressure caused severe wear damaging the surface textures and the friction reduction results were erratic. To overcome this issue, we developed a wear-in procedure to create a smooth crater surface of approximately 0.5 mm diameter and the texture was then carved onto the surface inside the crater with a diamond tip on the triboindenter. This way, a controlled interface was created to avoid severe wear-in. We demonstrated that friction in a 52100 steel/52100 steel contact could be reduced significantly from 0.09 to 0.06.

Last quarter, we focus on developing a low cost and rapid fabrication method and conduct tests to verify the friction reduction characteristics of the new fabrication technique. We have used microlithography/chemical etching process previously to fabricate dimples with depth ranging from 3 to 10 μm. For shallow dimples, we need to control the etching process precisely. Numerous factors can affect the electrochemical etching, including electrolyte properties, voltage, and composition of the material. Since electricity always passes the way with high conductivity, the inhomogeneous oxidant on the work piece will make etching selective. This is critical when shallow depth is needed. A special electrolyte composed with acids was used for this purpose. Acid is effective to remove the oxidant on the surface so that etching can start uniformly. A circular dimple pattern was produced by this technique. A four-ball wear tester was used to carry out the friction tests using a ball-on-three flat configuration. The results show that up to 32% friction reduction has been achieved by the texture generated by this fabrication technique. Compared with previous texture generated by nanoscratching with sloped bottoms, the friction reduction was not as high (40-80%).

This quarter, we continue to refine the fabrication technique trying to introduce a sloped bottom texture features using micro-electrochemical methods. We achieve partial success by exploring a stress-enhanced electro-chemical etching concept. The basic concept is to apply a voltage through a sharp needle which can be translated laterally using a translation stage. We were successful in generating a sloped bottomed surface texture feature this way. The next step is how to generate a pattern in a concave surface as required by our testing protocol.

In situ observation of cavitation

Cavitation has been proposed as one mechanism by which surface texture features can reduce friction under hydrodynamic lubrication conditions. According to Reynolds equations, a surface feature such as a dimple will result in a localized asymmetric pressure fluctuation, Fig. 1a but no net change in lubricant pressure. The occurrence of cavitation, however, will impose a limit on the low-pressure inlet side of the fluctuation, giving rise to a net increase in hydrodynamic pressure in the fluid film, Fig. 1b. In order to verify the presence of cavitation and study the

effect of test conditions and different feature geometries on cavitation, a pin-on-disk tester was modified to allow the observation of cavitation through a transparent sapphire pin specimen sliding against a polished steel disk. A schematic drawing of the apparatus is shown in Fig. 2. The sapphire pin specimen was prepared by grinding parallel flats, approximately 3.5 mm in diameter, on a 4.76 mm diameter sapphire ball. A single dimple was fabricated at the center of one of the flats. That flat was then slid against a polished steel disk. A CCD camera attached to a tube microscope was used to obtain images of the dimple and contacting disk surface during sliding. Figure 3 shows an example of cavitation in a dimple. The dimple is partly filled with gas generated by cavitation. A trail of cavitation gas in the thin film of lubricant separating the pin and disk surfaces can also be seen behind the dimple. Fine scratches in the lapped 52100 steel disk are visible in the image. Note that the area of contact between the flat on the sapphire pin and disk extends well beyond the area of the image shown in Fig. 3. In this example the dimple was approximately 210 mμ in diameter and 1.5 mμ in depth. The applied load was 2 N, the lubricant used was Mobil Velocite No. 10 oil (ISO VG 22).

A second example of cavitation is shown in Fig. 4. In this case the dimple was 90 μm in diameter and had a depth of 9 μm, indicating that cavitation still occurred despite the different dimple diameter and depth. In the examples shown the sliding speed was quite low, 0.3 mm/s in Fig. 3 and 0.2 mm/s in Fig. 4. However, similar appearing cavitation has been observed at sliding speeds as high as 75 mm/s. The cavitation itself appears to result from the release of dissolved air in the oil due to the drop in pressure at the entrant edge of the dimples.

We have now begun to understand the friction reduction mechanism of textures under high speed low load conditions.

We have also initiated a modeling effort of textures under boundary lubricating conditions based on our theory of elasto-plastic lubrication mechanism. In boundary lubrication conditions, continuous fluid film may not be present and each texture feature may be treated as a liquid pool under compression. We are modeling the fluid pressure generated by deformation and calculating the sealing pressure surrounding the texture feature. We will report our progress next quarter.

Publications/Presentations

Presentations:

Jorn Larson Basse, X. Wang, L. Ives, S. M. Hsu, “Some friction experiments with dimpled surface texture,” The fourth China International Symposium on Tribology, Xian, China, November 8-11, 2004.

S. M. Hsu, “An Integrated surface modification technique to control friction: a new paradigm,” Keynote speaker, the 4th China International Symposium on Tribology, November 8-11, 2004,Xian,China.

Y. Chae, X. Wang, S. M. Hsu, “The size effect of surface texture on lubricated friction,” The First International Conference on Advanced Tribology, Singapore, Dec. 1-3, 2004.

Publications:

Jorn Larson Basse, X. Wang, L. Ives, S. M. Hsu, "Some friction experiments with textured surfaces," Proceedings of Nordic Symposium on Tribology, Troms, Norway, June 2004.

X. Wang, S. M. Hsu, "An Integrated surface modification technique to control friction: a new paradigm," Keynote paper, the 4th China International Symposium on Tribology, November 8-11, 2004,Xian,China.

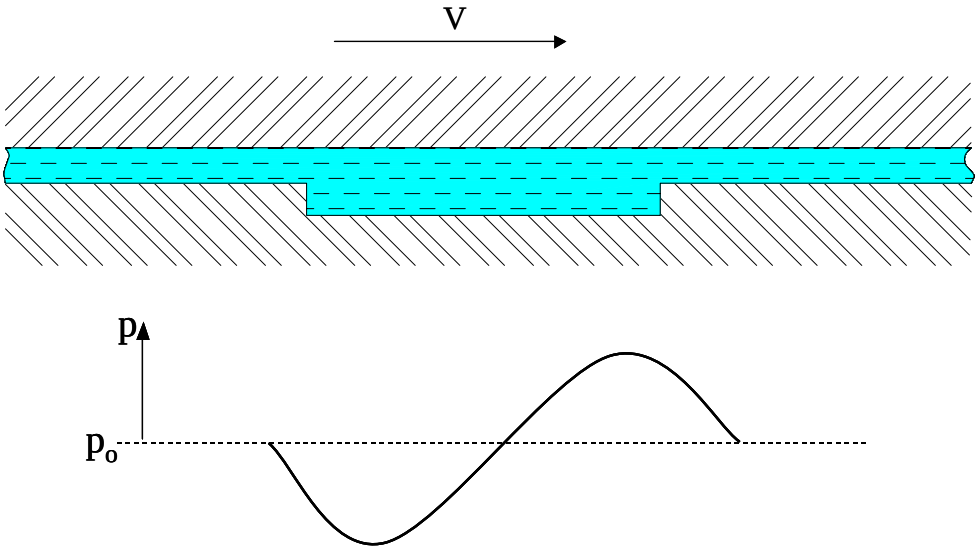

(a)

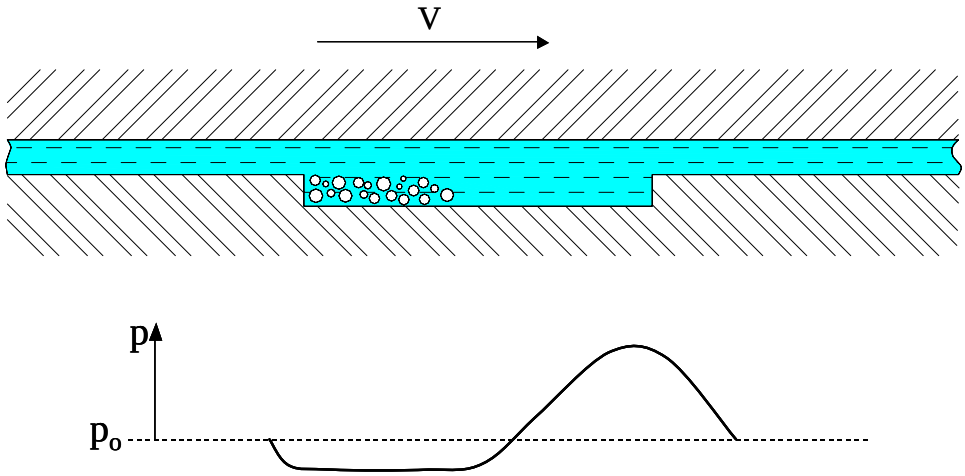

(b)

Fig. 1a. Schematic drawing showing an upper sliding surface and lower surface with dimple separated by a film of lubricant. The variation in pressure in the lubricant film caused by the dimple is shown below. The effect of cavitation in the dimple on the pressure variation is illustrated in Fig. 1b.

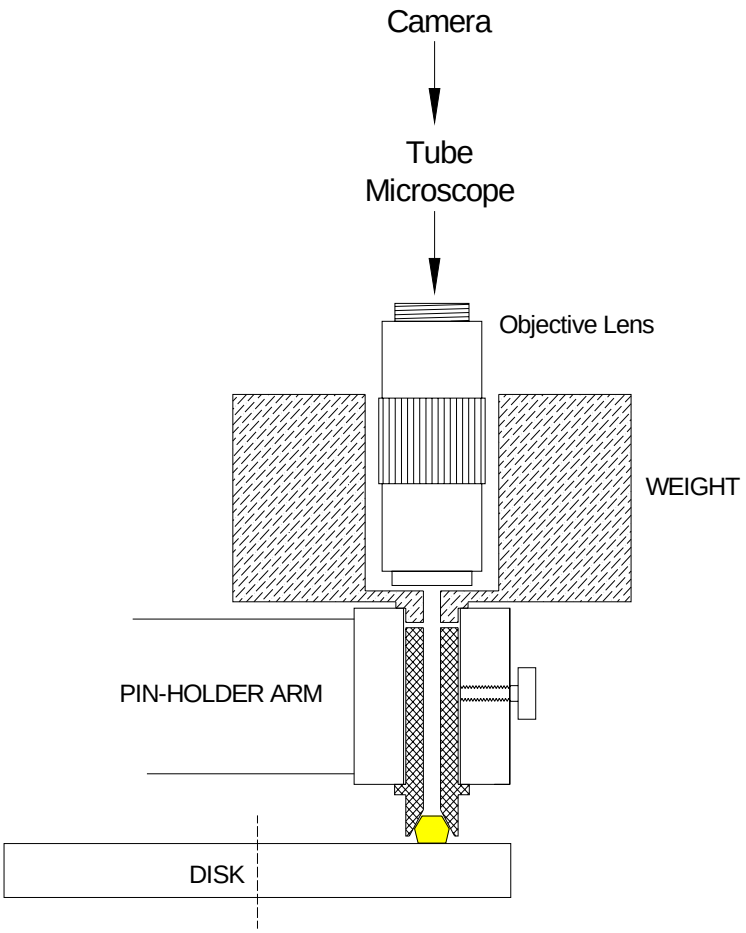

Fig. 2. Schematic of the test setup used to observe cavitation with a pin-on-disk apparatus.

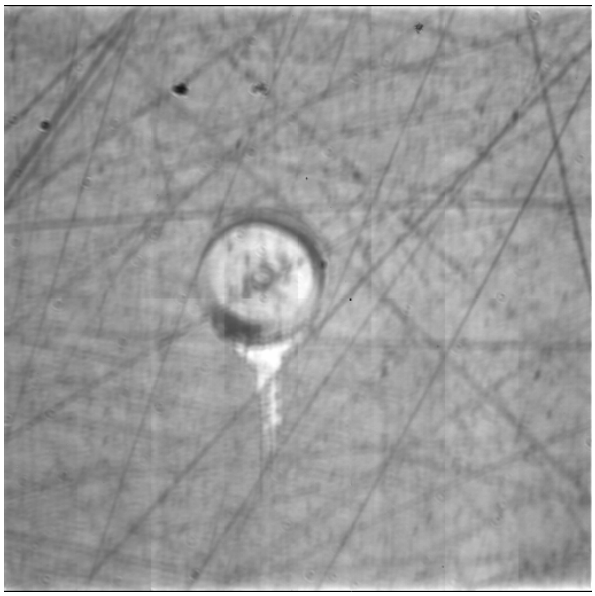

Fig. 3. Trail of cavitation gas behind a dimple in the flat surface of sapphire pin sliding against a 52100 steel disk. The dimple diameter is approximately 210 mm.

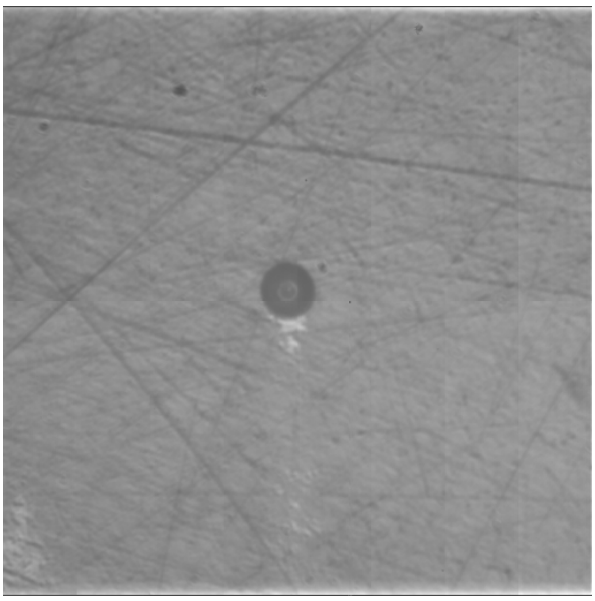

Fig. 4. Trail of cavitation gas behind a 90 mm diameter dimple in the flat surface of sapphire pin sliding against a 52100 steel disk.